Title

Geometry based local transport phenomena in classical and quantum regimes

Author

Dugar, Palak

Publication Date

2021

UNIVERSITY OF CALIFORNIA, MERCED

Geometry based local transport phenomena in classical and quantum regimes

A dissertation submitted in partial fulfillment of the requirements
for the degree of Doctor of Philosophy
in

Physics

by

Palak Dugar

Committee in charge:

Linda Hirst, Chair
David Strubbe
Chih-Chun Chien

2021

The dissertation of Palak Dugar, titled Geometry based local transport phenomena in classical and quantum regimes, is approved, and it is acceptable in quality and form for publication.

Chih-Chun Chien Principal Adviser	Date
Linda Hirst Committee Chair	Date
David Strubbe Committee Member	Date

University of California, Merced
2021

Acknowledgments

I would first like to express my gratitude towards my advisor, Prof. Chih-Chun Chien for his invaluable guidance, support and patience during these five years. Thank you for providing me with the tools that I needed to become a physicist and for being a great mentor.

Thanks to my committee members, Prof. Linda Hirst and Prof. David Strubbe for challenging my knowledge and pushing me to think about the greater implications of my research. I am also grateful to my co-author, Prof. Michael Scheibner for his time and guidance. Many thanks to the Physics group for providing summer and travel fellowships over the course of my graduate studies.

I also appreciate all the support I've received from my family. Finally, a special thanks to all my friends: Apoorva, Amrita, Neha, Uma, Lian, Alain, Farnaz, Ritwika and Alex for being there for me.

Curriculum Vitae

Education

2016 – 2021	• **PhD-Physics, University of California, Merced**
2012 – 2014	• **MSc-Physics, University of Delhi**
2009 – 2012	• **BSc-Physics Honours, University of Delhi**

Research Publications

Journal Articles

1 **Dugar**, **P.**, Scheibner, M., & Chien, C.-C. (2020). Geometry-based circulation of local photonic transport in a triangular metastructure. *Phys. Rev. A*, *102*(2), 023704.
🔗 https://doi.org/10.1103/PhysRevA.102.023704

2 **Dugar**, **P.**, & Chien, C.-C. (2019). Geometry-induced local thermal current from cold to hot in a classical harmonic system. *Phys. Rev. E*, *99*(2), 022131.
🔗 https://doi.org/10.1103/PhysRevE.99.022131

3 **Dugar**, **P.**, Kumar, M., TC, S. K., Aggarwal, N., & Gupta, G. (2015). Carrier relaxation dynamics in defect states of epitaxial GaN/AlN/Si using ultrafast transient absorption spectroscopy. *RSC Adv.*, *5*(102), 83969–83975.
🔗 https://doi.org/10.1039/c5ra10877b

4 Krishna, T. S., Aggarwal, N., Reddy, G. A., **Dugar**, **P.**, Mishra, M., Goswami, L., Dilawar, N., Kumar, M., Maurya, K., & Gupta, G. (2015). Probing the correlation between structure, carrier dynamics and defect states of epitaxial gan film on $(11\bar{2}0)$ sapphire grown by rf-molecular beam epitaxy. *RSC Adv.*, *5*(89), 73261–73267.
🔗 https://doi.org/10.1039/C5RA10099B

Abstract

In this thesis, we study geometry-based non-equilibrium steady-state transport phenomena theoretically with the overarching goal to understand how the multi-path geometry can affect transport in classical and quantum systems. We begin with an overview of the physics associated with classical and quantum transport and the formalisms used to obtain results. In the non-equilibrium steady-state, one would expect that the local gradient imposed by the reservoirs would define a unique direction of flow from high-to-low. However, through this thesis we show that may not always be the case as one can devise a local steady-state atypical flow which goes from (low-to-high) by using a system with multi-path geometry. We address the universality of these steady-state local atypical flows in systems with multiple paths, through the following undertakings:

- We show a classical harmonic system of Hookean springs and point masses coupled in a multi-path geometry driven by two Langevin reservoirs at different temperatures can give rise to a steady-state local atypical thermal flow. Through molecular dynamics simulations of Langevin equations for this system, we show that the atypical current depends on both internal and external parameters such as ratio of spring constants, ratio of masses and system-reservoir coupling respectively. We also show the robust nature of this atypical current against substrate induced non-linearity and asymmetric system-reservoir coupling.

- Two different approaches, namely the Redfield and Lindblad master equation, are used to extract the non-equilibrium steady-state thermal transport of a

quantum system of oscillators coupled in a triangular geometry described in the coordinate-momentum space and as a Bose-Hubbard Hamiltonian respectively. Through the third quantization formalism and numerical simulation of the quantum master equations we show that atypical flows are universal to multi-path geometry and arise in both descriptions. We show that these atypical flows give rise to two patterns of internal steady-state circulations, clockwise and counterclockwise. We map out phase diagrams for these flow patterns as a function of system parameters thereby showing its robust nature.

- Finally, we show that these atypical flows and internal steady-state circulations are not limited to thermal transport but can be achieved for particle transport as well. We phenomenologically describe a hybrid system comprising of photonic structures and electronic quantum dots and show that the triangular geometry of this system can give rise to steady-state photonic circulations. We show the robust nature of these circulations against photon blockade and interactions through numerically calculated phase maps with the ratio of tunneling coefficients and system-reservoir coupling as the parameters.

At the end, we elaborate on the applications of these geometry-based steady-state atypical flows and outline possible experimental realizations to observe these atypical flows and circulations.

Contents

List of Figures

Chapter 1

Introduction

1.1 Motivation

Recent experimental advances in the realization of low dimensional systems have revolutionized the modern industry [1–4]. These advances are a culmination of theoretical and experimental efforts spanning over half a century. Understanding and control of transport in low dimensional systems down to the atomic and molecular scale will continue to play a vital role in the development of future technology. Characterization of transport phenomena requires one to work at the interface of non-equilibrium physics, thermodynamics classical and quantum mechanics. A simple example of transport phenomena is when a system is subjected to an external environment such that it develops a chemical potential or temperature gradient, which results in particle current or energy current through it.

Imposing a gradient on a system places restrictions on the direction of the total current but no such restrictions are levied on the local currents within the system. For example, it is known from the second law of thermodynamics, that a total steady-state thermal current from a cold to hot body without any other changes to the system is not possible [5]. However, no statement of the second law imposes any such restrictions on a local current in the system [6]. Therefore, looking into the local transport in the system can lead to interesting physics [6, 7]. Ref. [7] exploits different geometries to show that "anything is possible" in regards to the direction of flux within a system of harmonic oscillators.

When an electron beam traverses a two arm interferometer which encloses a constant magnetic field, a magnetic field dependent shift in the interference pattern can be observed even though the electron paths are in a region of zero magnetic field this non-local effect is popularly known as the Aharonov-Bohm effect [8]. The ring geometry provides a convenient platform for realization of the persistent current induced by a magnetic flux from an external magnetic field [9–11]. For charged particles like electrons, it is always possible to use an external magnetic field to induce a circulating current in classical [12] as well as quantum systems [11]. However, for neutral carriers such as photons or phonons, there are no natural means for inducing circulations. For these neutral particles, it is possible to exploit their interaction with matter to generate an artificial gauge field [13–15], which drives them the way a magnetic field drives a charged particle.

Moreover, without a magnetic field the ring geometry by itself has been used to induce current vortices [16–19], chiral current [20], current magnifications [21]. The ring geometry also offers an elementary probe to study topological properties of 1D Bose fields [22]. Furthermore, it has been shown that a ring embedded with two quantum dots and connected to external electrodes shows circulating currents [23]. Ref. [24] shows quantum non-locality without inputs for a triangular network, a consequence of its triangular network configuration which is different from previously known forms of quantum non-locality. Ref. [6] shows that the quantum interference of tunneling electrons in a system of two quantum dots individually coupled to two reservoirs can also result in a circulating electric current. Ref. [25] shows that the steady-state quantum electronic current through a triangular geometry shows circulation even in the absence of magnetic field.

It is clear to see from these examples that geometry plays a crucial role in determining the system's transport properties. Motivated by these non-trivial results, in this thesis we explore the geometry of multi-path systems and show its influence on classical and quantum thermal and quantum particle transport. With this thesis, we aim to show that multi-path systems can give rise to an atypical steady-state current in classical harmonic systems and tunable internal steady-state thermal and photonic

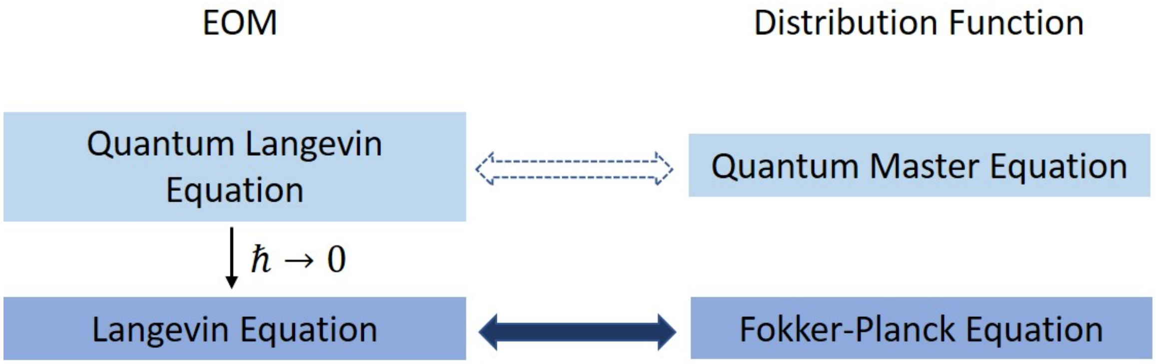

Figure 1.1: Relation between EOM and distribution function approaches.

current circulations in bosonic systems without using any additional media as required for artificial gauge fields or interactions. We show that these circulations are a consequence of the multi-path system geometry and are a universal phenomenon in the sense that they can be observed in all quantum systems with multi-path geometries.

1.2 Approaches to non-equilibrium transport

Open systems provide a natural framework to study non-equilibrium transport. The basic idea of an open system is that a system of interest interacts with an external environment and evolves under its influence. Standard approaches to study non-equilibrium transport can be broadly categorized into the following: Non-equilibrium Green's function [26, 27], path integral [28, 29], equation of motion (EOM) and probability distribution approaches. All of which can be adapted to work in both the classical and quantum regimes. There are a couple of equation of motion approaches such as Langevin equations [30–33] and quantum stochastic Schrödinger equation [34]. Classically, open systems can be equivalently described by stochastic Langevin equation and through deterministic evolution equation for the system's phase space distribution function more commonly known as the Fokker-Planck equation. In the limit $\hbar \to 0$, the quantum fluctuation-dissipation relation becomes the $\delta-$correlated classical fluctuation-dissipation relationship [35, 36]. Unlike its classical counterpart, the relationship between the quantum Langevin equation and the quantum equivalent of

Fokker Planck equation, more commonly referred to as quantum master equation, is generally not obvious [37] and sometimes not present [38, 39]. These relations are summarised in Fig. 1.1. The reason behind the absence of this equivalence are the approximations one employs in deriving the quantum master equations. We will elaborate upon these approximations in chapter 2.

1.3 Outline

In chapter 2, we introduce the classical Langevin equation and the quantum master equations. We briefly discuss the numerical schemes used to simulate the Langevin and quantum master equation. We introduce the idea behind the third quantization formalism and show the framework for bosonic systems.

In chapter 3, we present our work on a minimal classical multi-path system made up of Hookean springs and three masses. We show that the local steady-state thermal current can show an atypical behavior. We present our numerical results and show through phase diagrams that the regime of atypical thermal current depends explicitly on the system-reservoir coupling, ratio of spring constants and ratio of masses. We also show that adding a non-linearity to the system does not destroy the atypical behaviour but rather can be used to tune the atypical regime.

In chapter 4, we present our results for a system of coupled oscillators placed on a multi-path triangular geometry modeled through the co-ordinate-momentum operators and Bose-Hubbard Hamiltonian. We calculate the non-equilibrium steady-state local and total currents through the Redfield quantum master equation (RQME) and Lindblad quantum master equation (LQME), and show the system exhibits an internal circulation of steady state thermal currents in both representations. We show how tuning internal and external system parameters affects the regimes of circulations. We also show that the circulations survive in the presence of onsite interactions.

In chapter 5, we show that the steady state photonic current in a phenomenological model of a triple quantum dot metastructure, calculated using the Lindblad form of the quantum master equation shows an internal circulation of current. Through phase maps, we outline the behavior of the circulations as a function of the maximum number of photons allowed per dot, system-reservoir coupling, ration of tunneling coefficients and on-site interaction.

In chapter 6, we discuss possible experimental realizations of the classical and quantum multi-path systems presented in the previous chapters. We also present applications of the classical atypical thermal current and the circulation of thermal and particle currents.

In chapter 7, we summarize all the results in this thesis.

Chapter 2

Formalism

2.1 Classical Langevin equation

It is known that Newton's equation of motion describes the dynamics of classical systems. The dynamics of a classical system which follows Newton's law while in contact with reservoirs can be described by the Langevin equation [32, 40].

Classical Langevin equations are stochastic equations where the effect of the environment can be modelled phenomenologically by adding two terms, the frictional force and a fluctuating random force also known as noise, $\eta_n(t)$, simultaneously to the system's Newton's equation. The noise is defined through its statistics and is generally taken to be Gaussian and mean $\langle \eta_n(t) \rangle = 0$. This phenomenological stochastic equation of motion can be written as:

$$m_n \ddot{x}_n = F_n - b_n \dot{x}_n + \eta_n(t). \tag{2.1}$$

Here m_n is the mass of the oscillator, F_n is the deterministic Newton's force on the n-th mass and b_n is the frictional coefficient coupling the system to a reservoir. Since the origin of the frictional and random forces is the same (effect of coupling to a reservoir) these forces should be correlated, which physically manifests as the fluctuation–dissipation theorem [41]. This relation essentially describes the linear response of a system and ensures that in the long time limit the system achieves equilibrium or is in a non-equilibrium steady-state.

Eq. (2.1) does not depend on the past of the reservoir and falls under the category of Markovian Langevin equations, which assumes that dissipation is instantaneous and independent of the system's past velocities. This instantaneous dissipation in the above equation means that the noise, $\eta_n(t)$ is $\delta-$correlated and has a vanishing mean $\langle \eta_n(t) \rangle = 0$; this type of noise is more commonly referred to as white noise. This white noise satisfies the fluctuation-dissipation relation of the first kind [41, 42]:

$$\langle \eta_n(\tau)\eta_n(\tau + t) \rangle = 2b_n k_B T_n \delta(t), \tag{2.2}$$

where k_B is the Boltzmann constant, T_n is the temperature of the reservoir and $\langle \rangle$ denotes the ensemble average taken over independent random realizations. The white noise used here, or any type of noise in general represent stochastic processes which are characterized through their probability distribution. To describe the probability distribution of a stochastic process, one can discuss either its expectation for a single system over time or its expectation over many identical systems at a time instance. The latter type of averaging is known as an ensemble average and it is what we use in this thesis to characterize the white noise.

We note that the Markovian Langevin equation is an idealization [41] as it implicitly assumes that the reservoir interacts instantaneously with the system. For a system to be in steady state, the position and velocity correlations by definition should be time independent. However, for Markovian Langevin equation even the equilibrium velocity correlations will have a time dependence [41]. Nonetheless, this time dependence is exponentially decaying and the use of Eq. (2.1) is reasonable and acceptable when the time scale associated with the reservoir is short compared to the time scale associated with system dynamics. But when a distinction between these time scales cannot be made, one needs to formulate an improved version of Eq. (2.1) commonly known as the generalized Langevin equation [43] through a non-Markovian framework which can model the system dynamics more accurately [43, 44]. We simulate the classcial langevin equation through non-equilibirum molecular dynamics (NEMD). In our simulations, we use the Euler scheme [42, 45] which is accurate up to first order in time step size and a second order scheme introduced in Ref. [46] which is accurate up to second order in time step size.

2.1.1 Euler-Maruyama method

The Euler-Maruyama method is an extension of the well known Euler method which is used to approximate solutions of deterministic differential equations. The Euler-Maruyama method provides a first order numerical approximation technique to solve stochastic differential equations. The classical Langevin equation, Eq. (2.1) under the Euler-Maruyama method [45] can be approximated as:

$$\begin{aligned} x_n(t+dt) &= x_n(t) + dt v_n(t) & (2.3) \\ v_n(t+dt) &= v_n(t) + \frac{dt}{m_n} F_n(t) - \frac{dt}{m_n} b_n v_n(t) + \frac{dW_n}{m_n}, & (2.4) \end{aligned}$$

here the W_n is the Wiener process [47] $(W_n(t+dt) - W_n(t) = dW_n)$ which is related to the stochastic force $\eta_n(t)$ as:

$$dW_n = \eta_n(t) dt. \tag{2.5}$$

The amplitude of the Wiener process has a characteristic $\sqrt{t}$ dependence which arises as a consequence of the following properties of Wiener process:

$$\begin{aligned} \langle W_n(s) W_n(s^{'}) \rangle &= 2 k_b T_n b_n min(s, s^{'}) & (2.6) \\ \langle (W_n(t+dt) - W_n(t))^2 \rangle &= 2 k_b T_n b_n dt. & (2.7) \end{aligned}$$

Hence dW_n can be written as:

$$W_n(t+dt) - W_n(t) = \sqrt{2 k_b T_n b_n dt} \mathcal{N}(0,1), \tag{2.8}$$

where $\mathcal{N}(0,1)$ is a normal random number with zero mean and unit variance and all symbols have their previously defined meaning.

2.1.2 Second order method

A second order approximation in both the deterministic and stochastic parts of the differential equation can be obtained from the method described in Ref. [46]. An approximation accurate upto $(dt)^2$ contains the integral of the difference between two Wiener processes and hence the random number becomes correlated. To simplify the situation, the correlated random number is decomposed into two uncorrelated random numbers with specific weights. Following the prescription in Ref. [46], the equations take the following form:

$$
\begin{aligned}
x_n(t+dt) &= x_n(t) + dt v_n(t) + C_n(t) && (2.9)\\
v_n(t+dt) &= v_n(t) + \frac{dt}{2m_n}(F_n(t) + F_n(t+dt)) \\
&\quad -\frac{dt}{m_n} b_n v_n(t) + \frac{dW_{na}}{m_n} - \frac{b_n C_n(t)}{m_n} && (2.10)\\
C_n(t) &= \frac{dt^2}{2m_n}(F_n(t) - b_n v_n(t)) + \frac{dt}{2m_n}(dW_{na} + \frac{dW_{nb}}{\sqrt{3}}), && (2.11)
\end{aligned}
$$

where dW_{na} and dW_{nb} are two independent Wiener processes of the form of Eq. (2.8).

For the classical harmonic system, the results from Euler-Maruyama and this second order method are almost equivalent. However, on addition of nonlinear substrate effects the Euler-Maruyama requires a long simulation run time therefore, we employ the full second-order method as it gives the steady state results for a smaller simulation run time.

2.2 Quantum master equation

For a closed quantum system described with pure states, the dynamics can be described by the Schrödinger equation [48]. Equivalently, the Liouville–von Neumann equation describes the time evolution of the density matrix of a closed quantum system with mixed states [48]. Both these closed system approaches describe a unitary evolution of the system.

To model the transport in a system of interest, we work in the open quantum system framework, by coupling the system to reservoirs which mimic an external environment. Since reservoirs are treated as systems with infinite degrees of freedom, it is not possible to describe the complete system dynamics as is done for closed systems. In such cases, the system dynamics are not only dictated by the system of interest's internal dynamics, but are also influenced by its interactions with reservoirs. As one is generally interested in the dynamics of the system of interest one can trace out the reservoir degrees of freedom, and get the reduced density matrix for the system of interest. The evolution of this reduced density matrix can be determined through effective equations of motion known as quantum master equations [49, 50]. Different sets of approximations are made to derive different types of quantum master equations. In the following section, we list the approximations involved in the derivation of the Redfield and Lindblad forms of the master equation.

2.2.1 Derivation

The following derivation has been adapted from references [49–53] to understand where and what are the approximations required. Here, S, the system of interest interacting with reservoirs, B constitutes an open quantum system and the complete Hamiltonian for it can be written as:

$$\mathscr{H} = \mathscr{H}_S + \mathscr{H}_B + \mathscr{H}_{int}, \tag{2.12}$$

where $\mathscr{H}_S$ is the system Hamiltonian, $\mathscr{H}_B$ is the Hamiltonian of the reservoirs and $\mathscr{H}_{int}$ represents the Hamiltonian for the interaction between the system and the reservoirs.

In the interaction picture [48, 50], Hamiltonian and the density matrix can be written as:

$$\mathscr{H}_{int}(t) = e^{\iota H_0 t}\mathscr{H}_{int}e^{-\iota H_0 t} \tag{2.13}$$

$$\rho^{(I)}(t) = e^{\iota H_0 t}e^{-\iota \mathscr{H} t}\rho e^{\iota \mathscr{H} t}e^{-\iota H_0 t} \tag{2.14}$$

where, $H_0 = \mathscr{H}_S + \mathscr{H}_B$ is the total free Hamiltonian. The time evolution for this system in the interaction picture can be written with the Liouville–von Neumann equation as:

$$\frac{d\rho^{(I)}(t)}{dt} = -\iota[\mathscr{H}_{int}(t), \rho^{(I)}(t)] \tag{2.15}$$

Integrating the above equation and then substituting the integral for $\rho^{(I)}(t)$ in the RHS of Eq. (2.15) we get:

$$\frac{d\rho^{(I)}(t)}{dt} = (-\iota)[\mathscr{H}_{int}(t), \rho^{(I)}(0)] + (-\iota)^2 \int_0^t dt^{'} [\mathscr{H}_{int}(t), [\mathscr{H}_{int}(t^{'}), \rho^{(I)}(t^{'})]]. \tag{2.16}$$

Performing a partial trace over reservoir degrees of freedom gives:

$$Tr_B\{\frac{d\rho^{(I)}(t)}{dt}\} = \frac{d\rho_S^{(I)}(t)}{dt} = -\int_0^t dt^{'} Tr_B\{[\mathscr{H}_{int}(t), [\mathscr{H}_{int}(t^{'}), \rho^{(I)}(t^{'})]]\} \tag{2.17}$$

Here, one can take $Tr_B\{[\mathscr{H}_{int}(t), \rho^{(I)}(0)]\}$ to be zero, provided the reservoir operators are shifted appropriately [50] . The above equation still depends on the total interaction picture density operator and is not time local ($\rho^I(t)$ is evaluated at all times between 0 to t), therefore to solve the above equation, one needs to make certain approximations, such as the Born and Markov approximation. The Born approximation takes away the dependence on the total interaction picture density operator and the Markov approximation renders Eq. (2.17) as a time local equation.

Born approximation

Under this approximation, the reservoir is assumed to be large and the system-reservoir coupling is assumed to be weak enough such that the reservoir is negligibly affected by the system-reservoir coupling and the total density operator remains in an approximate product state at all times:

$$\rho^{(I)}(t^{'}) \approx \rho_S^{(I)}(t^{'}) \otimes \rho_B. \tag{2.18}$$

Here, $\otimes$ denotes the tensor product.

Markov approximation

Under this approximation, the reservoirs become "memory-less", i.e. the reservoir correlation functions decay on a timescale shorter than the characteristic timescale τ_S, associated with the system dynamics over which the interaction picture density operator can change. The first consequence of this approximation is that we can replace $\rho_S^{(I)}(t')$ with $\rho_S^{(I)}(t)$. This gives us the Redfield quantum master equation which can be written as:

$$\frac{d\rho_S^{(I)}(t)}{dt} = -\int_0^t dt' Tr_B\{[\mathscr{H}_{int}(t), [\mathscr{H}_{int}(t'), \rho_S^{(I)}(t) \otimes \rho_B]]\}. \tag{2.19}$$

With the substitution: $t' = t - \tau$, the Redfield equation above can be further simplified as:

$$\frac{d\rho_S^{(I)}(t)}{dt} = -\int_0^\infty d\tau Tr_B\{[\mathscr{H}_{int}(t), [\mathscr{H}_{int}(t-\tau), \rho_S^{(I)}(t) \otimes \rho_B]]\}, \tag{2.20}$$

where the limit of integration has been extended to infinity.

Redfield quantum master equation: To connect with the RQME we use in chapter 4, we define $\mathscr{H}_{int}(t)$ as:

$$\mathscr{H}_{int}(t) = \Sigma_\mu (X_\mu(t) \otimes Y_\mu(t)), \tag{2.21}$$

here $X_\mu(t)$ represents the system operators, $Y_\mu(t)$ represents the reservoir operators and μ indexes over the different reservoirs. This is considered as the interaction Hamiltonian in Eq. (2.17) and the system-reservoir correlation function is defined as:

$$\Gamma^\beta_{\mu,\nu}(t) = Tr_B(e^{\iota \mathscr{H}_B t} e^{-\iota Y_\mu \mathscr{H}_B t} Y_\nu e^{-\beta \mathscr{H}_B})/Tr_B(e^{-\beta \mathscr{H}_B}), \tag{2.22}$$

here $\beta = 1/k_B T$ is the inverse temperature of the reservoir. With these system and reservoir operators, the Schrödinger picture equivalent of Eq. (2.20) is:

$$\frac{d\rho(t)}{dt} = \iota[\rho(t), \mathscr{H}_S] + \Sigma_{\mu,\nu} \int_0^\infty d\tau \Gamma^\beta_{\mu,\nu}(\tau)[X_{\mu,\nu}(-\tau)\rho(t), X_{\mu,\nu}] + h.c. \tag{2.23}$$

Lindblad quantum master equation: Now, one may obtain the the LQME from a phenomenological equation [51, 54–56] derived from the Kraus operator formalism [51]. This derivation may not provide all the microscopic details such as the interaction and reservoir Hamiltonian but for the purpose of this thesis, it is this phenomenological LQME that we will use.

LQME from Kraus operator representation:

We follow Ref. [50, 51, 57] to outline the steps to get to a phenomenological LQME. The evolution of the reduced density matrix of a system can be written in terms of a map connecting the initial density matrix to the evolved one as:

$$\rho(t) = \mathcal{M}[\rho(0)], \tag{2.24}$$

where the mapping $\mathcal{M} = \{\mathcal{M}_k\}$ is linear and constructed such that it preserves the positivity, trace and hermiticity of the density matrix [57] and k over all the possible transitions (dephasing, damping, depolarization etc.) that a system may undergo due to its interaction with a reservoir. In the Kraus operator representation [50, 51], the evolution of the reduced density matrix of the system can be written in terms of the Kraus operators $\mathcal{M}_k$ as:

$$\rho(t+\delta t) = \sum_k \mathcal{M}_k(\delta t)\rho(t)\mathcal{M}_k^\dagger(\delta t). \tag{2.25}$$

Here, taking the infinitesimal time limit while keeping only the first order terms, the Kraus operators can be defined as [50, 57]:

$$\mathcal{M}_0 = \mathbb{I} + \delta t(-\imath\mathscr{H} + K), \qquad \mathcal{M}_k = \sqrt{\delta t}\mathcal{L}_k, \tag{2.26}$$

Here, $\mathcal{M}_0$ describes how the system evolves when no quantum jumps take place, $\mathcal{L}_k$ are quantum jump operators or Lindblad operators [58] and for $\rho(t+\delta t)$ to remain hermitian, K needs to be a hermitian operator [50]. Hence Eq. (2.25) can be written as:

$$\rho(t+\delta t) = \rho(t) + \delta t\delta\rho = \mathcal{M}_0\rho(t)\mathcal{M}_0^\dagger + \sum_{k>0}\mathcal{M}_k\rho(t)\mathcal{M}_k^\dagger. \tag{2.27}$$

Here, $K = -1/2(\sum_{k>0}\mathcal{L}_k^\dagger\mathcal{L}_k)$ to satisfy the Kraus sum normalization [50]. Substituting K and taking the limit $\lim_{\delta\to 0}(\rho(t)+\delta t\delta\rho) = \rho(t)+dt\dot{\rho}$, Eq. (2.27) takes the form of a LQME:

$$\dot{\rho}(t) = -\iota[\mathscr{H},\rho(t)] + \sum_{k=1}^{M}\left(L_k\rho(t)L_k^\dagger - 1/2\{L_k^\dagger L_k,\rho(t)\}\right). \tag{2.28}$$

Here, $\{A,B\}$ represents the anti-commutator of operators A and B. Limited versions of the LQME can be obtained from the Redfield quantum master equation [39, 49, 59, 60] by applying certain approximations. For sake of completion, we will briefly discuss the type of approximation and the corresponding final form of the LQME obtained.

Secular approximation

For this approximation, the system Hamiltonian is first expressed in the energy eigenbasis $\mathscr{H}_S = \sum_i E_i |E_i\rangle\langle E_i|$. Then the system operator can be expressed as:

$$X_\mu(\tau) = \sum_{(E_i-E_j=\omega')} X(\omega')e^{-\iota\omega'\tau}. \tag{2.29}$$

Here we define the Fourier transform $\Gamma_{\mu,\nu}(\omega') = \int_0^\infty d\tau\Gamma_{\mu,\nu}(\tau)$, and collect all the time dependence, such that the interaction picture equivalent of Eq. (2.23) becomes:

$$\frac{d\rho_S^{(I)}(t)}{dt} = -\sum_{\mu,\nu}\sum_{\omega',\omega''}\Gamma_{\mu,\nu}(\omega')e^{-\iota(\omega''-\omega')t}[X_\mu^\dagger(\omega''),X_\nu(\omega')\rho_S^{(I)}(t)] + h.c. \tag{2.30}$$

Now application of the secular approximation to the above RQME implies that the fast rotating terms ($\omega' \neq \omega''$) can be neglected. Following Ref. [50, 59], this in Schrödinger picture gives us the global LQME:

$$\frac{d\rho(t)}{dt} = \iota[\rho,\mathscr{H}_S] + \Sigma_{\mu,\nu}\gamma_{\mu,\nu}(\omega')(X_\mu(\omega')\rho, X_\nu^\dagger(\omega') - \frac{1}{2}\{X_\nu^\dagger(\omega')X_\mu(\omega'),\rho\}), \tag{2.31}$$

where $\gamma_{\mu,\nu}(\omega') = \Gamma_{\mu,\nu}(\omega') + \Gamma^{*}_{\nu,\mu}(\omega')$ [50] which according to Ref. [61] is equivalent to retrieving $\gamma_{\mu,\nu}$ from $\Gamma_{\mu,\nu}(\tau) = \gamma_{\mu,\nu}\delta(\tau+0)$ when the Fourier transform of the reservoir correlations are defined appropriately.

Weak internal coupling approximation

In the case of a Bose-Hubbard Hamiltonian which has an onsite potential term ($\sim \Omega_0$), tunneling related terms ($\sim t_{ij}$) and a term for onsite interactions U, with the weak internal coupling approximation one can assume that ($\Omega_0 > t_{ij}$), all the tunnelling coefficients are weaker compared to the onsite frequency such that the system dynamics in the non-unitary evolution of the reduced density matrix can be approximated with just the onsite-frequency term instead of the system Hamiltonian. With this the local LQME in the Schrödinger picture [59, 61] can be written as:

$$\frac{d\rho(t)}{dt} = \iota[\rho, \mathscr{H}_S] + \Sigma_{\mu,\nu}\gamma_{\mu,\nu}(X_\mu\rho, X^{\dagger}_{\nu} - \frac{1}{2}\{X^{\dagger}_{\nu}X_\mu, \rho\}). \tag{2.32}$$

For a bosonic system, the density matrix can be infinite as a single site can accommodate an infinite number of bosons. However, due to limited resources such as memory and time, numerical simulations of bosonic systems use a truncated space where the maximum number of bosons per site is limited. The algorithm [62] for construction of this truncated basis has been outlined in Appendix A.1. The LQME is a deterministic differential equation, hence for its integration one can use higher-order algorithms like fourth-order Runge-Kutta method. Unlike in the case for stochastic equations, where going to higher-order methodology requires calculation of specific correlations between the random numbers depending on the type of noise used.

This truncation of Fock space usually turns out to be a good approximation qualitatively [63]. However, for a true qualitative and quantitative picture of the system in the untruncated Fock space we use the third quantization formalism introduced in the following section.

2.2.2 Third quantization

Third quantization formalism is designed to study open systems with non-interacting Hamiltonians coupled to a reservoir through linear operators. The space in which the system density matrix for an open quantum system resides is known as the Liouville space and $\mathscr{L}$, commonly referred to as the Liouvillean, is the generator of the open quantum system:

$$\frac{\partial \rho(T)}{\partial T} = \mathscr{L}\rho(T). \tag{2.33}$$

In the third quantization formalism, Prosen [64,65] canonically quantizes the Liouville space for open bosonic systems. By introducing specific mappings for left and right multiplication maps in the operator space, the Liouvillean is diagonalized. With the diagonalization of the Liouvillean one can obtain the non-equilibrium stationary state correlations by solving the Lyapunov equation for the system. The formalism provides complete information on the steady state correlations in the untruncated Fock space.

Following Ref. [64] we give a brief overview of the process of third quantization. The authors introduce a dual vector space $\mathcal{K}, \mathcal{K}'$ where $\mathcal{K}$ contains trace class operators, whose element is represented as $|\rho\rangle$ and $\mathcal{K}'$ contains the unbounded, physical operators whose element is represented as $(X|$. Over this dual space, the authors define 4K maps for the left and right multiplication:

$$\begin{aligned} \hat{a}_{0,j} &= f_j^L, \quad \hat{a}^{'}_{0,j} = \alpha(d_j^L - d_j^R), \\ \hat{a}_{1,j} &= d_j^R, \quad \hat{a}^{'}_{1,j} = \alpha(f_j^R - f_j^L), \end{aligned} \tag{2.34}$$

where j goes from 1 to the number of sites, K. f_j, d_k satisfy a known commutation relation and α is a constant that depends on the commutation relation. For example, a system of harmonic oscillators described in the coordinate-momentum space satisfies $[q_j, p_k] = \iota\delta_{j,k}$ which leads to $\alpha = \iota$. In the second quantization framework, for the associated unit energy quanta of an oscillator, the oscillators satisfy $[c_j, c_k^\dagger] = \delta_{j,k}$ with $q_j = (c_j^\dagger + c_j)/\sqrt{2}$ and $p_j = \iota(c_j^\dagger - c_j)/\sqrt{2}$ which leads to an $\alpha = 1$. These 4K mappings are defined such that they satisfy the following commutation relation:

$$[\hat{a}_{\nu,j}, \hat{a}^{'}_{\mu,k}] = \delta_{\mu,\nu}\delta_{j,k} \qquad [\hat{a}_{\nu,j}, \hat{a}_{\mu,k}] = [\hat{a}^{'}_{\nu,j}, \hat{a}^{'}_{\mu,k}] = 0. \tag{2.35}$$

The authors call the above commutation relations as the almost-commutation relation to distinguish them from the second quantization bosonic commutation relation. These maps are defined such that the identity operator $(1|$ is left annihilated $(1|\hat{a}^{'}_{\mu,k} = 0$ and the vacuum pure state $|\rho_0\rangle$ is right annihilated, $\hat{a}_{\mu,k}\,|\rho_0\rangle = 0$. With the construction of these 4K multiplication maps, a dual, bi-orthonormal Fock space can be formulated for the dual vector spaces:

$$|m\rangle = \Pi_{\nu,j}\frac{(\hat{a}^{'}_{\nu,j})^{(m_{\nu,j})}}{\sqrt{m_{\nu,j}!}}\,|\rho_0\rangle \qquad (m| = (1|\Pi_{\nu,j}\frac{(\hat{a}_{\nu,j})^{(m_{\nu,j})}}{\sqrt{m_{\nu,j}!}} \tag{2.36}$$

Following the algebra introduced above, the respective master equations of the open quantum system 2.33 are recast in terms of the almost-commutation relation such that the Liouvillean of the open quantum system can be written in the following quadratic form:

$$\mathscr{L} = b.\boldsymbol{S}b - \boldsymbol{S_0}\mathbb{I}, \tag{2.37}$$

where $b = (\hat{a}_0, \hat{a}_1, \hat{a}^{'}_0, \hat{a}^{'}_1)^T$, with $\boldsymbol{S}$:

$$\boldsymbol{S} = \begin{pmatrix} 0 & -\boldsymbol{X} \\ -\boldsymbol{X}^T & \boldsymbol{Y} \end{pmatrix}, \tag{2.38}$$

and $\boldsymbol{S_0}$ as a scalar. The $\boldsymbol{X}$ and $\boldsymbol{Y}$ matrices are constructed using the system Hamiltonian, system-reservoir coupling and reservoir spectral function and hence will be different for different forms of the Hamiltonian and quantum master equations. Once $\boldsymbol{X}$ and $\boldsymbol{Y}$ are known, solving the Lyapunov equation $\boldsymbol{X}^T\boldsymbol{Z} + \boldsymbol{Z}\boldsymbol{X} = \boldsymbol{Y}$ will give us the non-equilibrium steady-state correlation matrix $\boldsymbol{Z}$.

In appendix A.3 we show the step by step process to apply third quantization to the Redfield quantum master equation [65]. From this canonical quantization process, we derive the Lyapunov equation for the non-equilibrium steady state coordinate-momentum correlation matrix. Following Ref. [63, 64] in appendix A.4 we show the application of third quantization to the LQME.

Chapter 3

Geometry-induced atypical thermal current

The work presented in this chapter has been published in **Physical Review E** 99 (2019): 022131 as:
"Geometry-induced local thermal current from cold to hot in a classical harmonic system."
Authors: Palak Dugar and Chih-Chun Chien

Ohm's law predicts the flow of electrical current when subjected to the potential difference and the strength of the current is proportional to the gradient of electric potential. In a classical circuit governed by Ohm's law, the direction of the total current is constrained by the direction of the potential gradient.When a temperature gradient is applied to a system, thermodynamical laws forbid an overall current from a cold to hot body without any other changes [66]. However, nothing prohibits a local thermal current to go from a cold to hot body [6]. We study a minimal system of three classical harmonic oscillator and show how coupling the oscillators in a multi-path geometry can result in interesting transport behavior. We show that this simple system in conjunction with Langevin reservoirs is capable of showing a local thermal current which goes from a cold to hot site. We refer to this cold-to-hot local current as atypical current.

We outline the model and the formalism to study atypical transport in sec. 3.1. In the next section, we show the analytical formula and present the numerical results for our system. From our numerical results shown in sec. 3.2.2 we unambiguously demonstrate a local atypical thermal current from cold to hot. This is followed by a discussion on the robust nature of the atypical local current against asymmetric system-reservoir coupling, nonlinear effects and additions of more masses and springs.

3.1 Model to study transport in a classical harmonic multi-path system

We consider a system of three masses m_1, m_2, and m_3 connected by some springs and coupled to two Langevin reservoirs at different temperatures, as illustrated in Fig. 3.1. We only consider the motion of the masses in one transverse direction labeled by their displacements x_n with $n = 1, 2, 3$. The system is described by Newtonian mechanics with the Hamiltonian:

$$\mathscr{H} = \sum_n [\frac{1}{2} m_n \dot{x}_n^2 + V(x_n - x_{n+1}) + U(x_n)], \tag{3.1}$$

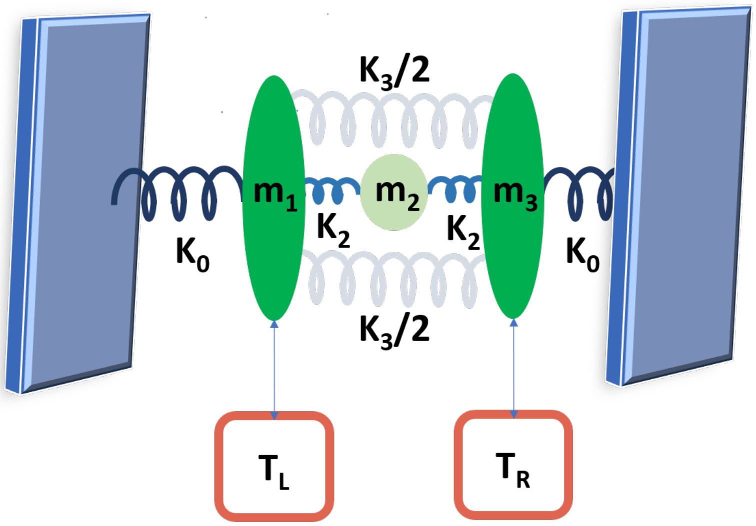

Figure 3.1: Schematics for the classical mass-spring system coupled to Langevin reservoirs (red square boxes) at temperatures T_L and T_R, respectively. m_1 and m_3 are connected to hard walls (the slabs) via springs with spring constant K_0 and to each other with two springs with spring constant $K_3/2$. m_2 is connected to both m_1 and m_3 through springs with spring constant K_2.

where V is the nearest-neighbor interaction potential and U is the on-site nonlinear potential. The system is harmonically coupled to two hard-walls with spring constant K_0. The hard-walls essentially confine the system such that we can take $x_0 = 0$ and $x_4 = 0$. These hard-walls prevent overall translational motions of the entire system [67].

We focus on harmonic couplings between the masses, while the coupling to the substrate is described by a nonlinear onsite potential [68,69] $U(x_n) = \frac{1}{4}gx_n^4$ with g as its coupling strength. Explicitly, the potentials of the three masses have the following forms:

$$\begin{aligned}
(V+U)_1 &= \frac{K_0}{2}(x_1-x_0)^2 + \frac{K_2}{2}(x_1-x_2)^2 + \frac{K_3}{2}(x_1-x_3)^2 + \frac{g}{4}(x_1)^4, \\
(V+U)_2 &= \frac{K_2}{2}(x_2-x_1)^2 + \frac{K_2}{2}(x_2-x_3)^2 + \frac{g}{4}(x_2)^4, \\
(V+U)_3 &= \frac{K_0}{2}(x_3-x_4)^2 + \frac{K_2}{2}(x_3-x_2)^2 + \frac{K_3}{2}(x_3-x_1)^2 + \frac{g}{4}(x_3)^4. \quad (3.2)
\end{aligned}$$

Here K_2 is the spring constant of the spring connecting m_2 to both m_1 and m_3, and $K_3/2$ is the spring constant of the two identical springs connecting m_1 and m_3 directly.

Thermal transport through the system is driven by coupling it to two reservoirs at temperatures T_L and T_R. We consider the Langevin reservoirs [32, 70, 71] introduced in chapter 2. The equations of motion [72] for the classical multi-path system coupled to Langevin reservoirs are

$$\begin{aligned} m_{1,3}\ddot{x}_{1,3} &= F_{1,3} - b_{L,R}\dot{x}_{1,3} + \eta_{L,R}(t), \\ m_2\ddot{x}_2 &= F_2. \end{aligned} \tag{3.3}$$

Here $F_n = -\partial(U+V)_n/\partial x_n$ denotes the deterministic force on the n-th mass. The subscripts L and R denote the left and right reservoirs, respectively. $b_{L,R}$ is the friction coefficient coupling the system to the left and right reservoir, and $\eta_{L,R}(t)$ is the force from the left and right reservoirs. The random forces $\eta_{L,R}(t)$ have a zero mean $\langle \eta_{L,R}(t)\rangle = 0$ and satisfy the fluctuation-dissipation relation of the first kind [32, 41] introduced in sec. (2.1):

$$\langle \eta_{L,R}(t_1)\eta_{L,R}(t_2)\rangle = 2bk_BT_{L,R}\delta(t_1 - t_2), \tag{3.4}$$

where k_B is the Boltzmann constant. In the following discussion, we keep $m_1 = m_3 = m$ and $K_0 = K_3 = K$. We will show that in the parameter regime we consider, using slightly different values of b_L and b_R does not change the results qualitatively. Hence, unless stated otherwise we will use the symmetric system-reservoir coupling, $b_L = b_R = b$.

The local thermal current from site i to site j can be defined using the continuity equation [40]. The general definition is $\langle J_{ij}\rangle = \langle F_{ij}\dot{x}_j\rangle$, where F_{ij} is the force acting on mass j due to mass i and $\langle\rangle$ denotes the average over an ensemble of independent random realizations. Using the equations of motion and the definition of current between two sites, the explicit form of the total thermal current from m_1 to m_3 is

$$\langle J_{13}\rangle = \langle \dot{x}_3(K_2x_2 + K_3x_1)\rangle. \tag{3.5}$$

Similarly, we can find the local current flowing from m_1 to m_2, which written explicitly is:

$$\langle J_{12} \rangle = \langle \dot{x}_2 (K_2 x_1) \rangle. \tag{3.6}$$

For a harmonic system in the steady state, the currents should satisfy $\langle J_{ij} \rangle = -\langle J_{ji} \rangle$. Additionally for our system, the current through m_2 should $\langle J_{12} \rangle = \langle J_{23} \rangle$ in the steady state.

In our work, we use the first-order Euler-Maruyama method [45] and the second-order method [46] to numerically simulate Langevin equation. The above methods and simulation process for the white noise follows the protocol outlined in section 2.1. In the absence of substrate effects, in general the results from those methods are indistinguishable. However, to simulate substrate effects we choose the full second-order method as it gives steady state results for a smaller simulation time. The time step size in our simulations is $\Delta t/t_0 = 10^{-4}$. We present the results averaged over an ensemble of 1600 independent realizations. To ensure that the system is in the steady-state regime, we monitor the time evolution of the thermal current and wait until the transient behavior decays away. In general, we start taking the steady-state value after $t > 300t_0$ and then average the value over a time period of $\tau/t_0 = 500$ afterwards. Importantly, we have checked there is no energy accumulation in the system in the steady state by verifying the thermal current coming into each mass equals the current out of each mass. Unless specified otherwise, the reservoirs were maintained at $T_L/T_0 = 2$ and $T_R/T_0 = 1$. We show the direction of the steady state thermal current through m_2 as a function of K_2/K_3, m_2/m_3, $b_{L,R}$, and g.

For numerical simulation of our model, we construct dimensionless quantities using m, K, k_B, and $\hbar$. For instance, the units of energy, temperature, time, angular frequency, length, thermal current, system-reservoir coupling, and system-substrate coupling are $E_0 = \hbar\sqrt{\frac{K}{m}}$, $T_0 = \frac{\hbar}{k_B}\sqrt{\frac{K}{m}}$, $t_0 = \sqrt{\frac{m}{K}}$, $\omega_0 = \sqrt{\frac{K}{m}}$, $l_0 = \sqrt{\frac{\hbar}{\sqrt{mk}}}$, $J_0 = \hbar\frac{K}{m}$, $b_0 = \sqrt{mK}$, and $g_0 = \frac{\sqrt{mK^3}}{\hbar}$, respectively. The setup of Fig. 3.1 is generic and may be applicable to molecular or nano-mechanical systems in the classical regime [73, 74], or even macroscopic objects as long as the Langevin equation (3.3) applies. The numerical parameters would result in a nano system [75, 76] with $m \simeq 10^{-26}$ kg,

$\sqrt{\frac{K}{m}} \simeq 10^{12}$ rad/s, $l_0 \simeq 10^{-10}$ m subject to an ambient temperature, T_0 around $73K$.

3.2 Results

3.2.1 Analytic formula for total current

We will start our investigation of thermal currents with the harmonic case without any substrate effects $g = 0$. A general formalism for the thermal current and conductance of harmonic systems coupled to Langevin reservoirs can be found in refs. [32, 77]. For a classical system consisting of N masses coupled by harmonic springs whose ends are under contact with two Langevin reservoirs which provide a temperature difference of $\Delta T = T_L - T_R$, the total thermal current is given by

$$J = \Delta T b_L b_R \int_{-\infty}^{\infty} \frac{d\omega}{\pi} \omega^2 |[Z^{-1}(\omega)]_{1N}|^2 \tag{3.7}$$

In this formalism, a force matrix Φ which specifies the harmonic couplings between pairs of masses, a mass matrix M which is constructed with the masses $m_1, m_2, ..., m_N$ on the diagonal and a B matrix which has only two nonvanishing elements $B_{11} = b_L$ and $B_{NN} = b_R$ are used to build the matrix, $Z = \Phi - M\ddot{\omega} - i\omega B$. Following Ref. [77], the total thermal current can be written as:

$$\begin{aligned} J &= \Delta T b_L b_R \int_{-\infty}^{\infty} \frac{d\omega}{\pi} \omega^2 |C_{1N}|^2 [(K_{1,N} - \omega^2 b_L b_R K_{2,N-1})^2 \\ &\quad + \omega^2 (b_R K_{1,N-1} + b_L K_{2,N})^2]^{-1}. \end{aligned} \tag{3.8}$$

Here, $K_{i,j}$ denotes the determinant of the matrix from the i-th row (column) to the j-th row (column) of the matrix $(\Phi - M\omega^2)$. C_{1N} is the cofactor of the $(1, N)$-th element of Z. For the setup shown in Fig. 3.1, the force matrix is

$$\Phi = \begin{pmatrix} K_0 + K_2 + K_3 & -K_2 & -K_3 \\ -K_2 & 2K_2 & -K_2 \\ -K_3 & -K_2 & K_0 + K_2 + K_3 \end{pmatrix}. \tag{3.9}$$

The numerical value of the total thermal current J_{13} flowing through the classical system shown in Fig. 3.1 can be obtain from Eq. (3.8) after one calculates the cofactor and determinants needed. Expressions based on Eq. (3.8) are available for specific types of 1D harmonic chains in the infinite-chain limit [77–80].

Fig. 3.2 shows the total thermal current J_{13} as a function of m_2/m_3 and K_2/K_3 according to Eq. (3.8) with $m_1 = m_3$, $K_0 = K_1 = K_3$, $\Delta T/T_0 = 1$, and selected values of $b_L = b_R = b$. When b is small, for instance $b/b_0 = 0.1$, one observes that the surface of J_{13} exhibits a dip, implying a non-monotonic dependence of J_{13} on the parameters m_2/m_3 and K_2/K_3. However, as b is increased the dip disappears. We have checked the more general cases with $0.5 \leq b_L/b_R \leq 2$, and made sure that the total current has the same qualitative behavior with the presence of a dip (or no dip) when b_L, b_R are small. At this stage, the dip of J_{13} may look mysterious. In the next section, we will show by numerically analyzing the local thermal current through each path, that the dip of the total thermal current is associated with a local atypical thermal current flowing through the mass m_2 from cold to hot.

3.2.2 Atypical local current

The results we will present only depend quantitatively on K_0, and all the conclusions are insensitive to K_0. The non-monotonic behaviour of the total thermal current seen in Fig. 3.2 is rooted in an interesting phenomenon of a local thermal current flowing opposite to the total current which we will refer to as atypical current. We take the nonlinear substrate coupling strength g to zero and numerically calculate the total and local currents in the harmonic system. Fig. 3.3 (a) shows the total, J_{13} and (b) shows the local steady state current, J_{12} for $b_L = b_R = b = 0.1b_0$. The insets of Fig. 3.3 (a) and (b) show the corresponding total and local currents for $b_L = b_R = b = 1.0b_0$. We emphasize that the steady-state values are taken after $t > 300t_0$ to ensure the transient behavior has decayed away. The opposite directions of J_{13} and J_{12} in the steady state for the case with $b/b_0 = 0.1$ unambiguously demonstrate the existence of a local atypical thermal current from cold to hot. The insets of Fig. 3.3 (a) and (b) show the typical, normal behavior obtained for $b/b_0 = 1.0$, where J_{12} and J_{13} show

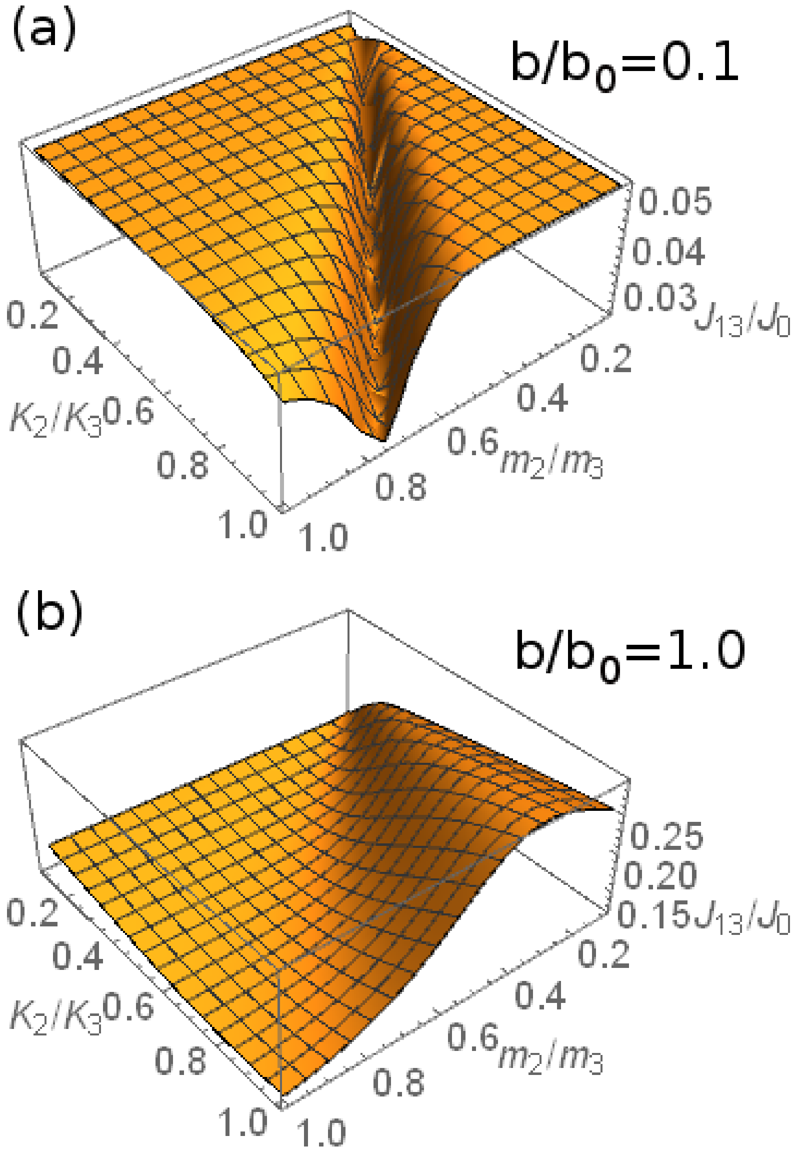

Figure 3.2: Total thermal current J_{13} through the harmonic system shown in Fig. 3.1, according to the analytic formula, Eq. (3.8). Here $b_L = b_R = b$, $m_1/m_3 = 1$, $K_0/K_3 = K_1/K_3 = 1$, $g = 0$, $\Delta T/T_0 = 1$, and $b/b_0 = 0.1$ for (a) and $b/b_0 = 1.0$ for (b).

the direction of flow in the steady state. We found that, in general, the local thermal current through m_2 can flow from cold to hot only in the weakly coupled regime when b/b_0 is small compared to the other system parameters. The dependence of the

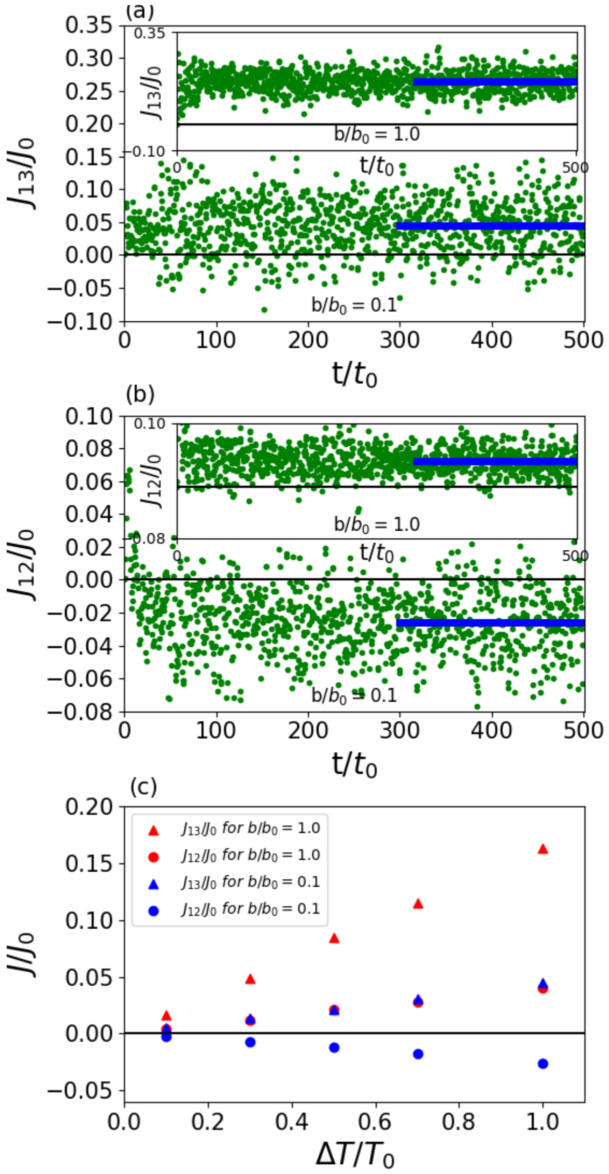

Figure 3.3: (a) The total thermal current J_{13} and (b) the local thermal current J_{12} through m_2 with $b/b_0 = 0.1$, showing the local atypical current from cold to hot. The insets present the corresponding quantities for the case with $b/b_0 = 1.0$, showing all currents flowing from hot to cold. The dots show the average over 1600 realizations. The thick blue lines show the average over a period of $500t_0$ in the steady state ($t > 300t_0$). Here $K_2/K_3 = 0.35$, $m_2/m_3 = 0.3$, $\Delta T/T_0 = 1$, and $g/g_0 = 0$. (c) The total and local thermal currents vs. ΔT for the two cases shown in (a) and (b).

thermal current of a one-dimensional (1D) harmonic system on b has been studied in Refs. [40, 81], but the setup shown in Fig. 3.1 is not a simple 1D system.

To verify the local thermal current from cold to hot is not an artifact, we vary the temperature difference ΔT between the two reservoirs and demonstrate that both the normal and atypical local current indeed scale linearly with $\Delta T/T_0$ just like the total current. This result shown in Fig. 3.3 (c) firmly establishes the existence of a local atypical thermal current from cold to hot in a simple classical harmonic system driven by Langevin reservoirs.

While T_L and T_R are fixed, sweeping the values of $(K_2/K_3, m_2/m_3)$ in the parameter space for small b/b_0, we have found that the steady-state thermal current through m_2 can flow either in the direction of m_1 to m_3 i.e. normal (hot to cold) or opposite to it i.e. atypical (cold to hot). Away from the small b/b_0 regime, the system only exhibits the normal behavior for reasonable values of m_2/m_3 and K_2/K_3. The dependence of J_{12} on b is illustrated in Fig. 3.4 (a) with the selected parameters $m_2/m_3 = 0.3$ and $K_2/K_3 = 0.35$.

For symmetric system reservoir coupling, $(b_R = b_L = b)/b_0$ as b/b_0 increases, J_{12} goes from being atypical to normal. Notably, there is a critical point ($b/b_0 \approx 0.4$ for this case), where the local current J_{12} vanishes in the steady state. We point out that there is still a thermal current flowing through the two springs coupling m_1 and m_3 directly, but the path through m_2 carries no thermal current in the steady state. Asymmetric system-reservoir couplings yields qualitatively the same results as the case with symmetric system-reservoir coupling as shown in Fig. 3.4 (a) as the local current J_{12} changes from the atypical to normal behavior as b_L increases. However, the choice of $b_R = (0.5, 1.0, 2.0)b_L$ does alter the value of the critical point where the local current changes its behavior.

We evaluate the local temperatures of the three masses and verify that m_1 is really hotter than m_2 in the steady state. The local temperature of mass j (with $j = 1, 2, 3$) is defined as

$$T_j = \frac{1}{k_B} m_j \langle v_j^2 \rangle. \tag{3.10}$$

In Fig. 3.4 (b), we show the steady-state local temperatures of the three masses as a

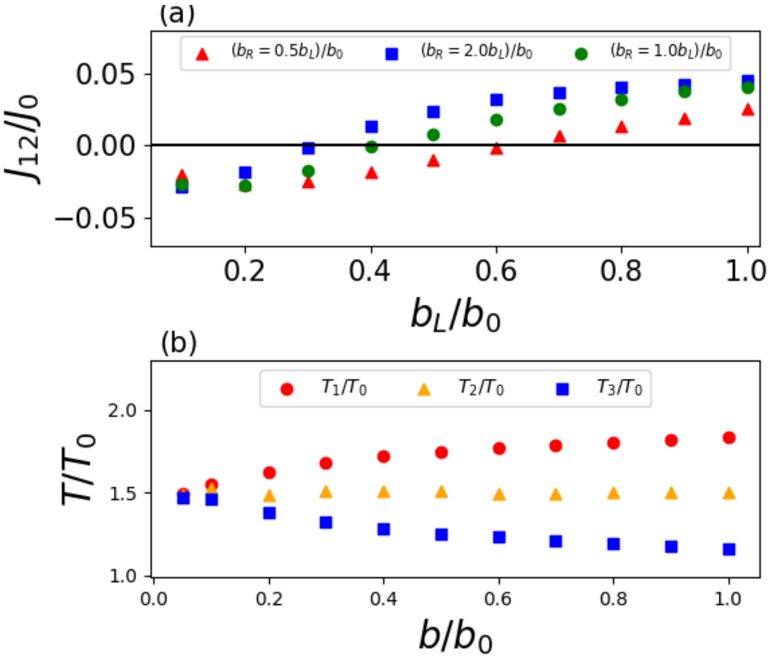

Figure 3.4: (a) The dependence of the local current J_{12} on the system-reservoir coupling b_L/b_0 for asymmetric couplings $b_R = 0.5b_L$ (triangles) and $b_R = 2.0b_L$ (squares) and symmetric coupling $b_R = b_L$ (circles). (b) The local temperatures of the three sites as functions of b/b_0 for the case of symmetric coupling in the steady state. Here $m_2/m_3 = 0.3$, $K_2/K_3 = 0.35$, $\Delta T/T_0 = 1$, and $g = 0$.

function of b for the case with symmetric system-reservoir coupling. One can see that regardless of the presence the atypical local thermal current, the local temperatures always follow $T_1 > T_2 > T_3$.

In Fig. 3.5 (a) we show the phase diagram of the system with $b/b_0 = 0.1$, where the blue triangles (red dots) indicate the parameters at which the local thermal current through m_2 is atypical (normal) when $b/b_0 = 0.1$. Increasing b/b_0 in the atypical regime always drives the system from one with a local atypical current to one with only normal currents, similar to the result shown in Fig. 3.4 (a). On the other hand, varying m_2/m_3 and K_2/K_3 leads to more complicated behavior of the local current and the atypical regime may be sandwiched in between the normal regimes.

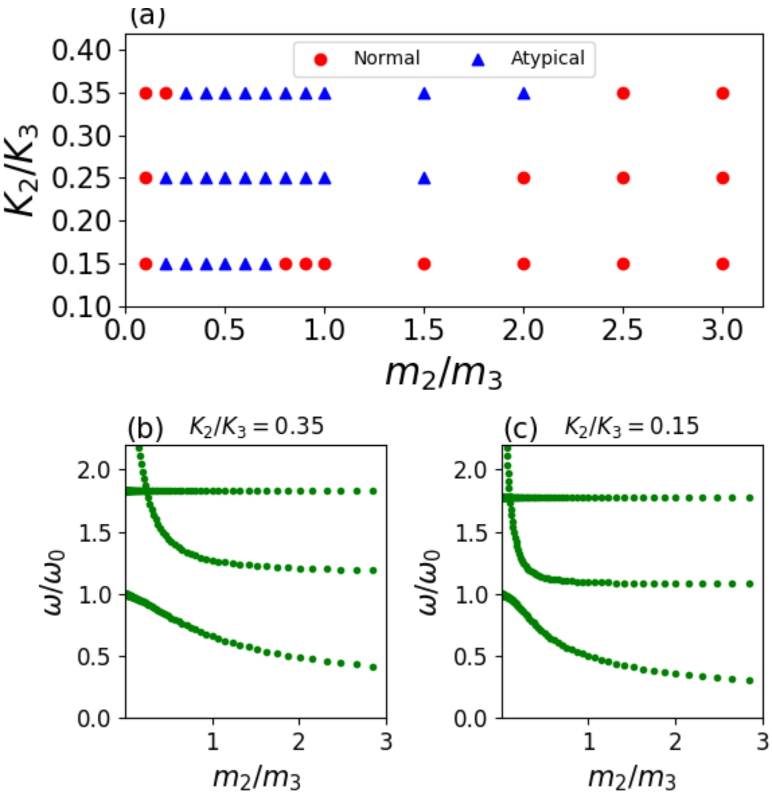

Figure 3.5: (a) Phase diagram showing where a local atypical thermal current from cold to hot can be found. The blue triangles (red dots) indicate where the local current is atypical (normal). Here $b/b_0 = 0.1$ and $g/g_0 = 0$. (b) and (c) show the normal mode frequencies, ω/ω_0, of the system shown in Fig. 3.1 without the reservoirs for (b) $K_2/K_3 = 0.35$ and (c) $K_2/K_3 = 0.15$.

The dependence of the direction of the local thermal current on the system-reservoir coupling b, shown in Fig. 3.4 (a), indicates the mechanism behind the atypical local current is not an intrinsic property of the harmonic system. To corroborate the observation, we evaluate the normal-mode frequencies of the harmonic system shown in Fig. 3.1 without the reservoirs and show the spectra in Fig. 3.5 (b) and (c) for two selected cases. As shown in Fig. 3.5 (b) and (c), the normal-mode frequencies for both values of K_2/K_3 exhibit level crossings. We found the locations of the level crossings are close to the left boundary of the region exhibiting the atypical current in the phase diagram shown in Fig. 3.5 (a). The observation that tuning the system-reservoir coupling b/b_0 can change the direction of the local thermal current even when m_2/m_3 and K_2/K_3 are fixed, as shown in Fig. 3.4 (a), coupled with the normal-mode frequencies shown in Fig. 3.5 (b) and (c) for parameters which show different behavior of local currents when attached to reservoirs we can claim that the atypical current is a combined effect of the system and reservoirs.

Moreover, the location of the dip in the total current from the analytic formula, shown in Fig. 3.2 (a), is close to the left boundary of the atypical regime shown in Fig. 3.5 (a) for small b/b_0. We found this to be the general case. One can use the dip in the total current from the analytic formula to estimate where the atypical local current emerges. There is no indication of the right boundary of the atypical regime from the analytic formula, though. Therefore, it may be insufficient to determine the whole atypical regime by analyzing the total thermal current or the normal-mode spectrum.

It is known that for quantum transport of electrons through a triangular quantum dot metastructure [25], the local atypical electric current is due to the combination of wave nature of quantum particles and multiple paths. Thermal transport in classical harmonic systems is carried by the normal modes of the oscillators coupled to the reservoirs. The normal modes may be viewed as mechanical waves. As one of the Langevin reservoir pumps in while the other takes out energy through the normal modes, there is no rule forbidding a path from overshooting the overall thermal current.

The conservation of charge in electronic transport imposes Kirchhoff's law requiring the net electric current through a node should be zero [82]. Similarly, in steady-state thermal transport the net thermal current through a mass in a harmonic system should vanish. Therefore, if an overshoot occurs along a path, another path will compensate for the excess thermal current by carrying the thermal current backward, resulting in an atypical local thermal current.

3.2.3 Atypical local current and nonlinear onsite potential

The harmonic system with the Langevin reservoirs is a linear system, allowing a detailed analysis of its dynamics. After establishing the local thermal current from cold to hot, we consider a nonlinear onsite potential $U(x_n) = (1/4)gx_n^4$ which mimicks the effect of coupling the system to a substrate [68,69]. In the presence of a nonlinear potential, the vibrational spectrum of the system cannot be always be described by the normal modes. Nevertheless, our simulations of the system with the nonlinear substrate effect using the second order method shows the direction of the local thermal current from cold to hot as a function of the onsite nonlinear potential.

Fig. 3.6 (a) and (b) show the phase diagrams of the system with $g/g_0 = 0.1$ and 0.5 at fixed system-reservoir coupling, $b/b_0 = 0.1$. The regime with a local atypical thermal current (the blue triangles) does not show any big changes as the interaction strength is changed. Therefore, we conclude that the atypical local thermal current is robust against the nonlinear onsite potential. The dependence on m_2/m_3 and K_2/K_3 shows similar behavior as the case with $g/g_0 = 0$. Fig. 3.6 (c) shows the dependence of the local thermal current J_{12} on the system-reservoir coupling for the symmetric ($b_L = b_R$) and asymmetric ($b_L \neq b_R$) cases for $m_2/m_3 = 0.9$, $K_2/K_3 = 0.35$, $\Delta T/T_0 = 1$, and $g/g_0 = 0.5$. Tuning the system-reservoir coupling in both the symmetric and asymmetric cases leads to a change in the behavior of the local thermal current. As the magnitude of the asymmetric system-reservoir coupling is increased the local current goes from atypical regime to the normal regime.

3.2.4 Robustness of atypical local current

We have shown that the atypical local thermal current in the steady state is robust against asymmetric system-reservoir coupling ($b_L \neq b_R$) in both the linear ($g/g_0 = 0$) and nonlinear ($g/g_0 = 0.1, 0.5$) cases, as demonstrated in Fig. 3.4 (a) and Fig. 3.6 (b,c). To show the robust nature of the atypical current we add another mass to the system such that a direct coupling between m_1 and m_3 in Fig. 3.1 is not present. The setup is illustrated in Fig. 3.7 (a), where m_1 and m_3 are coupled to each other through m_2 and m_4. Similar to Eq. (3.1) for the three oscillator system, the Hamiltonian for

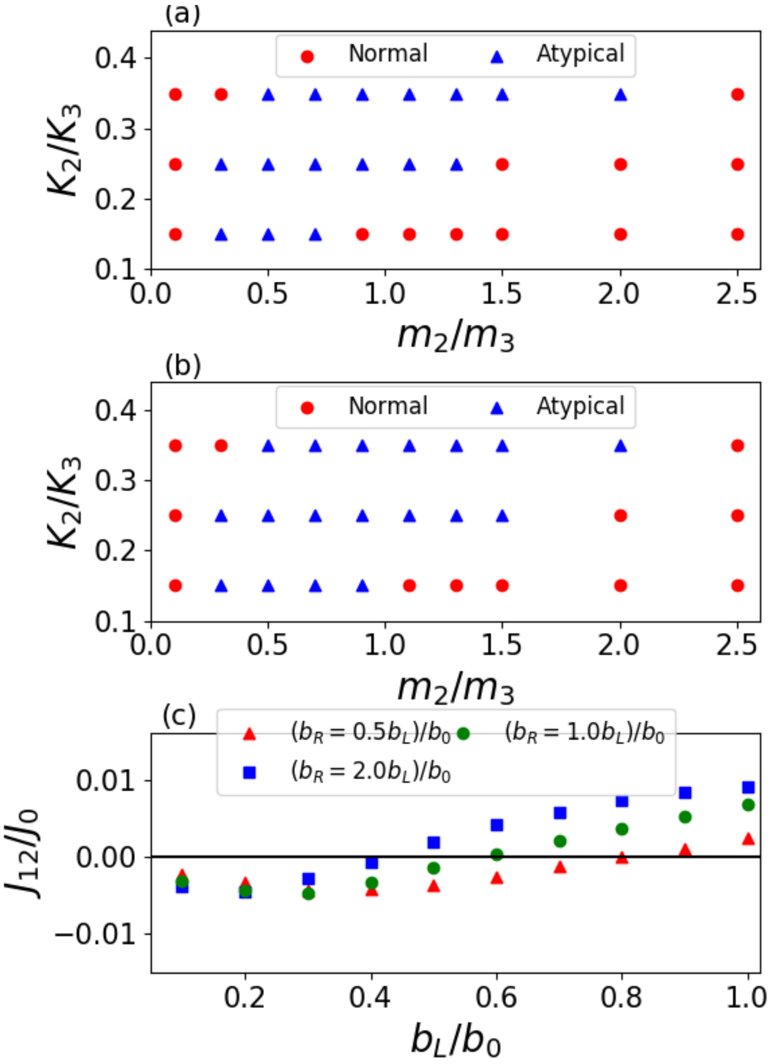

Figure 3.6: (a) and (b): Phase diagrams of the system with nonlinear substrate effect. Here $g/g_0 = 0.1$ in (a) and $g/g_0 = 0.5$ in (b). The blue triangles (red dots) show where a local thermal current from cold to hot can (cannot) be observed. Here $b/b_0 = 0.1$. (c) The local thermal current as a function of the system-reservoir coupling for the symmetric case with $b_R = b_L$ (circles) and asymmetric cases with $b_R = 0.5b_L$ (triangles) and $b_R = 2.0b_L$ (squares). Here $m_2/m_3 = 0.9$, $K_2/K_3 = 0.35$, $\Delta T/T_0 = 1$, and $g/g_0 = 0.5$.

this system is:

$$H_4 = \sum_{n=1}^{4}[\frac{1}{2}m_n\dot{x}_n^2 + V(x_n, x_{n+r}) + U(x_n)], \tag{3.11}$$

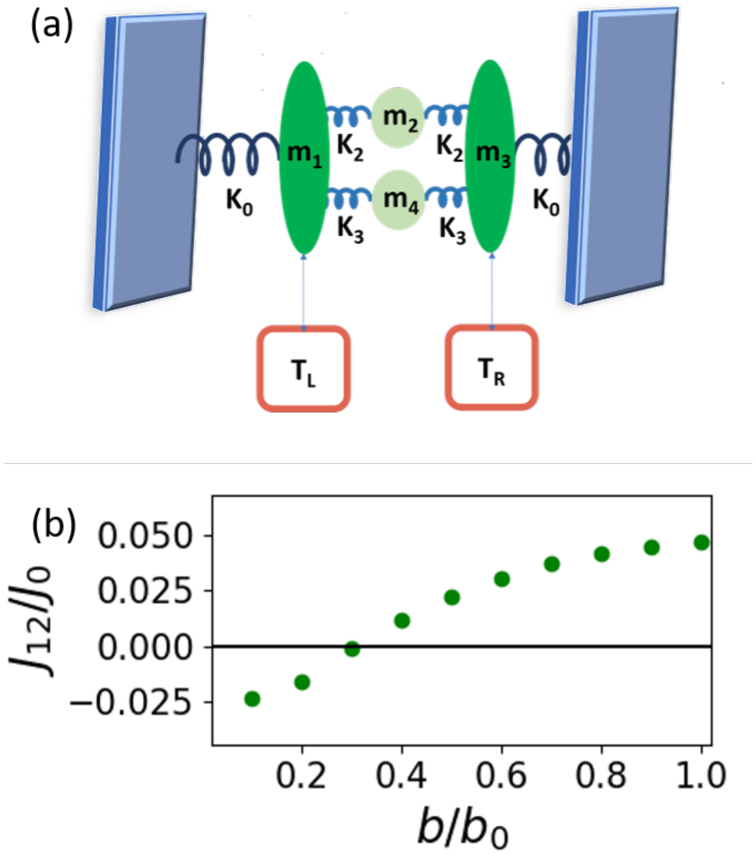

Figure 3.7: (a) schematic for a four-mass setup. The addition of m_4 avoids a direct coupling between m_1 and m_3, which are connected to the Langevin reservoirs at temperatures T_L and T_R, respectively. The convention follows Fig. 3.1. (b) The local thermal current J_{12} through m_2 in the steady state as a function of the symmetric system-reservoir coupling $b_R = b_L = b$. Here $m_1/m_3 = 1$, $m_2/m_3 = 0.4$, $m_4/m_3 = 0.5$, $K_0/K_3 = 1$, $K_2/K_3 = 0.35$, $\Delta T/T_0 = 1$, and $g = 0$.

where V and U denote the harmonic coupling and onsite potentials. Two hard-walls are introduced with $x_0 = x_5 = 0$. The potentials have the following forms:

$$\begin{aligned}
(V+U)_1 &= \frac{K_0}{2}(x_1 - x_0)^2 + \frac{K_2}{2}(x_1 - x_2)^2 + \frac{K_3}{2}(x_1 - x_4)^2 + \frac{g}{4}(x_1)^4, \\
(V+U)_2 &= \frac{K_2}{2}(x_2 - x_1)^2 + \frac{K_2}{2}(x_2 - x_3)^2 + \frac{g}{4}(x_2)^4, \\
(V+U)_3 &= \frac{K_0}{2}(x_3 - x_5)^2 + \frac{K_2}{2}(x_3 - x_2)^2 + \frac{K_3}{2}(x_3 - x_4)^2 + \frac{g}{4}(x_3)^4, \\
(V+U)_4 &= \frac{K_3}{2}(x_4 - x_1)^2 + \frac{K_3}{2}(x_4 - x_3)^2 + \frac{g}{4}(x_4)^4. \qquad (3.12)
\end{aligned}$$

Here K_2 is the spring constant of the two springs connecting m_2 to m_1 and m_3, and K_3 is the spring constant of the springs connecting m_4 to m_1 and m_3.

We implement the same protocol we followed for the system shown in Fig. 3.1 to numerically simulate the total and local currents for the four site system. For simplicity, we consider the harmonic case with fixed $m_1/m_3 = 1$, $K_0/K_3 = 1$ and $b_L = b_R = b$. Fig. 3.7 (b) shows the local thermal current flowing through m_2 in the steady state when $m_2/m_3 = 0.4$, $m_4/m_3 = 0.5$, and $K_2/K_3 = 0.35$ as a function of the system-reservoir coupling and show that the local atypical thermal current survives in a setup with no direct coupling between the two masses connected to the Langevin reservoirs. Moreover, the dependence of the local current on the system-reservoir coupling is similar to the result shown in Fig. 3.4 (a). Therefore, the local atypical thermal current is robust against asymmetry in the system-reservoir coupling, and additions of more masses and springs to the system.

3.3 Summary

To summarize we demonstrate a steady-state local thermal current from cold to hot in a multi-path system of classical harmonic oscillators subject to Langevin reservoirs at different temperatures while the total thermal current always follows the second law of thermodynamics, as it goes from hot to cold. The regime of the local atypical current is dependent on both the parameters of the harmonic system, and the coupling to the reservoirs. We show that the local atypical thermal current is robust against asymmetric system-reservoir coupling, nonlinearity and additions of more masses and springs.

Chapter 4

Quantum thermal transport

Motivated by the emergence of an atypical local thermal current in a classical harmonic system with a multi-path geometry, in this chapter we explore the implications of multiple pathways on the steady-state local quantum thermal current. We study a system of three quantum oscillators coupled in a way that they form a triangle. This triangular geometry provides the ‘multiple paths’, the essential ingredient for the system to exhibit an internal circulation of quantum thermal current. We describe the system of quantum oscillators in the coordinate-momentum space in the Redfield form and through a Bose-Hubbard model in Lindblad form of the quantum master equation respectively and show the presence of internal circulations in both these formalisms. Our goal for this chapter is not to establish a rigorous connection between the Hamiltonians and forms of the quantum master equation but to demonstrate the universal nature of the internal circulation of local thermal current in open quantum systems.

In section 4.1, we lay out the system Hamiltonian for the multi-path quantum oscillator system in the coordinate-momentum basis and through the Bose-Hubbard Hamiltonian. Each system of interest Hamiltonian representation is followed by a description of the quantum master equation employed to study the steady state thermal currents and the corresponding definitions of local thermal currents in both the approaches. In section 4.2, we present our third quantization results for the multi-path quantum oscillator system in the Redfield and Lindblad master equation formalism. We discuss the relevant parameter space in which these internal circulations are present and finally their behavior when interactions are added to the system. We summarize our results in section 4.3.

4.1 Models and methods

4.1.1 Quantum harmonic oscillators with RQME

Throughout this chapter, we take $\hbar = k_B = 1$. To investigate local quantum thermal transport in a multi-path geometry, we consider a minimal system of three quantum oscillators harmonically coupled to each other and to a substrate, as shown in Fig. 4.1 (a). We consider a simple set of parameters, but all the parameters may be tuned. All three quantum oscillators have the same mass, $m_j = m$. Following Ref. [65], the Hamiltonian of this system in the mass weighted coordinates can be written as:

$$\begin{aligned}\mathscr{H} =&\frac{1}{2}\sum_{j=1}^{3}(p_j^2+\omega_0^2 q_j^2)+\frac{k_3}{2m}(q_1-q_3)^2+\frac{k}{2m}\sum_{j=1}^{2}(q_j-q_{j+1})^2\\ =&\frac{1}{2}(p.p+q.\mathbf{Q}q).\end{aligned}$$

Here q_j and p_j with $j = 1, 2, 3$, denote the coordinate and momentum operator of the j-th oscillator and the coupling to the substrate k_0 is associated with the onsite frequency $\omega_0 = \sqrt{k_0/m}$. The harmonic coupling constant between the $m_1 - m_2$ link and the $m_2 - m_3$ link is k and between the $m_1 - m_3$ link is k_3. p and q store the coordinate and momentum information of all the oscillators in a column vector form and

$$\mathbf{Q} = \omega_0^2 \mathbb{1}_3 + \omega_c^2 \begin{pmatrix} 1+\frac{k_3}{k} & -1 & -\frac{k_3}{k} \\ -1 & 2 & -1 \\ -\frac{k_3}{k} & -1 & 1+\frac{k_3}{k} \end{pmatrix}, \tag{4.1}$$

with $\omega_c = \sqrt{k/m}$.

To study its thermal transport, the system of quantum oscillators is connected

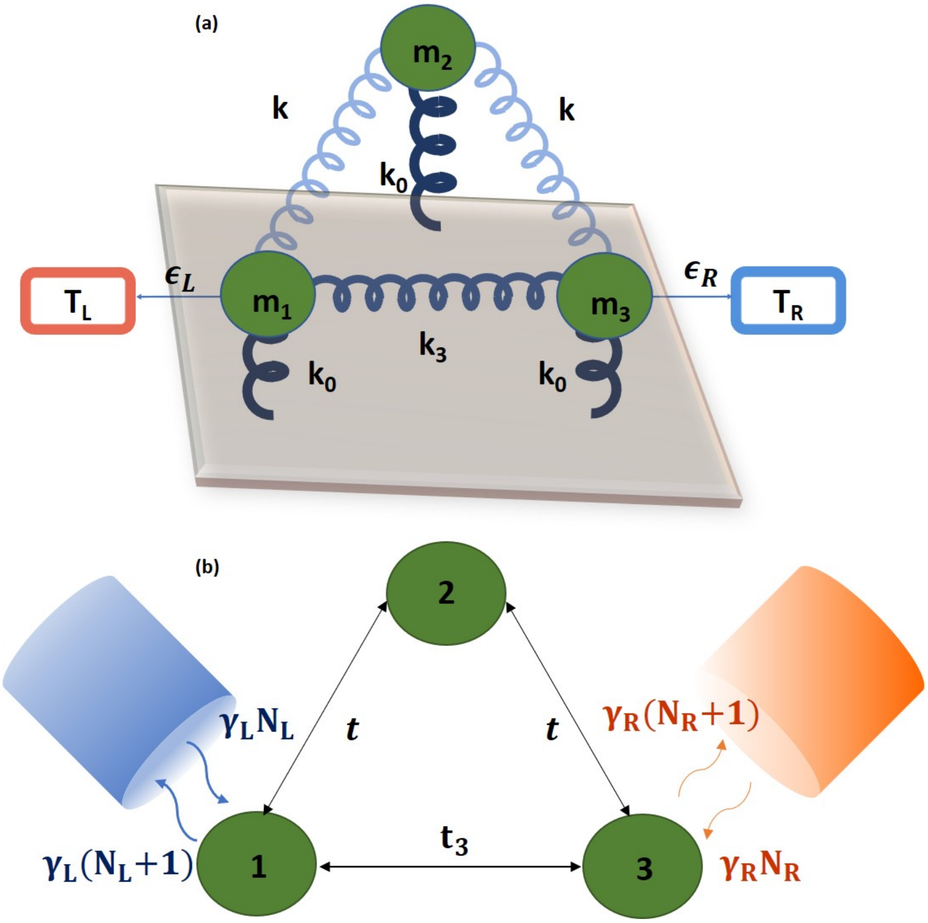

Figure 4.1: Schematic illustrations of the systems for studying geometry-based circulation in quantum thermal transport. (a) Two of the quantum oscillators $j = 1, 2$ are coupled to reservoirs with temperatures T_L and T_R, respectively. The quantum oscillator of mass m_2 is harmonically coupled to both m_1 and m_3 with coupling constant k while m_1 and m_3 are harmonically coupled to each other with coupling constant k_3. All masses couple to the substrate with harmonic coupling constant k_0. (b) The Bose-Hubbard model modeling the energy quanta as bosons with tunneling coefficients t along the upper path and t_3 along the lower path. The system is connected via the system-reservoir couplings γ_L and γ_R to two reservoirs with different temperatures T_L and T_R which determines the phonon number density N_L and N_R for the left and right reservoir respectively.

to thermal reservoirs maintained at temperatures $T_{L,R}$, respectively. Without loss of generality, we assume $T_L > T_R$. We evaluate the time evolution of the reduced density matrix of this system under the influence of the reservoirs through the RQME [65]:

$$\frac{d\rho(\mathcal{T})}{d\mathcal{T}} = \iota[\rho, \mathscr{H}] + \mathscr{D}\rho. \tag{4.2}$$

Here $\mathscr{D}$ is the Redfield dissipator defined as:

$$\mathscr{D}_{L,R}\rho = \int_0^\infty d\tau \Gamma_{L,R}(\tau)[X_{L,R}(-\tau)\rho, X_{L,R}] + h.c. \tag{4.3}$$

$[A, B]$ represents the commutator of operators A and B. For this system, the coupling operators are [65] $X_{L,R} = \sqrt{\epsilon_{L,R}} q_{1,3}$, with L, R denoting the left and right reservoir respectively. Here ϵ_L and ϵ_R are the system-reservoir coupling constants which essentially represent the strength of the system-reservoir coupling. Ref. [65] presents a general form of the spectral function of the thermal reservoir. In this chapter, we focus on the reservoirs with an ohmic spectral function, which is the Fourier transform of $\Gamma_{L,R}(\tau)$:

$$\Gamma_{L,R}(\omega) = \frac{sign(\omega)|\omega|}{\exp(\omega/T_{L,R}) - 1} \tag{4.4}$$

As this open quantum system comprises of a system of interest with a quadratic Hamiltonian of the form of Eq. (4.1) coupled to ohmic reservoirs through linear coupling operators [65], we can use the third quantization formalism introduced in sec. 2.2.2 to extract the non-equilibrium steady state (NESS) coordinate-momentum correlations. The implementation of third quantization formalism to calculate the NESS correlations for this system is outlined in appendix A.3.

Using the continuity equation, the thermal current from the i^{th} oscillator to the adjacent j^{th} oscillator can be derived [32, 61]. We follow the notation of Ref. [65] and use the following simplified definition of the local thermal current from the i^{th} to j^{th} oscillator:

$$\langle J_{ij} \rangle = \frac{K}{m} tr(p_j q_i \rho_{NESS}), \tag{4.5}$$

where K denotes the harmonic coupling constant between the two sites. For a harmonic system in the NESS, $\langle J_{12} \rangle = \langle J_{23} \rangle$, as there should not be any energy accumulation in oscillator 2. The total steady-state thermal current through the system is given by the steady-state value of

$$\langle J_T \rangle = \langle J_{13} \rangle + \langle J_{12} \rangle. \tag{4.6}$$

4.1.2 Bose-Hubbard model with LQME

In the second quantization representation, a quantum oscillator can be expressed in terms of creation and annihilation operators [48]. Under the rotating wave approximation one can neglect number non-conserving terms ($c_i^\dagger c_j^\dagger$, $c_i c_j$) such that the Hamiltonian of a system of harmonically coupled quantum oscillators can expressed in the form of the non-interacting Bose-Hubbard model [83, 84]. The rotating wave approximation is usually justified when the onsite frequency is stronger than tunneling coefficients.

In this section, we investigate local thermal transport of a Bose-Hubbard model in a multi-path geometry illustrated in Fig. 4.1 (b). In general, a three site Bose-Hubbard Hamiltonian can be written as:

$$\begin{aligned}\mathscr{H}_{BH} = &\sum_{j=1}^{3} \Omega_0 c_j^\dagger c_j - t(c_1^\dagger c_2 + c_2^\dagger c_1 + c_2^\dagger c_3 + c_3^\dagger c_2) \\ &- t_3(c_1^\dagger c_3 + c_3^\dagger c_1) + \frac{U}{2}\sum_{j=1}^{3} n_j(n_j - 1).\end{aligned} \tag{4.7}$$

Here a uniform onsite potential Ω_0 possibly from the system-substrate coupling has been included, $c_j^\dagger$ and c_j are the creation and annihilation operators at the j^{th} site. t is the tunneling coefficients between site 1-site 2 and site 2-site 3, and t_3 is the tunneling coefficient between site 1-site 3. U denotes the onsite interaction strength and n_j is the number density operator on the j^{th} site.

One can make the rotating wave approximation on Eq. (4.1) and approximate Eq. (4.1), the Hamiltonian of the system of coupled oscillators, through Eq. (4.7) with $U = 0$. To be able to make the rotating wave approximation, we work within a regime where $\Omega_0 >> t, t_3$. We reiterate that the aim of this chapter is to show that geometry-based circulations transcends formalisms and are universally found in multi-path quantum systems and not to justify a rigorous correspondence between different models and formalisms. We begin our investigation with the non-interacting Bose-Hubbard Hamiltonian $U = 0$ and address the interacting case later.

Similar to how we used the Langevin equation and RQME for multi-path classical and quantum system of oscillators respectively, for the open Bose-Hubbard system shown in Fig. 4.1 (b) we utilize the LQME [51] which describes the evolution of the reduced density matrix of this system of interest under the influence of the reservoirs. The LQME we work with has the form:

$$\begin{aligned}\partial\rho(\mathcal{T})/\partial\mathcal{T} &= \imath[\rho, \mathscr{H}_{BH}] + \gamma_L N_L(c_1^\dagger \rho c_1 - \frac{1}{2}\{c_1 c_1^\dagger, \rho\}) + \\ & \gamma_L(N_L+1)(c_1\rho c_1^\dagger - \frac{1}{2}\{c_1^\dagger c_1, \rho\}) + \gamma_R N_R(c_3^\dagger \rho c_3 - \frac{1}{2}\{c_3 c_3^\dagger, \rho\}) + \\ & \gamma_R(N_R+1)(c_3\rho c_3^\dagger - \frac{1}{2}\{c_3^\dagger c_3, \rho\}). \end{aligned} \tag{4.8}$$

Here $\mathcal{T}$, is the time, $\{A, B\}$ represents the anti-commutator of operators A and B. γ_L and γ_R represent the strength of the system-reservoir coupling to the left and right reservoir respectively. The reservoirs are assumed to maintain fixed excitation numbers N_L and N_R, respectively with $N_{L,R} = 1/[\exp(\Omega_0/T_{L,R}) - 1]$. The reservoirs emits an excitation at the rate $\gamma_j N_j$ into the system and absorbs excitation from the system at the rate $\gamma_j(N_j + 1)$ with $j = L, R$, as shown in Eq. (4.8). These exchange rates of excitation follow the assumption of Bose statistics and leads to the system being in equilibrium when coupled to a single reservoir.

Recently there have been concerns about the thermodynamic consistency of the local (position basis) LQME that we employ here [39, 85–87]. However, these issues can be addressed by choosing the thermodynamically correct definition of current related to work and heat [88, 89]. When it comes to thermal transport through a bosonic system described by the Bose-Hubbard model, there are multiple ways to define and calculate the thermal current in quantum systems [61, 83, 89].

Ref. [83] shows two different expressions for the thermal current of a linear chain. The first one utilizes the fact that in the steady state the time derivative of the expectation value of the system Hamiltonian should be zero, $Tr(\mathscr{H}\frac{\partial\rho}{\partial\mathcal{T}}) = 0$. The authors use Eq. (4.8) for the time derivative of the reduced density matrix. As it turns outs, the commutator in Eq. (4.8) does not contribute, while the contributions from the two reservoirs should sum up to zero in the steady state, making them equal and opposite to each other. Hence without loss of generality, either of the contribution from the left or right reservoir may be picked as the expression for thermal current. This expression for the thermal current accounts for not only heat current but also the current related to work [89–91]. As explained in Ref. [89], only the diagonal terms of the Hamiltonian contribute to the heat related current as those diagonal terms are the ones that are responsible for entropy production. The non-diagonal terms of the Hamiltonian contribute to the work done at the system-reservoir interface. As our focus is on the heat transferred through the system, we choose the second expression [61,83] and derive a formula of the thermal current associated with only heat. For a linear chain described by the Bose-Hubbard Hamiltonian, the local thermal current operator associated with heat through a link between the i^{th} and $(i+1)^{th}$ sites can be evaluated by the Heisenberg equation of motion. Explicitly, one defines the Hamiltonian of the partial chain up to the link as H_L. Then, $J_{i,i+1} = dH_L/dt = i[H_L, H]$, where H_L contains the Hamiltonian from the left end to the left site of the link. By generalizing the definition, the thermal current operator from site i to site j is given by

$$J_{ij} = -\imath t_{ij}(\Omega_0 - U)(c_i^\dagger c_j - c_j^\dagger c_i) - \imath U t_{ij}(c_i^\dagger c_j c_j^\dagger c_j - c_j^\dagger c_j c_j^\dagger c_i). \tag{4.9}$$

Here t_{ij} takes the value t or t_3 for J_{12} or J_{13}, respectively. The expectation value of the local current is obtained from $\langle J_{ij} \rangle = tr(\rho J_{ij})$. By using Eq. (4.9) as the definition of current we make sure that the total thermal current does not violate the second law of thermodynamics as it always flows from hot to cold.

For the noninteracting case with $U = 0$, we implement the third quantization method for the LQME [63, 64] and follow the steps in appendix A.4 to obtain the non-equilibrium steady-state correlations. The third quantization formalism is limited to non-interacting Hamiltonians and cannot be used for a system with interactions. To study the Bose-Hubbard system with a non-zero interaction strength, we numerically integrate the LMQE (4.8) and get the evolution of the reduced density matrix. The numerical integration is done through the fourth-order Runge-Kutta method. Theoretically, the density matrix of a bosonic system can be infinite dimensional as each site can accommodate an infinite number of bosons due to their Bose-Einstein statistics. However, due to limited resources, numerical simulations of bosonic systems are usually performed by restricting the maximal number of bosons per site. This restriction leads to a truncated basis. We follow the algorithm outlined in Ref. [62] to construct this truncated basis for our multi-path system. In our simulations, we restrict the number of bosons per site to three. to find the steady state thermal currents. Once the integration of the LQME is carried out, one can calculate the expectation values of the local currents by taking their trace with the reduced density operator. The steady state local thermal currents for an interacting system should obey $\sum_i \langle J_{i2} + J_{2i} \rangle = 0$, such that there is no energy accumulation on site 2.

4.2 Results and discussion

4.2.1 Quantum harmonic oscillators with RQME

In this section we present the results of the quantum thermal transport for the harmonically coupled quantum oscillators coupled to ohmic reservoirs shown in Fig. 4.1 (a). Before showing the results of the setup shown in Fig. 4.1, we ensure that our results for a linear chain of quantum oscillators are consistent with those presented in Ref. [65]. We work in the small temperature regime i.e. when $T_L - T_R = \Delta T << T_{avg}$, where $T_{avg} = (T_L + T_R)/2$ is the average temperature of the reservoirs. We assume symmetric coupling to the reservoirs with $\epsilon_{L,R} = \epsilon$. The parameter space of this coupled quantum oscillator system in a triangular geometry consists of internal parameters k/k_3 and external parameters T_L/ω_0, T_R/ω_0, and ϵ/ω_0.

We show the behavior of the thermal conductance $\langle J_T \rangle / \Delta T$ as a function of T_{avg} for different values of the system-reservoir coupling ϵ in Fig. 4.2 with $k = k_3 = m\omega_0^2$. We note that when the coupling constants and masses of the three oscillators are equal, the currents on each of the links are also equal. The quantum of thermal

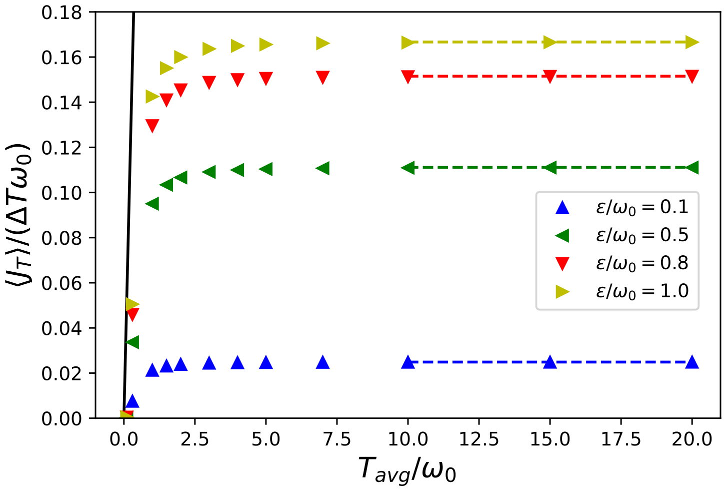

Figure 4.2: Quantum thermal conductance from the total current through the three-site harmonic oscillators with $k = k_3 = m\omega_0^2$ as a function of T_{avg}/ω_0 for different values of the system-reservoir coupling and fixed $\Delta T/T_{avg} = 0.02$. The black line shows the quantum of thermal conductance and the colored dashed lines show the corresponding values of the classical thermal conductance.

conductance [32] $= \pi {k_B}^2 T_{avg}/6\hbar$ is shown by the black curve of Fig. 4.2. In the low temperature regime when $\omega_0 > T_{avg}$, the conductance increases monotonically as T_{avg} increases. As one can see, the quantum of thermal conductance becomes an upper bound for the numerical values as $T_{avg} \to 0$. As T_{avg} increases, the thermal conductance starts to saturate and becomes constant. At high temperatures, the conductance of the system shown in Fig. 4.1 (a) can be explained classically. The classical thermal transport in multi-path systems such as Fig. 3.1 with Langevin reservoirs has been shown in chapter 3 the RQME results approach the corresponding classical values [77] in the high-temperature limit. In Ref. [65], the authors show that the classical Langevin results agree with the RQME in the high temperature limit $\omega_0 \ll T_{avg}$ for a linear chain of quantum harmonic oscillators, and here we confirm this agreement for a multi-path geometry.

Since the RQME is essentially a second-order perturbation formalism [65], it can be used reliably when the system-reservoir coupling is weak. Within the weak coupling regime, we found the thermal conductance increases with ϵ/ω_0, as shown in Fig. 4.2.

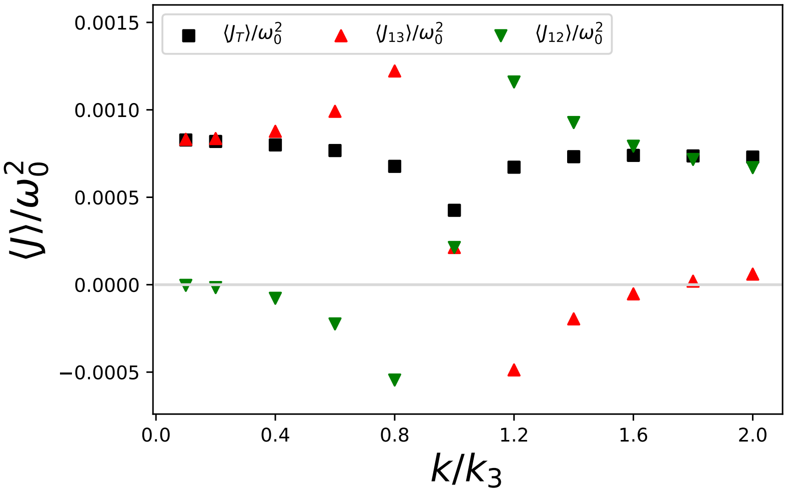

Figure 4.3: Total and local steady-state thermal currents of the three site coupled quantum oscillators described by the RQME as a function of k/k_3 for $\epsilon/\omega_0 = 0.1$. Here $T_L/\omega_0 = 1.01$ and $T_R/\omega_0 = 0.99$. ω_0 is the onsite frequency of the quantum oscillators. The solid grey line marks the zero of the y-axis.

It has been shown [81] that the thermal conductance of a classical harmonic chain changes non-monotonically as the system-reservoir coupling strength is varied over several orders of magnitude. However, due to the weak system reservoir coupling assumption that is needed to write the RQME we cannot explore the behavior of the quantum thermal transport in the regime where $\epsilon/\omega_0 \gg 1$.

The total quantum thermal current and its thermal conductance do not show any unexpected behavior. However, when we examine the local steady state current on each of the links we unambiguously demonstrate the existence of atypical local thermal current in the coupled quantum system. For the quantum system shown in Fig. 4.1 with $k_3 = m\omega_0^2$, and $\epsilon/\omega_0 = 0.1$ coupled to reservoirs with $T_L/\omega_0 = 1.01$, $T_R/\omega_0 = 0.99$, the total and local steady state thermal currents are shown in Fig. 4.3. As one can see, when $k < k_3$ the local thermal current along the $1-3$ link flows from hot to cold according to the direction of the reservoirs, but the local thermal current along the $1-2$ link flows in the opposite direction or from cold to hot as indicated by its negative value. We term this local floe from cold to hot as an atypical local current. In the steady state, we have verified that $\langle J_{12}\rangle = \langle J_{23}\rangle$. The combination of an atypical $\langle J_{12}\rangle$ with a normal $\langle J_{13}\rangle$ gives rise to a counterclockwise (CCW) internal circulation. At $k = k_3$, the local thermal currents on all the links are the same and flow in the normal direction, i.e. from hot to cold. When all local thermal currents flow in the same direction no circulations can arise, we call the flow unidirectional (UD). For $k > k_3$, the local thermal currents on the $1-2$ and $2-3$ links flow from hot to cold, but the local thermal current on the $1-3$ link shows atypical behavior as it flows from cold to hot, indicated by its negative value. In this case, the local thermal currents give rise to an internal clockwise (CW) circulation. For $k >> k_3$, the local thermal currents become unidirectional again. The three patterns (CCW, UD, and CW) are illustrated in the top panel of Fig. 4.4. The positive value of the total steady state thermal current throughout the the parameter regime explored in Fig. 4.4 confirms that although a local thermal current may show atypical behavior by flowing from cold to hot, the total steady state thermal current is always from hot to cold, consistent with the second law of thermodynamics.

Fig. 4.4 shows the phase diagram for the three patterns as a function of the parameters k/k_3 and ϵ/ω_0. When ϵ/ω_0 is small, both types of circulations are observable. The circulation has the property that the atypical local current is along the link with the smaller value of the harmonic coupling constant. For example, $k/k_3 > 1$ implies the atypical current is along the link with k_3, which is the $1-3$ link, giving rise to CW circulation. However, as ϵ/ω_0 is increased, the regimes of both circulations shrink. Beyond a certain critical value of ϵ/ω_0, only the UD flow survives.

4.2.2 Bose-Hubbard model with LQME

In this section we present the local steady-state thermal currents of the open quantum system of coupled oscillators modeled through the LQME. Eq. (4.8) where the system of interest shown in Fig. 4.1 (b) is modelled through the Bose-Hubbard Hamiltonian. We begin with the non-interacting Bose-Hubbard model for which $U = 0$ in Eq. (4.7). We take $t_3/\Omega_0 = 0.1$, and vary t/Ω_0 from 0.01 to 0.2 such that we are in the regime where the rotating wave approximation is valid. The system is coupled to the thermal reservoirs symmetrically which are maintained at $T_L/\Omega_0 = 1.01$ and $T_R/\Omega_0 = 0.99$

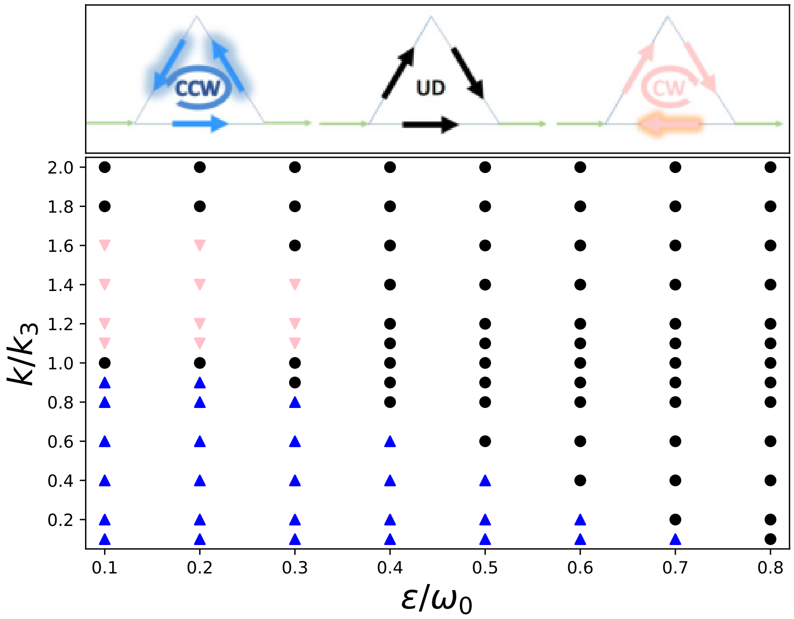

Figure 4.4: The top panel illustrates the patterns of local thermal currents. From left to right: counterclockwise (CCW), unidirectional (UD) and clockwise (CW). The lower panel shows where each pattern is found as a function of k/k_3 and ϵ/ω_0 for the three coupled quantum harmonic oscillators under the influence of ohmic reservoirs. Here $T_L/\omega_0 = 1.01$ and $T_R/\omega_0 = 0.99$, and the masses are the same with $\sqrt{k_3/m} = \omega_0$. In the phase diagram, the blue triangles, black circles, and pink inverted triangles represent the CCW circulation, unidirectional flow, and CW circulation, respectively.

through out our discussion. We employ the third quantization formalism outlined in appendix A.4 to solve for the steady state correlations of this system.

In Fig. 4.5 we show the total and local currents for $\gamma/\Omega_0 = 0.1$ as a function of t/t_3. As we tune t/t_3, we see that the local currents follow the trend of three patterns observed in the previous section. For $t/t_3 < 1$, the local currents combine to give rise to an internal CCW circulation. For $t/t_3 > 1$, the local currents show a CW internal circulation. While at $t/t_3 = 1$, both the local currents flow unidirectionally. At all these parameter points, the total steady state thermal current is positive and is accompanied by a dip at the point where there is a change in circulation pattern. Next, we examine the three patterns as a function of t/t_3 and γ/Ω_0 which is shown in Fig. 4.6. From the phase diagram, we infer that both CCW and CW circulations

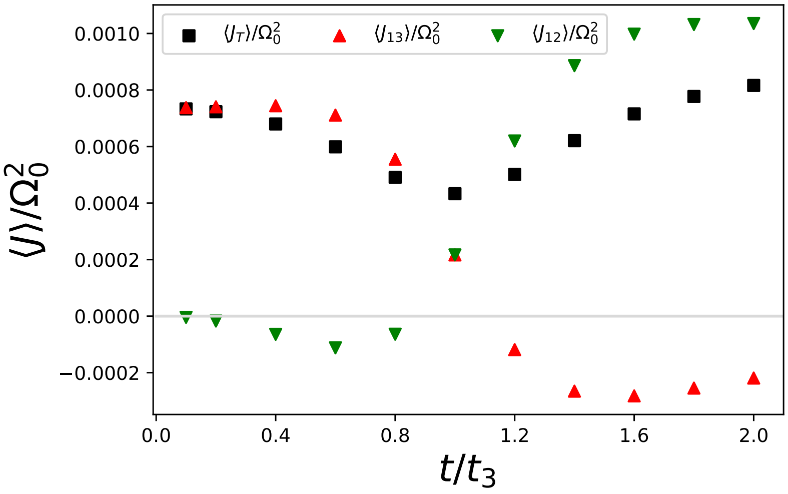

Figure 4.5: The total and local steady-state thermal currents of the non-interacting Bose-Hubbard model described by the LQME as a function of t/t_3 for $t_3/\Omega_0 = 0.1$ and $\gamma/\Omega_0 = 0.1$ with $T_L/\Omega_0 = 1.01, T_R/\Omega_0 = 0.99$. Ω_0 is the onsite frequency. The solid grey line marks the zero of the y-axis.

dominate at small γ/Ω_0. As γ/Ω_0 is increased both regions of circulations decrease quite similar to our RQME results shown in sec. 4.2 A. We note that increasing γ/Ω_0 depletes the CCW circulation regime more in comparison to the CW circulation regime.

We conclude this section by showing the robust nature of these circulations against interactions. Here, U/Ω_0 may be used to model underlying interactions with a substrate and anharmonicity or disorder in the system. To be in the weakly interacting regime, U/Ω_0 should be the smallest energy scale in the system and hence should satisfy $U < (t, t_3)$. In the presence of interactions, in addition to the usual two operator correlations the thermal steady state current also depends on four operator correlations as seen in Eq. (4.9). We also note that the four operator correlators in Eq. (4.9) depend on the number density of the oscillator into which the heat is flowing. In Fig. 4.7 (a) and (b) we show the total and local steady-state thermal currents for the Bose Hubbard model with interaction strength of $U/\Omega = 0.01, 0.05$ respectively. To make sure we are within the weakly interacting regime we use standardized tunneling, where the tunneling coefficients on the upper and lower path

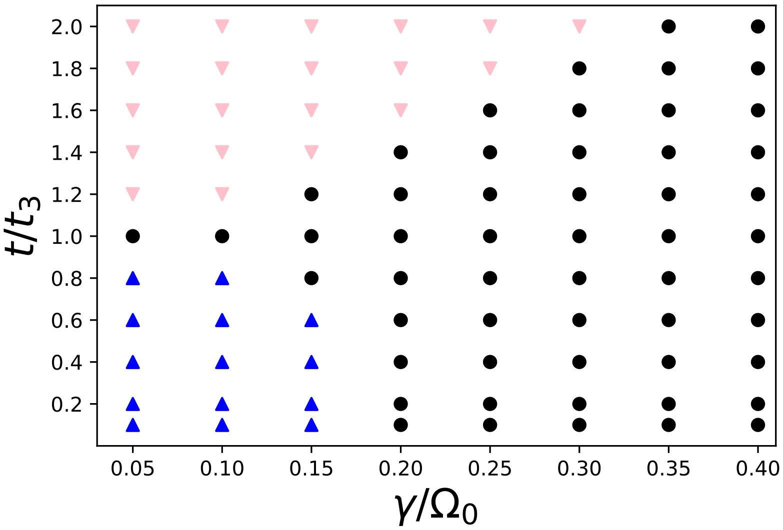

Figure 4.6: Phase diagram of the noninteracting Bose Hubbard described by the LQME, showing the CCW circulation (blue triangles), CW circulation (pink inverted triangles), and UD flow (black dots) on the plane of t/t_3 and γ/Ω_0. Here, $T_L/\Omega_0 = 1.01, T_R/\Omega_0 = 0.99$, $t_3/\Omega_0 = 0.1$.

satisfy $min\{(t, t_3)/\Omega_0\} = 0.1$ such that $(t, t_3) > U$ is always true. We make sure that the net current through the site into which the current is flowing is zero and the signs of the local currents $\langle J_{12}\rangle/{\Omega_0}^2, \langle J_{23}\rangle/{\Omega_0}^2$ agree. We infer from Fig. 4.7 that even in the presence of interactions, the local steady state thermal currents combine to give rise to both the circulation patterns.

4.3 Summary

In this chapter we demonstrated that a minimal system of three quantum oscillators in conjunction with reservoirs show an internal circulations of the steady state thermal currents. We show that these circulations are universal in the sense that they can be found through both the Redfield and Lindblad form of the quantum master equations wherein a different Hamiltonian is used to describe the system. The local currents and flow patterns obtained show the same qualitative nature. We map the two patterns of internal circulation of steady-state local thermal currents, CCW and CW as a

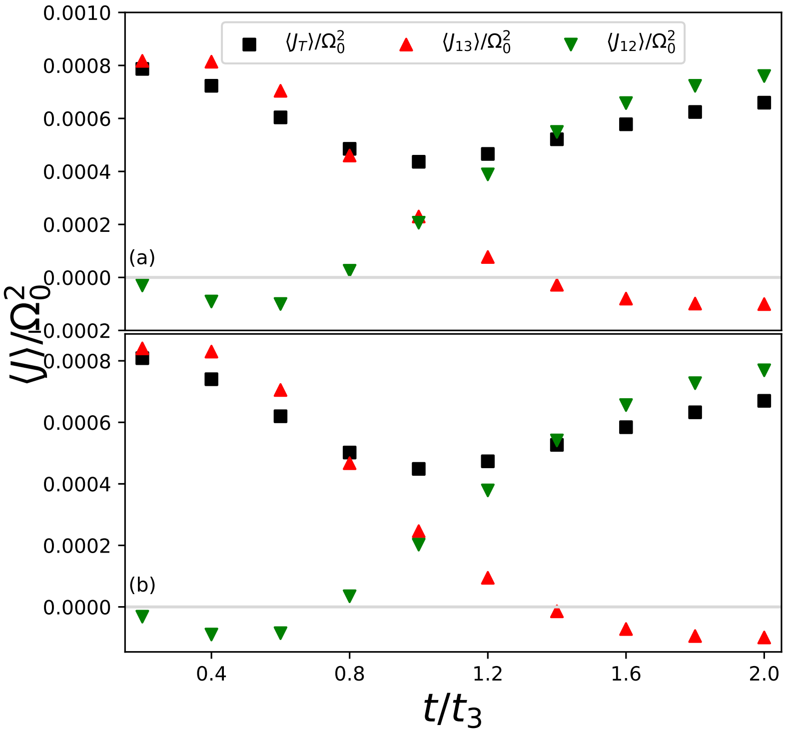

Figure 4.7: The total and local steady-state thermal currents of the Bose Hubbard model with self-interactions described by the LQME for (a)$U/\Omega_0 = 0.01$ and (b) $U/\Omega_0 = 0.05$ as a function of t/t_3 with standardized tunneling coefficients satisfying $min\{(t, t_3)/\Omega_0\} = 0.1$. Here $T_L/\Omega_0 = 1.01, T_R/\Omega_0 = 0.99$, $\gamma/\Omega_0 = 0.1$, and the solid grey line marks the zero of the y-axis.

function of internal parameters such as k/k_3 or t/t_3 and external parameters such as ϵ/ω_0 or γ/Ω_0. The Redfield calculations show a re-entrant regime between the unidirectional flow while no such such behavior is show in the Lindblad calculations, highlighting their different quantitative nature. Finally, through numerical simulation of the LQME, we show that the circulation patterns are robust against interactions.

Chapter 5

Quantum transport of Photons

The work presented in this chapter has been previously published in **Physical Review A** 102 (2020): 023704 as:
"Geometry-based circulation of local photonic transport in a triangular metastructure."
Authors: Palak Dugar, Michael Scheibner and Chih-Chun Chien.

Having dealt with classical and quantum thermal transport in a multi-path geometry in the previous chapters where we unambiguously proved the presence of an atypical local steady-state thermal current, in this chapter we show that this 'atypical behavior' associated with local thermal current can also be found for photonic particle transport in a multi-path geometry. Ref. [25] shows how the multi-path geometry of a triangle can be utilized to show internal circulation of the steady-state electronic current. The typical route to achieve circulation of photons is through artificial gauge fields. In this chapter we demonstrate steady-state photonic transport in a multi-path geometry can show circulation patterns without using an artificial gauge field. We examine the parameter regimes where atypical behavior can arise and lead to an internal circulation of the steady-state photonic current.

For the system of interest, we consider a triple quantum dot system with each of the three quantum dots embedded in separate photonic arrays, coupled to each other such that they form a triangle. In this chapter, we will refer to the entire system of the three quantum dots, photonic crystals, arrays and waveguide as the triple quantum dot metastructure, or TQDM for short. To study photonic transport, this TQDM is coupled to appropriate particle reservoirs which act as photonic pump and sink generating the photonic current within the system.

Now theoretically, the Bose-Einstein statistics of photons allows an arbitrary large numbers of photons on any given site. However due to limited resources such as memory and time, numerical simulation of a system with a large density matrix is not feasible [63, 92]. The TQDM considered here provides a constraint on the photons that can participate in transport. The main function of the quantum dots in the TQDM is to provide excitons for coupling to the incoming and outgoing photons. Due to the coupling between the photons and the excitons in the quantum dots, the spectrum of the coupled photons may differ from that of the uncoupled cavity photons. With carefully designed waveguides, only the photons coupled to the excitons can be transmitted [93, 94]. Given the limited number of excitons with a specific energy on each quantum dot, the number of photons on each site that can participate in transport is limited making a realistic numerical simulation of the photonic transport possible.

In sec. 5.1 we describe the model for the TQDM and the LQME used to study the steady state photonic transport. In our results section, we present our numerical results for the noninteracting system where we explicitly show the emergence of circulation patterns. Next, in 5.2.2 we present the phase maps of the flow patterns in the TQDM as a function of system parameters and the system-reservoir coupling in the weakly and strongly interacting regimes. We talk about decoupling of number densities at the sites and the local currents in sec. 5.2.3. We end our results section by presenting a phase map obtained through the third quantization formalism for the noninteracting TQDM without any photon blockade in sec. 5.2.4 and summarize the chapter in 5.3.

5.1 Model and method

Illustrated in Fig. 5.1, the TQDM that we envision has a triangular geometry where the photonic cavites, each embedded with quantum dots are placed at the vertices. Photonic waveguides are placed between the cavities for transferring photons. The photonic crystal structure forms the “photonic connections” as the photons can evanescently couple from one cavity to the waveguides [95, 96], resulting in photonic transport across the cavities. The system is connected via additional waveguides to two photon reservoirs which play the role of an incoherent photon pump and sink to sustain photonic transport across the TQDM.

A complete description of the photon-exciton interactions at the quantum dots and its transport across the waveguides requires the microscopic system Hamiltonian to include interactions between electrons, holes and photons. Here we take a phenomenological point of view and consider an effective model of the photons by integrating out the electron-hole contributions, such that the transport of photons can be treated as a simple tunneling process. We choose the Bose-Hubbard Hamiltonian to model the photons in the TQDM which describes the tunneling of the photons and also has repulsive onsite interaction between the photons present due to the repulsive coulombic interaction between the underlying electrons in the quantum dots. The effective Bose-Hubbard Hamiltonian for the TQDM has the same form as the one used to study circulations in steady state thermal currents in chapter 4. For the sake of completion we repeat it here:

$$\mathscr{H} = -t_1(c_1^\dagger c_2 + c_2^\dagger c_1 + c_2^\dagger c_3 + c_3^\dagger c_2) - t_3(c_1^\dagger c_3 + c_3^\dagger c_1) + \frac{U}{2}\sum_{i=1}^{3} n_i(n_i - 1). \tag{5.1}$$

Here t_1 is the tunnelling coefficient between the first and second site, as well as the tunnelling coefficient between the second and third site t_1. t_3 is the tunneling coefficient between the first and third site. U is the strength of the effective onsite interaction which we assume to be repulsive $U \geq 0$. The photonic number operator at the i^{th} site is $n_i = c_i^\dagger c_i$. We take $\hbar = 1$ and the time unit is defined as $T_0 = \frac{\hbar}{t_1}$.

In the open quantum system approach, physical observables, such as the density or current, can be obtained from taking the expectation of the corresponding operators once the time evolution of the reduced density matrix of the TQDM photons participating in the transport, $\rho(T)$, is known. We use the Lindblad form of the quantum master equation introduced in sec. 2.2.

$$\begin{aligned}\frac{\partial\rho(T)}{\partial T} &= \frac{\iota}{\hbar}[\rho, \mathscr{H}] \\ &+\gamma_L N_L(c_1^\dagger \rho c_1 - \frac{1}{2}\{c_1 c_1^\dagger, \rho\}) + \gamma_L(N_L+1)(c_1\rho c_1^\dagger - \frac{1}{2}\{c_1^\dagger c_1, \rho\}) \\ &+\gamma_R N_R(c_3^\dagger \rho c_3 - \frac{1}{2}\{c_3 c_3^\dagger, \rho\}) + \gamma_R(N_R+1)(c_3\rho c_3^\dagger - \frac{1}{2}\{c_3^\dagger c_3, \rho\}). \quad (5.2)\end{aligned}$$

The same form of LQME (4.8) with the Bose-Hubbard Hamiltonian (4.7) was used to describe the quantum thermal transport in a multi-path geometry in chapter 4. Here, $\mathscr{H}$ is the TQDM Hamiltonian and N_L and N_R are the fixed photon numbers of the left and right reservoirs respectively. The above exchange rates of photons are consistent with the quantum optical master equation [49, 51].

The Lindblad equation (5.2) describes a homogeneous Markov process. According to Ref. [97], there exists at least one steady-state solution in a finite-dimensional space. Ref. [97] shows that when ρ is rewritten as an equivalent column vector, the Lindblad superoperator $\mathscr{L}$ can be written as a square matrix. However, $\mathscr{L}$ may

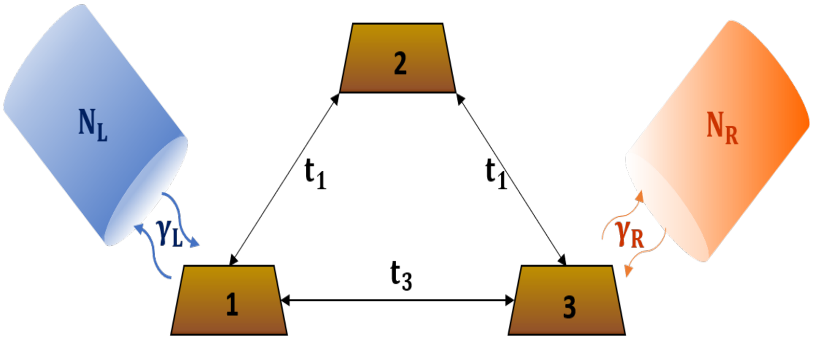

Figure 5.1: The open TQDM to study photonic transport has the same skeletal form as that of Fig. 4.1 (b). The three quantum dots are embedded in the three photonic cavities labeled by 1, 2, and 3. The cavities are connected by photonic waveguides. The quantum dots provide excitons for coupling to the photons, and only the photons coupled to the excitons are transported via the waveguides. The photonic transport is described by the effective hopping of the photons and effective repulsion from the underlying electrons. Site 1 (3) of the system is connected to a photon pump (sink) via additional waveguides for maintaining a steady-state.

not be a normal matrix ($\mathscr{L}\mathscr{L}^\dagger \neq \mathscr{L}^\dagger\mathscr{L}$) and hence may not be diagonalizable [98]. To overcome this technical difficulty, we implement the fourth-order Runge-Kutta method [99] to integrate Eq. (5.2) from a given initial state and obtain the steady-state density matrix after the transient behavior decays away. The expectation value $\langle A \rangle$ of an operator A can be obtained from $Tr(\rho A)$. Here Tr denotes the trace. After the steady-state density matrix ρ_{ss} is found from Eq. (5.2), the steady-state current and occupation nummbers can be obtained accordingly.

For a linear chain, the local photonic current operator through a link between the i^{th} and $(i+1)^{th}$ sites can be evaluated by using the continuity equation and Heisenberg's equation of motion, $J_{i,i+1} = dN_L/dt = i[N_L, H]$, where N_L contains the number density of the partial chain from the left end to the i^{th} site. By generalizing the definition, the photonic current operator from site i to site j is given by:

$$J_{ij} = -\iota(t_{ij}c_i^\dagger c_j - t_{ij}c_j^\dagger c_i), \tag{5.3}$$

where t_{ij} takes the value t_1 or t_3 for J_{12} or J_{13}, respectively. In the steady-state,

$\langle J_{12}\rangle = \langle J_{23}\rangle$, with the total steady-state photonic current through the TQDM:

$$\langle J_T\rangle = \langle J_{12}\rangle + \langle J_{13}\rangle. \tag{5.4}$$

Due to the limited availability of electron-hole pairs with a specific energy at a quantum dot, the coupling between the photons and the electron-hole pairs can be utilized to limit the number of photons that participate in transport. This phenomenon is generally known as the photon blockade [100–102] and we employ it here to introduce a truncated basis for the TQDM photons. The truncation parameter M denotes the maximum number of photons that a site can accommodate. These truncated basis states are constructed following the algorithm of Ref. [62]. In our simulations, the initial density matrix was set to the one with no photons in the system or to the maximal entropic state. Both types of initial states lead to the same steady-state density matrix. However, in the strongly interacting regime when γT_0 is very small, the convergence to the steady-state value can be slow, so we use the steady-state value of an adjacent point in the parameter space as the initial condition to achieve faster convergence. Importantly, we have checked that steady-state ρ obtained from the numerical integration of Eq. (5.2) indeed makes the right-hand side vanish within machine precision.

5.2 Results and discussion

5.2.1 Noninteracting photons with photon blockade

We study photonic transport through the TQDM illustrated in Fig. 5.1 in the incoherently pumped and dissipative regime with $\gamma_L = \gamma_R = \gamma \neq 0$ for fixed $N_L = 1$ and $N_R = 0$. The photon blockade due to the photon-exciton interaction restricts the maximum number of allowed photons on each site by M. We begin with the noninteracting Bose-Hubbard Hamiltonian, $U = 0$ with $M = 1$. In the upper panel of Fig. 5.2, we show the time evolution of the local currents J_{12} and J_{13} for two selected values of $t_3/t_1 = 0.6, 1.4$ for $\gamma T_0 = 0.5$. It is clear from the plateau in the long time limit that the local currents are in their steady-state. More importantly,

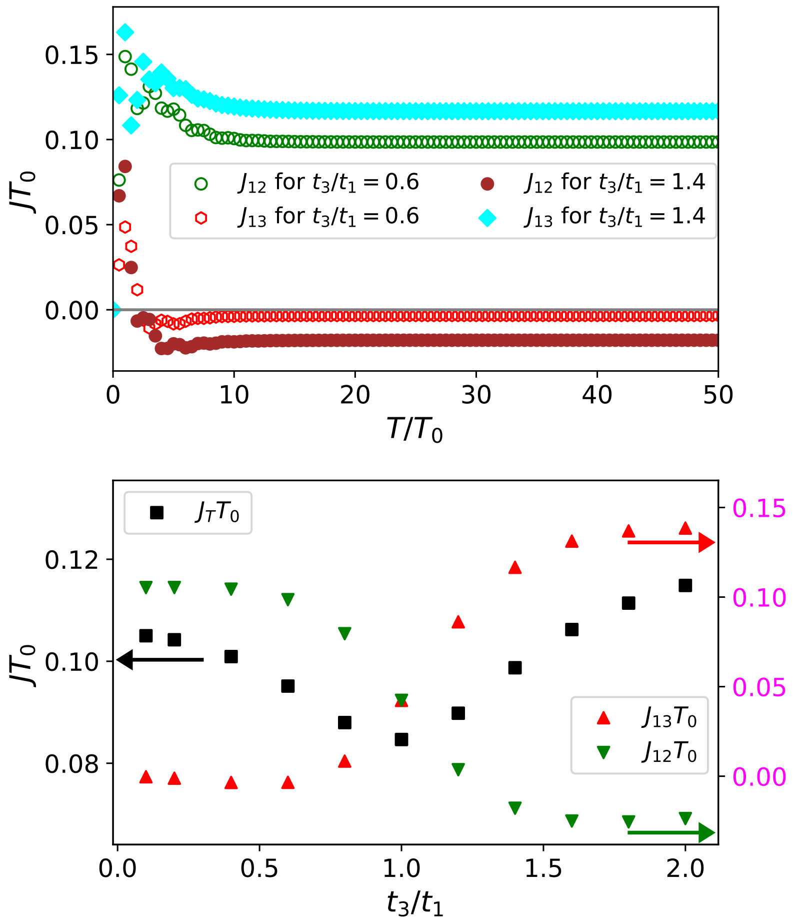

Figure 5.2: (Top panel) The local currents J_{12} and J_{13} as functions of time with $t_3/t_1 = 0.6, 1.4$, $\gamma T_0 = 0.5$, and $M = 1$ without the onsite interaction ($U = 0$). The plateaus of the currents are the signature of a steady-state. (Bottom panel) The steady-state values of the local currents J_{12}, J_{13} and the total current J_T as functions of t_3/t_1 with the same γT_0 and M, showing opposite signs of J_{12} and J_{13} in certain regimes.

one can see that J_{13} for $t_3/t_1 = 0.6$ and J_{12} for $t_3/t_1 = 1.4$ are negative and show an atypical behavior by flowing opposite to the normal flow from the reservoir with the higher to a lower photon number density.

Next keeping the system-reservoir coupling fixed, $\gamma T_0 = 0.5$ we investigate the steady-state local and total currents as a function of t_3/t_1, these currents are shown in the lower panel of Fig. 5.2. For small t_3/t_1, we get a normal flow for J_{12} while J_{13}

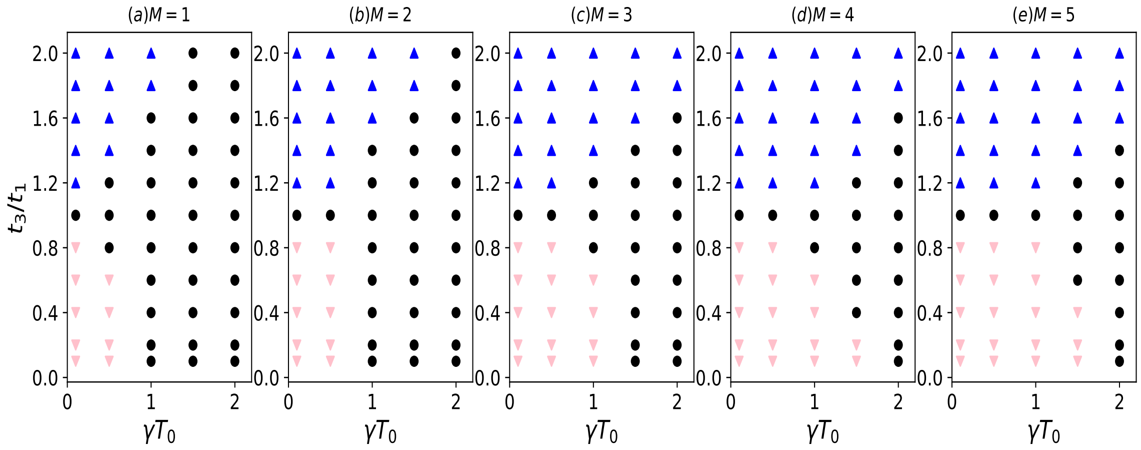

Figure 5.3: Phase diagrams showing the steady-state patterns of the photonic current with $U = 0$ and $M = 1, 2, 3, 4, 5$ (from left to right). Here the pink upside-down triangles denote the CW circulation, the black circles denote the UD flow, and the blue triangles denote the CCW circulation.

shows atypical behavior. Here, the combination of $J_{12} > 0$ and $J_{13} < 0$ corresponds to an internal clockwise (CW) circulation of the photons in the TQDM. For intermediate ratio, $0.8 \leq t_3/t_1 \leq 1.2$ both J_{12} and J_{13} exhibit normal behavior leading to a lack of circulation which we call unidirectional (UD) flow. Finally, for large t_3/t_1, we get get atypical behavior for J_{12} while J_{13} is normal. This combination of $J_{12} < 0$ and $J_{13} > 0$ corresponds to an internal counter-clockwise (CCW) circulation. This convention for labeling the orientation of the circulation is the same as used in chapter 4. It can be clearly inferred that varying the ratio t_3/t_1 can lead to tuning of the pattern of internal circulation of the photons in the steady-state. We emphasize that the internal circulation of photons is a steady-state phenomenon, not a transient one, because the long-time limit has been taken.

The mechanism behind the photonic circulations is a combination of the wave nature of quantum particles and multi-path geometry. As explained in Ref. [25], the wave functions spread out over the whole system in the triangular geometry during the dynamic process, making it possible for one path to overflow while another path transports the particles backward to compensate for it. This mechanism of overflow transcends classical-quantum boundary as well as spin-statistics. The Bose-Einstein statistics of photons allows us to explore the dependence of the circulation on M, which we will address shortly. Moreover, the geometry-induced circulation presented here is not associated with any real or artificial gauge field. Thus, there is no quantization condition on the vorticity of the photons.

When $M = 1$, the non-monotonic behavior of J_T on t_3/t_1 shown in Fig. 5.2 may be considered as an indication of a change of the orientation of the photon circulation in the metastructure. We notice that the $M = 1$ case of photons is similar to the spinless fermions studied in Ref. [25] because there cannot be two particles on the same site. However, a careful comparison shows that the similarity is only qualitative because of the different spin-statistics. Specifically, the evaluations of the commutator in Eq. (5.2) and the exchange terms with the reservoirs depend on whether the particles are bosonic or fermionic. Thus, it can be concluded that the spin-statistics cause quantitative differences between electronic and photonic transport under the constraint $M = 1$.

After establishing the existence of internal photon circulations in the TQDM, we explore whether these circulations can survive in the photon blockade regime with more photons per site. We consider $M = 2, 3, 4, 5$ and the TQDM exhibits both CW and CCW circulations for all cases with $M > 1$. Later on we will show the phase diagram without any photon blockade, $M \to \infty$, and confirm that the photonic transport already saturates for relatively small values of M. Fig. 5.3 shows the phase diagrams of the steady-state flow patterns as a function of M, t_3/t_1, and γ. By comparing the phase diagrams of noninteracting photons with $M = 1, 2, 3, 4, 5$, we infer that in the photon blockade regime with higher allowed number of photons per site, the internal circulations of photons not only survive survive but the regimes of both CW and CCW circulations increase as M increases. We conjecture that more photons are present in each site when M increases which increases the possible configurations of the photon wavefunctions, leading to overshoots of the flows along certain paths and causing the internal circulation.

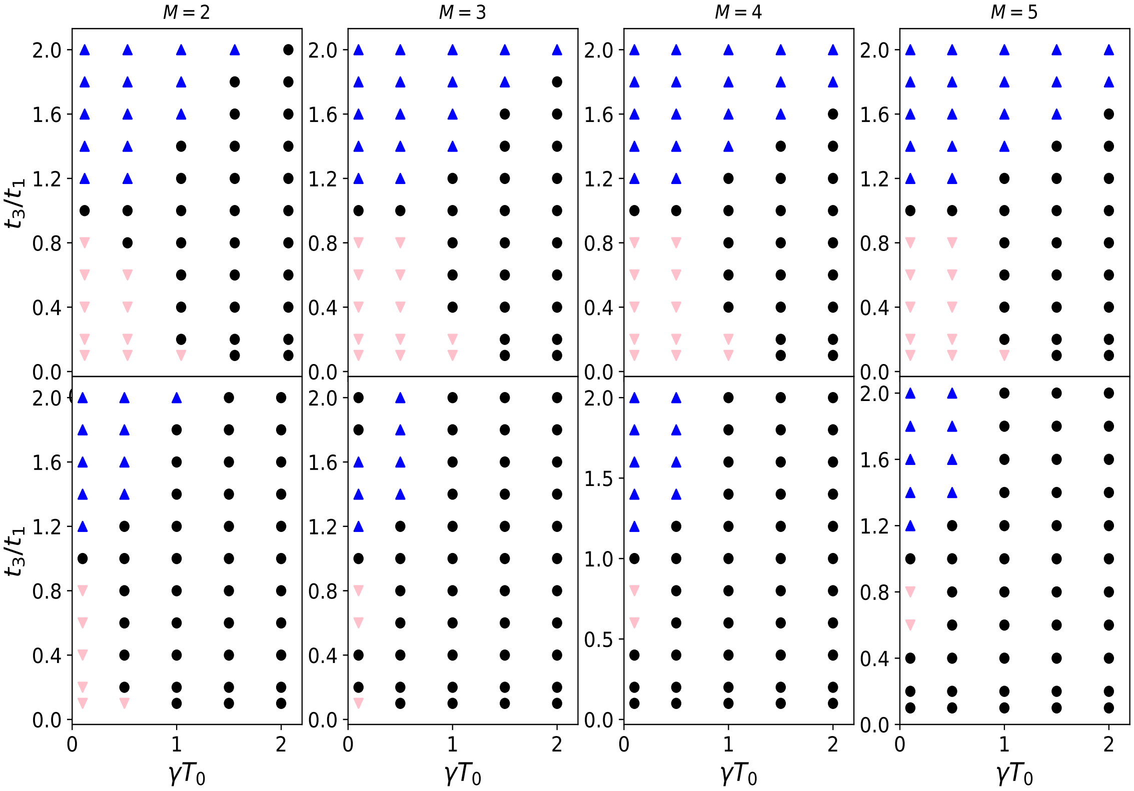

Figure 5.4: Phase diagrams showing the steady-state patterns of the photonic current for the cases with $U = t_1$ (the top row) and $U = 5t_1$ (the bottom row). Here $M = 2, 3, 4, 5$ from left to right. The pink upside-down triangles denote the CW circulation, the black circles denote the UD flow, and the blue triangles denote the CCW circulation.

5.2.2 Photons with effective onsite interactions and photon blockade

While photons in vacuum do not interact with each other [103], the photons in the TQDM interact with the excitons in the quantum dots and may experience an effective repulsion amongst themselves. To investigate photonic transport in a system with such effective repulsive interaction, we utilize the Bose-Hubbard Hamiltonian with a non-zero U and calculate the steady-state expectation values of the local currents from Eq. (5.2). Once the steady state local photonic currents are known, the phase diagrams of of flow patterns for interacting photons in the TQDM are constructed and shown in Fig. 5.4.

When U is smaller or comparable to the tunneling coefficient t_1, the phase maps of the circulation patterns shown in the upper row of Fig. 5.4 are qualitatively similar to the noninteracting maps shown in Fig. 5.3. The regimes showing CW and CCW circulations increase as M increase from 1 to 4, but beyond that the circulation regimes seem to saturate as M is increased further. Thus, we establish that the photon circulation is not unique to noninteracting systems.

As U is increased further, both the CW or CCW regimes of circulations are suppressed, as shown in the lower panel of Fig. 5.4. In Ref. [25] the authors reason that the suppression of internal electronic circulations in a triangular triple quantum dot system is due to the scattering of the electrons due to the onsite interactions. Extending that to the case of internal circulation of photons presented here, the photons may also suffer an effective scattering and may suppress the circulation as well.

The phase maps in the regime of weak γT_0 and strong U/t_1 is interesting in the sense that as t_3/t_1 is varied, regimes with CW or CCW circulation are interspersed with the UD flow for $M = 3, 4, 5$. The $t_3/t_1 < 1$ parameter regime of the phase diagrams shown in the bottom row of Fig. 5.4 have CW circulations emerging at small values of t_3/t_1, but the UD regime occurs both above and below the CW regime. The competition among the different circulations in the small γT_0 and strong interaction regime implies the system is sensitive to the parameters, making the accurate measurement of phase diagrams of strongly interacting non-equilibrium systems challenging.

5.2.3 Photon number dependence of local transport

In this section we show how the local currents and densities of the photons are influenced by M. Fig. 5.5 shows the local steady-state photonic currents J_{12}, J_{23}, and J_{13} as functions of $1/M$ with $\gamma T_0 = 0.5$ and $U = 0$ for (top) $t_3/t_1 = 0.6$, (middle) $t_3/t_1 = 1.0$, (bottom) $t_3/t_1 = 1.4$. The insets of Fig. 5.5 show the occupation numbers on the three sites, n_1, n_2, n_3, as functions of $1/M$ with the same set of parameters of

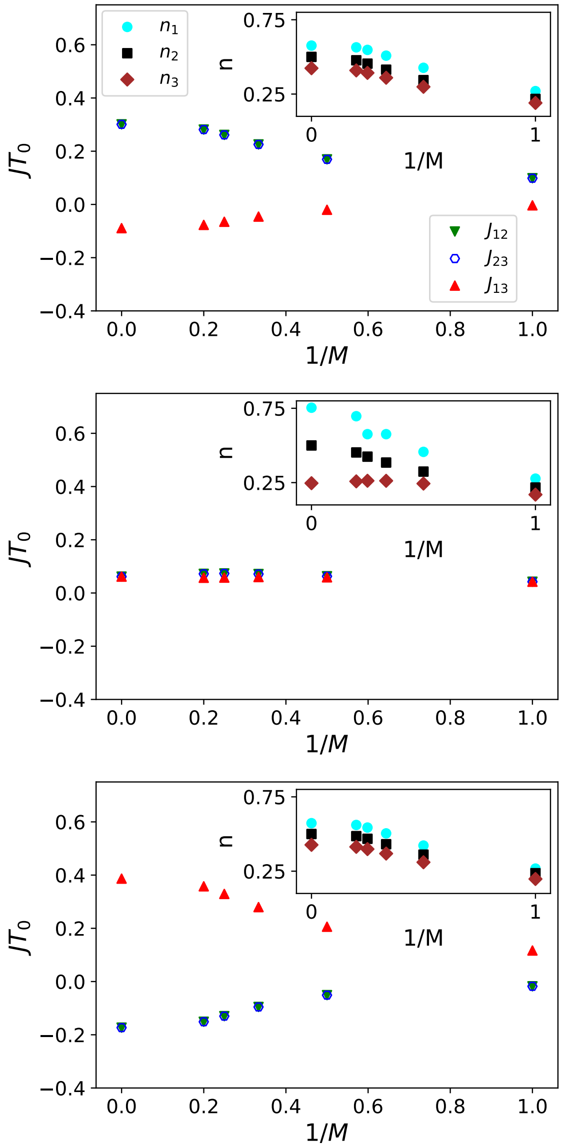

Figure 5.5: The dependence of the local steady-state currents J_{12} (blue hollow hexagons), J_{23} (green triangles), and J_{13} (red upside-down triangles) on $1/M$ for $t_3/t_1 = 0.6, 1.0, 1.4$ from top to bottom. Here $\gamma T_0 = 0.5$ and $U = 0$. J_{12} and J_{23} overlap in the steady-state. The insets show the photon occupation numbers on the three sites, n_1, n_2, and n_3 (cyan circles, black squares, and brown diamonds), as functions of $1/M$ with the same parameters as those in the main panels.

the main panels. While the local occupation numbers of the photons always follow

$n_3 < n_2 < n_1$ as shown in the insets of Fig. 5.5, the local currents exhibit different patterns depending on t_3/t_1. The $1/M = 0$ point shown in Fig. 5.5 were obtained using the third-quantization approach which we will talk about in sec. 5.2.4. With these results we show proof that the directions of the local currents are decoupled from the local densities in quantum transport of photons. In other words, it is possible to transport photons from a low-density site to a high-density one in the steady-state by using a multi-path geometry.

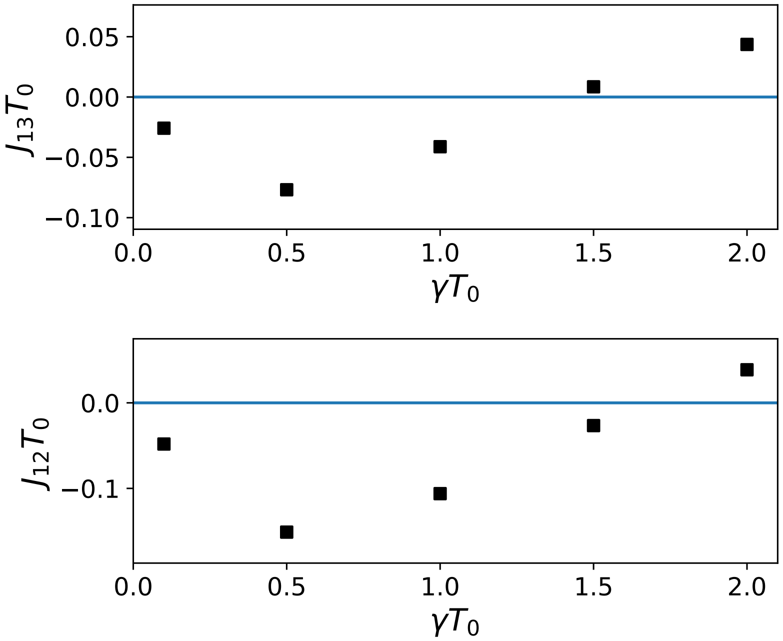

Figure 5.6: Tuning the local currents by the system-reservoir coupling γ: The upper (lower) panel shows J_{13} for $t_3/t_1 = 0.6$ and $M = 5$ (J_{12} for $t_3/t_1 = 1.4$ and $M = 5$). Both cases show a change of the sign of the local current as γ increases.

To further demonstrate the tunability of the local photonic currents, we show that for a given t_3/t_1 the local currents can change signs as γT_0 is varied. Fig. 5.6 shows J_{13} for $t_3/t_1 = 0.6$ and J_{12} for $t_3/t_1 = 1.4$ for the noninteracting case with $M = 5$ as functions of γT_0. A change in the sign of the local current implies the reversal of the direction of local flow. The possibility of tuning the local currents using the system-reservoir coupling γT_0 introduces additional knobs for controlling the photonic transport. Moreover, the dependence of the local photonic currents on

γT_0 implies that the photonic circulation results from a combination of the system and reservoirs, and hence as was the case in classical transport the atypical flow resulting in circulation is not an intrinsic property of just the TQDM.

We have verified that the results of the cases with asymmetric system-reservoir couplings ($\gamma_L \neq \gamma_R$) are qualitatively similar to those of the case with the symmetric condition as all flown patterns can be found in the asymmetric cases as well. We have also checked other values of N_L and N_R of the reservoirs, and the results seem to differ quantitatively. With all these results and checks, we conclude that the internal circulation of local photonic currents are robust against the asymmetry of the system-reservoir couplings and the number of particles in the reservoirs. This robustness of the geometry-induced circulation may increase the possibility of observing this phenomenon experimentally.

5.2.4 Photon circulation without photon blockade

In this section, we explicitly show that photon blockade is not necessary, at least in the noninteracting case, for internal circulation of local currents in the TQDM. We use the third-quantization formalism [64] for bosons outlined in sec. 2.2.2 and follow the protocol outlined in appendix A.4 to find the steady-state local currents when the basis for the TQDM photons is not truncated i.e. when $M \to \infty$.

Fig. 5.7 shows the phase diagram of the steady-state circulations of the noninteracting photons in the TQDM without any restriction on the number of photons on each site. All three types of flow patterns (CW, CCW, UD) are indeed present. Importantly, the noninteracting photons with $M \to \infty$ are the genuine case of a noninteracting system because imposing a restriction on the number of photons on each site may be considered as introducing effective interactions into the TQDM photons. Therefore, Fig. 5.7 establishes two crucial factors for internal circulation of local steady state photonic currents in the TQDM, the first is that the photon blockade is not a necessary condition and the second is that the geometry-induced circulation survives in the genuine noninteracting case.

A comparison of Fig. 5.7 for $M \to \infty$ with Fig. 5.3 for $M = 1, \cdots, 5$, reveals that

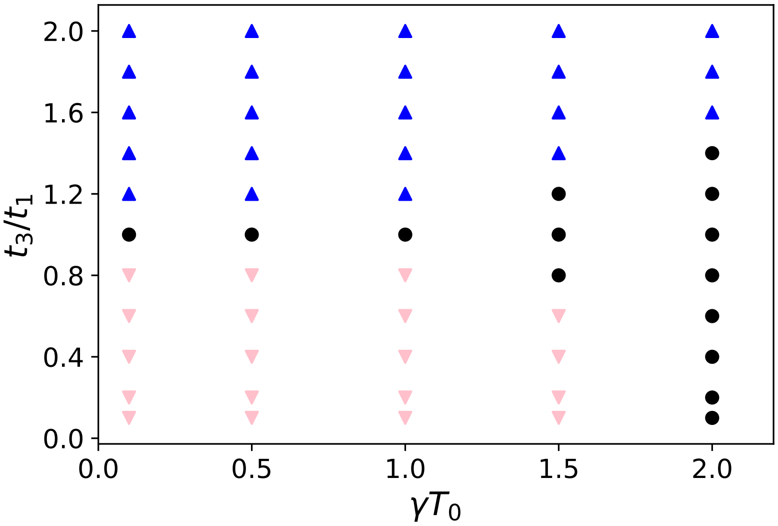

Figure 5.7: Phase diagram showing different steady-state patterns of the photonic current in a noninteracting ($U = 0$) system in absence of the photon blockade ($M \to \infty$). The pink upside-down triangles denote the CW circulation, the black circles denote the UD flow, and the blue triangles denote the CCW circulation.

the phase diagram of the untruncated TQDM photons is almost identical to the one with $M = 5$. Therefore, we surmise that circulation regimes saturate with increasing M in absence of the onsite interaction, and it is sufficient to analyze the systems with $M \leq 5$ for all practical purposes as we expect that the local currents and circulation patterns will remain basically the same as M increases above 5. The $1/M = 0$ point shown in Fig. 5.5 were also obtained using the third-quantization approach. We note that as $1/M$ decreases, the local currents and occupation numbers all approach the $1/M = 0$ values. This result also corroborates that the photonic transport in the TQDM saturates as M increases. It may be possible to approximate the qualitative behavior of the $M \to \infty$ limit through in systems with a moderate number of allowed photons.

The third-quantization method, however, is limited to noninteracting systems with linear system reservoir couplings. To study interaction effects in intermediate-sized systems one may use numerical methods such as the density-matrix renormalization group [63,92,104]. In this study, we have shown that the photon circulation survives in the TQDM with effective interactions, upto a maximum of $M \leq 5$ photons allowed per site.

5.3 Summary

In this chapter, we have shown that a multi-path geometry can lead to steady-state circulation of local photonic currents without introducing any artificial gauge field. The minimal system for emergence of these circulation patterns may be realized in a triangular geometry metastructure which is made up of photonic structures embedded with electronic quantum dots. The photon-exciton interactions may induce a photon blockade that restricts the number of photons per quantum dot. We show that the circulation patterns are observable for the both the noninteracting and interacting TQDM with photon blockade. Additionally, the photonic circulations have a non-trivial dependence not only on the internal system parameters such as the tunneling coefficients, or the onsite effective interaction but also on external parameters such as the system-reservoir coupling. Moreover we demonstrate decoupling of the direction of the local current from the density difference between the sites in the TQDM. We also show from our third quantization calculation that the circulations are robust, in the sense that photon blockade is not a necessary condition for the circulations to arise.

Chapter 6

Applications and experimental realization

In this chapter we begin with a discussion on how the systems of chapters 3, 4 and 5 may be realized experimentally. We follow up with possible applications of the geometry-based local atypical classical thermal current and quantum circulations.

6.1 Experimental realizations

Before we consider potential experimental setups which may be used to verify the classical local atypical current and quantum circulations we will briefly discuss the techniques for tuning system parameters. This discussion is pivotal as the applications introduced in the latter section require tuning of parameters of the multi-path systems.

Tuning mechanisms can be classified into two categories: mechanical or electromagnetic. In mechanical tuning, one may use atomic force microscopy [105, 106] to locally strain the material. The strain may modify the coupling between the system and the reservoirs. Density-functional theory calculations in Ref. [107] show that the thermal current in a molecular junction can be manipulated through mechanical compression for a wide range of temperatures, essentially due to mode localization. Ref. [108] shows, also using density functional theory, a significant suppression in the phononic thermal conductance of a molecular junction due to its structure.

Under electromagnetic techniques one can use lasers [109] to manipulate the interactions between the system and reservoirs on both the micro and mesoscopic scale. Alternatively, for substrates that are conducting or piezoelectric [110], can be subjected to an electric current or field to modify its coupling with the system. The modification will also affect the connections between the system and reservoirs, such that the system-reservoir coupling can be tuned indirectly. The biasing of quantum dots can also lead to change in certain system parameters of the metastructure proposed in chapter 5.

6.1.1 Classical multi-path system with Langevin reservoirs

The Langevin equation (3.3) does not differentiate the size of the system. For example, in Ref. [111] the authors experimentally study the motion of a macroscopic glass prism under the influence of Coulombic and kinematic friction while subjected to external white or Cauchy noise. They show that their experimental findings agree with drift velocities and diffusivities calculated through Langevin equation. In their experiment, the energy is delivered to the slider in terms of work and not thermal energy and additionally the friction and noise are introduced to the system through separate individual processes. However, as Langevin equations describe systems where the friction and noise are simultaneous effects introduced by just the presence of a reservoir i.e. these two effects are two different faces of the same action, it may be more feasible to realize local atypical currents in molecular or nano-mechanical systems [112–114]. For example, Ref. [113] describes the vibrational motion of a nanoelectromechanical system through classical Langevin equation where the coupling to the electrons results in the frictional and random force being exerted on the vibrational mode of the system.

There are studies and techniques for tuning the coupling between a molecular or nano-mechanical system and its environment [105–107, 109, 115–119]. One can envision realization of the setup shown in Figs. 3.1 and 3.7 in experiments performed at liquid nitrogen temperatures with nano-mechanical devices in which tuning the system-reservoir coupling by mechanical pressing or electromagnetic field as mentioned above can reverse the local thermal current, with which one may design a local thermal switch embedded in a multi-path geometry.

6.1.2 Geometry-based transport in quantum systems

In general, the ‘quantum-ness’ of a system can be determined through the fugacity z of the system [120]. The fugacity of the system can be defined as the ratio of the thermal de Broglie wavelength to the length per particle in a 1D system [120]. Hence any treatment of a system, whether classical ($z << 1$) or quantum ($z > 1$) mechanical, must be done after careful consideration of the fugacity of the system. For example, a molecular system with mass $\approx 10^{-24} kg$ confined to a nanometer sized geometry has ($z \approx 10^{-2} < 1$) at liquid Nitrogen temperatures and a ($z > 1$) at μK temperatures. Hence the same system is capable of showing both quantum and classical behavior depending on the operating temperature of the reservoirs.

For quantum systems, a laser may function as a reservoir that supplies energy or particles to a localized part of the system. For example, in Ref. [121] the authors use a pulsed laser to excite a chain of trapped ions and study its energy transport. In accordance with the theoretical parameters, the geometry-based circulations may survive in experiments performed at Liquid Helium temperature with the frequencies of the system of interest in the terahertz range.

The systems shown in Figs. 4.1, 5.1 may be realizable in quantum dots [122], quantum dot - cavity systems, [123], molecular systems [124, 125] or trapped ion systems [121]. In addition, these systems may also be realizable through cold-atom simulators. Recently there has been progress towards engineering nearest neighbor and next-nearest neighbor hopping coefficients of bosonic atoms in optical potentials connected to particle reservoirs [126], which may resemble the setup of Fig. 5.1. The bosonic cold-atoms are massive bosons, but the photons are massless bosons. However, as the geometry-based circulation only concerns the wave nature, circulations should emerge in both systems with massive and massless bosons.

The TQDM we envision in Fig. 5.1 comprises of a photonic crystal which houses

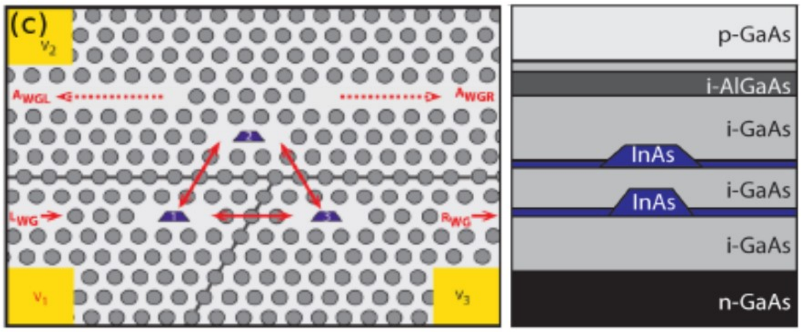

Figure 6.1: Illustration of an experimental realization of the TQDM and the schematics of the layer structure of the pin-diode structure. In the TQDM, the dots are embedded in three L3 cavities in a photonic crystal membrane, formed by a pin-type diode. Photons are injected from the left waveguide, L_{WG} and extracted from the right waveguide, R_{WG}. Additional wave guides (A_{WGL}, A_{WGR}) may be used to measure the directionality of the photon flux. Reproduced with permission from "Tunable current circulation in triangular quantum-dot metastructures" EPL 123 (2018) 47002. Copyright (2018) Europhysics Letters

.

the photonic cavities embedded with the electronic quantum dots. The photonic crystal structures are commonly fabricated with electron-beam lithography and chemical etching. Protocol for fabricating nanophotonic crystal cavities and photonic crystal waveguides containing quantum dots have been established, for example in Refs. [127, 128].

For the experimental realization of the TQDM shown in Fig. 5.1 one needs to consider a system where the length scales of all the components of the TQDM such as the size of the photonic crystal and cavities, and the separation length of the cavities are of the order of the wavelength of the photons. The TQDM should be designed such that it allows individual tuning of each photonic crystal cavity through additional waveguides between the TQDM and the reservoirs such that it is possible to couple only two sites to the reservoirs [25]. Fig. 6.1 adapted from Ref. [25] outlines a realization of this TQDM and the corresponding pin-diode structures which houses the electronic quantum dots. In their visualization of the TQDM, they embed the quantum dots in three L3 cavities of a photonic crystal membrane through the fabrication of a pin-type diode illustrated in Fig. 6.1 adapted from Ref. [25]. Etching through the top layer of this pin-diode structure along the photonic crystal holes allows for separate tuning of the quantum dot excitonic transitions through gate voltages. In their setup, the photons are injected and extracted through waveguides and they suggest using additional waveguides to measure the directionality of the photon flux.

The cavity photon and quantum dot exciton composite system has two branches, an upper and a lower exciton-polariton branch. One can tune the reservoir to a frequency slightly above the lower branch to incoherently pump the photons into the TQDM, similar to the idea of Ref. [94]. The waveguides, through which the photons travel [25], should also be tuned to the frequency of the lower branch. To achieve sufficient polaritonic coupling between the cavity photons and quantum-dot excitons, the wavelength of the quantum dot should match with that of the photonic cavities. The separation between the cavities and the distance between the cavities and the waveguides determines the upper limit for the coupling strength, which in turn constrains the tunneling coefficients in the effective model.

The photon blockade in the TQDM may be realized using the quantum dot excitons. As suggested in Ref. [25], the number of excitons in each quantum dot can be tuned by the gate voltage. The excitonic transitions can be tuned in-situ, most conveniently by electric fields via the quantum confined Stark effect if the sample structure is designed as a (pin-type) diode as shown in Fig. 6.1. Since we only consider the transport of photons that couple to the excitons, the number of photons on each site may also be tuned by the gate voltage. However, each quantum dot may not accommodate more than a few excitons, so tuning the gate voltage may be more suitable for $M \leq 2$. To study transport in a photon blockade regime with $M > 2$, it is possible to adopt and modify the quantum-dot metastructure of Ref. [129]. The idea is to let each vertex of the triangle shown in Fig. 5.1 consist of multiple quantum dots, and each dot can hold up to one exciton. Therefore, each group of M quantum dots represents an effective site that can accommodate up to M photons, which can then be transported via the photonic structures.

For nanomechanical or molecular systems, the thermal currents may be measured through thermoreflectance [130] or scanning-probe techniques [125, 131–133]. To determine the circulation in the TQDM, additional photon detectors may be used which couple to the sites and siphon out some photons to measure their momentum, which determines the direction of the photonic current.

6.2 Applications

The direction of the classical local thermal current can be controlled by tuning internal and external system parameters such as ratio of springs and masses, and system-reservoir coupling. With this control over the direction of the local thermal current through system parameters, one can design a local thermal switch embedded in a multi-path geometry. For example, by tuning the system-reservoir coupling one can control the direction of the local thermal current. In another application, one may identify the two types of the local thermal current namely normal and atypical, with binary digits 0 and 1 and design classical memory elements.

As evident from the phase maps shown in chapter 4 and 5, the quantum circulations of internal currents can be manipulated by tuning internal system parameters such as the tunneling coefficients, interaction strength or external parameters such as the system-reservoir coupling, temperature, average number of particles in reservoir, the photon blockade parameter. Similar to building classical memory elements, geometry based CW and CCW internal circulation of thermal and particle transport may be used to encode the binary numbers 0 and 1 for realizing heat or particle based memory elements. Our ability to control electrons has driven major technological revolutions in the past; perhaps devices based on the above theoretical predictions which manipulate photons and phonons may result in exciting analogous advances and help utilize the higher frequency range of phonons and photons.

Another application of the TQMD proposed in chapter 5 allows the possibility of transporting photons from a low-density site to a high-density one using the multi-path geometry. The system shown in Fig. 5.1 may be viewed as a proof-of-principle device which may function as a controllable local photonic router. If one needs to transport photons from, say, site 2 to site 1 regardless of the densities on those sites, one can tune the internal or external parameters to ensure the system stays in the CCW circulation regime. This router is made possible by the underlying multi-path geometry which does not require interactions or artificial gauge fields.

There have been analogous studies of the local transport phenomena in the literature. Refs. [16,134] utilize the similarity between the Helmholtz equation for classical electromagnetic waves and the Schrödinger equation for the wavefunction of noninteracting quantum systems. Transport in a noninteracting many-body system can be solved by tackling the single-particle Hamiltonian as the many-body Hamiltonian of noninteracting particles is a direct sum of the single-particle Hamiltonians. In the analogous study, the role of the local current between two atoms in the single-particle picture is played by the transmission coefficient of microwaves between adjacent macroscopic resonators in the experiments. Ref. [16] experimentally verifies that the transmission coefficients of the microwave correspond to a circulating current in a benzene-like ring, showing the wave nature and the ability of multi-path geometry to induce an internal circulation. Quantum systems with interactions exhibit rich physics and in the presence of interactions, it is no longer possible to write the system Hamiltonian as a direct sum of single-particle Hamiltonians. Hence to study of quantum systems with interactions one needs to treat the system as a many-body problem which cannot be explained through the single-particle picture. While the microwave simulators have demonstrated circulating current for single-particle transport of the analogous quantum systems, the systems presented in Figs. 4.1 and 5.1 with non-zero U, may offer a route to the simulate many-body transport in quantum systems.

Chapter 7

Conclusion

There have been scattered studies of interesting phenomena in local thermal transport in specific multi-path networks [6, 7, 21, 135] which talk about either classical or quantum thermal transport but these documentations lack a comprehensive analysis of geometry-based local transport phenomena. With this thesis, we provide a systematic and comprehensive survey of geometry based steady-state transport in minimal multi-path systems and convey its ability to show a local atypical current universally across domains and different drives not just limited to thermal. A steady-state atypical local current is identified as the current that flows opposite to the direction of the total current which is determined by the external gradient.

Through this thesis, we show that a local steady-state atypical current is universal to multi-path system geometry and can arise across classical and quantum realms, using different formalisms and external drives. The physics behind the local atypical flow remains the same across these different scenarios. The transport of heat in the classical system is through normal modes while in the quantum system is through quantum particle waves. The multi-path geometry provides the flux different pathways to reach the other reservoir. Combined with the wave nature of transport and depending on the system parameters, this multi-path geometry allows certain paths to overflow; this overflow is compensated by an atypical flow on the other path. We also show that this atypical current is tunable and robust.

We consider a classical system made up of few masses and harmonic springs (Fig.

3.1), a system of three quantum oscillators coupled in a triangular multi-path geometry described in the coordinate-momentum space and through a Bose-Hubbard model (Fig. 4.1) and photons in a TQMD (Fig. 5.1). These systems are the minimal structures with either three oscillators or three quantum dots. In the next few paragraphs, we will summarise our results for these systems and show the universal and robust nature of steady-state local atypical currents.

First we looked at a classical multi-path harmonic system of three masses subject to Langevin reservoirs shown in Fig. 3.1. We show that the system exhibits a steady-state local atypical thermal current (hot-to-cold). Once we establish the emergence of atypical current we map out phase diagrams to demonstrate that the local atypical current is a function of both internal and external system parameters such as the ratio of spring constants, ratio of masses and system-reservoir coupling. We also show that the atypical current is robust against non-linearity introduced through substrate coupling, asymmetry of system-reservoir coupling and addition of masses.

Next, we show through the third quantization method for Redfield and Lindblad quantum master equations that local steady-state atypical thermal flows arise in a non-interacting quantum system of oscillators coupled in a triangular multi-path geometry. We show that in the appropriate high temperature limit, the Redfield results reproduce the classical results for thermal conductance. The local atypical flow gives rise to two circulation patterns in the system, namely clockwise and counterclockwise. We map out phase diagrams for the three flow patterns observed, the two circulations and unidirectional flow as a function of an internal parameter and the system-reservoir coupling. We also show numerical simulations of the Lindblad quantum master equation for the interacting Bose-Hubbard model and unequivocally show that the circulations are robust against onsite interactions.

Finally, we look at photons coupled to quantum dot excitons modelled phenomenologically through a Bose-Hubbard Hamiltonian. We run the simulations of the Lindblad quantum master equation in the photon blockade regime where the number of photons that participate in transport can be limited by the quantum-dot excitons. When subjected to photonic reservoirs, the system exhibits local atypical photonic current which gives rise to three flow patterns similar to what we saw in the case of thermal transport. We demonstrate again through phase maps that these steady-state internal circulations are present even as the number of allowed photons per site is increased from 1 to 5 and for both weak and strong onsite interactions. We show through third quantization calculations that the circulations exist in the regime without photon blockade. Lastly, we also show a decoupling between the direction of the local current and the occupation number at the sites.

With these results, we establish that geometry-based internal steady-state circulation of thermal and particle current is a robust and universal phenomenon found in quantum bosonic systems with multi-path geometries. Due to the same physics of waves in multi-path geometry, these circulations are not just limited to bosonic systems but can be found in fermionic systems as well [25]. Ref. [25] analyzes the electronic transport in a triple quantum dot metastructure, and it shows the same qualitative behavior (three flow patterns) as shown by the photons in a quantum dot metastructure and by the thermal currents in a multi-path geometry of a triangle. The transport analysis through the quantum master equation depends on the whether the carrier is bosonic or fermionic as the calculation of the commutator and the terms which model the interaction with the reservoirs implicitly depend on the spin-statistics of the carrier. This spin-statistics dependence causes quantitative differences in the circulation phase maps while the qualitative nature is intact.

We present phase maps for the quantum bosonic systems with multi-path geometry, which show how these circulations can be controlled for application purposes via tuning internal and external parameters. We clearly demonstrate that the steady-state circulations in systems with multi-path geometry do not require interactions or additional media. This may be useful for inducing circulations of neutral carriers such as photons and phonons, whose circulation generally requires interactions or coupling to matter.

The local atypical thermal currents may find application as temperature controlled classical memory elements or as a thermal switch. While in addition to these applications, the decoupling of atypical behavior and occupation number in the TQDM may be utilized to built a photonic router. The prospect of applications of the universal and non-trivial properties of multi-path system geometry combined with recent experimental progress in the fabrication and control of atomic, nano and mesoscopic systems lead us to believe that the atypical local currents may be realizable in a broad range of systems ranging from nano or molecular systems, quantum dot-photonic hybrid structures, to trapped atoms or ion systems. As our ability to control electrons has driven major technological revolutions in the past; we expect devices based on the above theoretical predictions which manipulate photons and phonons may result in exciting analogous advances.

Appendix A

Appendix

A.1 Basis construction

In this appendix, we provide an example of the basis states used for the numerical simulation of the LQME in a truncated space used in chapters 4 and 5. Theoretically, the basis for a single site bosonic system can be large as it can accommodate an infinite number of bosons. Now, the size of the Fock space for a system of N bosons in K sites is [136]:

$$\frac{(N+K-1)!}{N!(K-1)!} = \binom{N+K-1}{K-1}. \tag{A.1}$$

Numerical simulations are usually performed by limiting the maximum number of bosons per site, which we denote by M. This limitation leads to a 'truncation' of the system basis. For a single site system, it means:

$$|Site1\rangle = \{|0\rangle, |1\rangle, |2\rangle ..... |M\rangle\}. \tag{A.2}$$

The size of the Fock space for a system of K sites with N bosons such that at most M allowed per site ($M < N$) can be calculated [137]:

$$\sum_{j=0}^{[\frac{N}{M+1}]} (-1)^j \binom{N+K-1-j(M+1)}{K-1} \binom{K}{j}. \tag{A.3}$$

Here and in the algorithm, [] denote the floor function. It is clear to see how M reduces the size of the Fock space for the system. For example, given K=3 and N=4, the size of the untruncated Fock space is 15 while introducing $M = 3$ results in a size of 6. For sake of completeness, we explicitly write the algorithm of Ref. [62] with corrected typographical errors present in the original text. Here, the occupation vector is defined as $n_I = (n_1, n_2, ..., n_K)$, for us as $K = 3$, we have $n_I = (n_1, n_2, n_3)$.

Algorithm 1 Construction of ordered truncated basis

```
Inputs:
    $I = 1, K, N, M$
Initialize:
    $n_1 = ... = n_{[N/M]} = M,$
    $n_{[N/M]+1} = N - M * [N/M],$
    $n_{[N/M]+2} = .... = n_K = 0$
    $n_I = (n_1, n_2, ..., 0)$
1 $I = I + 1$
if $n_1 > 0$ then
    $\delta = 0$
    if $n_1 < M$ then
        $\delta = M - n_1$
        $n_1 = M$
    Let i be the smallest site index for which $n_i < M$ and $i > 1$
    $n_i = n_i + 1, n_{i-1} = n_{i-1} - 1 - \delta$
    $n_I = (n_1, n_2, ..., 0)$
    goto 1
if $n_1 > 0$ then
    Let j be the smallest site index for which $n_j > 0$ and $j > 1$
    Let i be the smallest site index for which $n_i < M$ and $i > j$
    If no such i exists goto 2
    $n_i = n_i + 1, n_{i-j} = n_j - 1$
    if $(i - j - 1) > 0$ then
        $n_{i-j-1} = n_{i-j-2} = ... = n_1 = M$
    $n_{i-j+1} = n_{i-j+2} = ... = n_{i-1} = 0$
    $n_I = (n_1, n_2, ...)$
    goto 1
2 end
```

We follow the above algorithm and build up the basis for each N ranging from 0 to N_{max}, where $N_{max} = KM$ is the maximum allowed bosons for the system given a specific K and M. Once the basis states are constructed, the next step is to assemble all the other elements such as the Hamiltonian, creation and annihilation matrices for each site which go into the LQME. To get the reduced density matrix of the system, the LQME is integrated through the fourth order Runge-Kutta method outlined in the next section.

A.2 Fourth order Runge-Kutta method

The fourth order Runge-Kutta method is used to numerically integrate differential equation:

$$\frac{d\rho}{dt} = \frac{\rho_{n+1} - \rho_n}{\Delta t} = f(\rho_n, t_n) \tag{A.4}$$

The Runge-Kutta algorithm breaks the interval, Δt into four smaller intervals through the mid-point method, such that more weight is assigned to the mid-points as follows:

$$\begin{aligned} \rho_{n+1} - \rho_n &= \frac{1}{6}(k_1 + 2(k_2 + k_3) + k_4) \\ k_1 &= \Delta t f(\rho_n, t_n) \\ k_2 &= \Delta t f(\rho_n + \frac{1}{2}\Delta t, t_n + \frac{1}{2}k_1) \\ k_3 &= \Delta t f(\rho_n + \frac{1}{2}\Delta t, t_n + \frac{1}{2}k_2) \\ k_4 &= \Delta t f(\rho_n + \Delta t, t_n + k_3) \end{aligned} \tag{A.5}$$

The application of the fourth-order Runge-Kutta to the LQME gives us the time evolution of the reduced density matrix. The expectation value of the system operators such as the local current and local occupation numbers can be calculated by taking the trace of the system operator with the reduced density matrix. Furthermore, the steady states values of the operator expectation value are extracted by taking the long time limit.

A.3 Third quantization formalism for the RQME

In this appendix, we show the step by step process to obtain the steady state correlations from the third quantization formalism for the RQME. First, we diagonalize the $\boldsymbol{Q}$ of Eq. (4.1):

$$\boldsymbol{Q} = \boldsymbol{U}\boldsymbol{\Omega}\boldsymbol{U}^{\dagger}. \tag{A.6}$$

Here, the columns of $\boldsymbol{U}$ are the right eigenvectors of $\boldsymbol{Q}$ and $\boldsymbol{\Omega}$ is a diagonal matrix whose entries are the corresponding eigenvalues of $\boldsymbol{Q}$. We also define $\lambda_j = \sqrt{\boldsymbol{\Omega}_{j,j}}$. For our system, with this $\boldsymbol{U}$, we can transform the momentum and coordinate vectors to the normal basis:

$$\underline{p'} = \underline{p}.\boldsymbol{U} \qquad \underline{q'} = \underline{q}.\boldsymbol{U} \tag{A.7}$$

Hereon, $'$ indicate vectors and operators in the normal basis. Now, according to Ref. [65], for our coupled quantum oscillator system we need to solve the following continuous Lyapunov equation:

$$\boldsymbol{X}^T\boldsymbol{Z} + \boldsymbol{Z}\boldsymbol{X} = \boldsymbol{Y} \tag{A.8}$$

Solving Eq. (A.8) yields the matrix $\boldsymbol{Z}$, whose elements are equivalent to the NESS correlation functions $\boldsymbol{Z}_{ij}^{a,b} = \langle a_i b_j \rangle$, with $a, b \in \{p, q\}$. The local currents and occupation numbers can then be calculated from these correlation functions. X^T and Y of Eq. (A.8) are defined as:

$$\boldsymbol{X}^T = \begin{pmatrix} \boldsymbol{M}_{\boldsymbol{im}}^{\boldsymbol{q'p'}} & \frac{\boldsymbol{\Omega}}{2} \\ -\frac{\mathbb{1}_{\boldsymbol{3}}}{2} & \boldsymbol{0} \end{pmatrix} \tag{A.9}$$

and

$$\boldsymbol{Y} = \frac{1}{2}\begin{pmatrix} \boldsymbol{M}_{\boldsymbol{r}}^{\boldsymbol{q'q'}} + (\boldsymbol{M}_{\boldsymbol{r}}^{\boldsymbol{q'q'}})^T & \boldsymbol{0} \\ \boldsymbol{0} & \boldsymbol{0} \end{pmatrix}. \tag{A.10}$$

Here, M are the bath matrices whose subscript im and r refer to imaginary and real part of those matrices. Following, Ref. [65], the bath matrices are:

$$\begin{aligned}\boldsymbol{M^{q'q'}} &= \frac{1}{2}X'_L \otimes X'_L diag((1+\exp(\frac{\lambda_j}{T_L}))\Gamma_L(\lambda_j)) \\ &\quad +\frac{1}{2}X'_R \otimes X'_R diag((1+\exp(\frac{\lambda_j}{T_R}))\Gamma_R(\lambda_j))\end{aligned} \tag{A.11}$$

$$\begin{aligned}\boldsymbol{M^{q'p'}} &= \frac{\iota}{2}X'_L \otimes X'_L diag((\frac{\exp(\lambda_j/T_L)-1}{\lambda_j})\Gamma_L(\lambda_j)) \\ &\quad +\frac{\iota}{2}X'_R \otimes X'_R diag((\frac{\exp(\lambda_j/T_R)-1}{\lambda_j})\Gamma_R(\lambda_j))\end{aligned} \tag{A.12}$$

A.4 Third quantization formalism for LQME

The Lindblad master equation considered in Ref. [64] is

$$\begin{aligned}\frac{\partial\rho(T)}{\partial T} &= \mathscr{L}\rho(t) \qquad (A.13) \\ &= i[\rho,\mathscr{H}] + \sum_\mu (2L_\mu\rho L_\mu^\dagger - \{L_\mu^\dagger L_\mu, \rho\}).\end{aligned}$$

Here L_μ denotes the Lindblad operators. The generalized decomposition of $\mathscr{H}$ and L_μ for the system shown in Fig. 3.1 are

$$\begin{aligned}\mathscr{H} &= \underline{c}^\dagger.\boldsymbol{H}\underline{c}, \\ L_\mu &= l_\mu.\underline{c} + k_\mu.\underline{c}^\dagger,\end{aligned} \tag{A.14}$$

where

$$\boldsymbol{H} = \begin{pmatrix} 0 & -t_1 & -t_3 \\ -t_1 & 0 & -t_1 \\ -t_3 & -t_1 & 0 \end{pmatrix} \tag{A.15}$$

encodes the information of the system parameters. $\underline{c}$ and $\underline{c}^\dagger$ are column vectors of the creation and annihilation operators. l_μ and k_μ are column vectors of the coefficients.

μ is the index over the reservoir terms. l_μ and k_μ for our system are given by

$$\begin{aligned} l_1 &= \begin{pmatrix} 0 & 0 & 0 \end{pmatrix}^T ; k_1 = \begin{pmatrix} \sqrt{\gamma N_L/2} & 0 & 0 \end{pmatrix}^T ; \\ l_2 &= \begin{pmatrix} \sqrt{\gamma (N_L+1)/2} & 0 & 0 \end{pmatrix}^T ; k_2 = \begin{pmatrix} 0 & 0 & 0 \end{pmatrix}^T ; \\ l_3 &= \begin{pmatrix} 0 & 0 & 0 \end{pmatrix}^T ; k_3 = \begin{pmatrix} 0 & 0 & \sqrt{\gamma N_R/2} \end{pmatrix}^T ; \\ l_4 &= \begin{pmatrix} 0 & 0 & \sqrt{\gamma (N_R+1)/2} \end{pmatrix}^T ; k_4 = \begin{pmatrix} 0 & 0 & 0 \end{pmatrix}^T . \end{aligned} \tag{A.16}$$

With those quantities, we can build the matrices $\boldsymbol{M}, \boldsymbol{N}$, and $\boldsymbol{L}$ mentioned in Ref. [64]. For our systems, they have the following expressions:

$$\boldsymbol{M} = \begin{pmatrix} \gamma(N_L+1)/2 & 0 & 0 \\ 0 & 0 & 0 \\ 0 & 0 & \gamma(N_R+1)/2 \end{pmatrix} . \tag{A.17}$$

$$\boldsymbol{N} = \begin{pmatrix} \gamma(N_L)/2 & 0 & 0 \\ 0 & 0 & 0 \\ 0 & 0 & \gamma(N_R)/2 \end{pmatrix} . \tag{A.18}$$

$$\boldsymbol{L} = \begin{pmatrix} 0 & 0 & 0 \\ 0 & 0 & 0 \\ 0 & 0 & 0 \end{pmatrix} . \tag{A.19}$$

Here we assume $\gamma_L = \gamma_R = \gamma$.

The Lindbladian $\mathscr{L}$ may be written in terms of $\underline{b}$, the transformation of $(a_0, a_1, a_0^{'}, a_1^{'})^T$, where $a_0, a_1, a_0^{'}, a_1^{'}$ represent combinations of the creation and annihilation operators $c, c^\dagger$ and satisfy the almost commutation relations of Ref. [64] shown explicitly in sec. (2.2.2). Here, X and Y are defined as:

$$X = \frac{1}{2} \begin{pmatrix} \iota \bar{\boldsymbol{H}} - \bar{\boldsymbol{N}} + \boldsymbol{M} & -2\iota \boldsymbol{K} - \boldsymbol{L} + \boldsymbol{L^T} \\ 2\iota \bar{\boldsymbol{K}} - \bar{\boldsymbol{L}} + \bar{\boldsymbol{L}}^{\boldsymbol{T}} & -\iota \boldsymbol{H} - \boldsymbol{N} + \bar{\boldsymbol{M}} \end{pmatrix} \tag{A.20}$$

and

$$Y = \frac{1}{2}\begin{pmatrix} -2\iota\bar{\boldsymbol{K}} - \bar{\boldsymbol{L}} - \bar{\boldsymbol{L}}^{\boldsymbol{T}} & 2\boldsymbol{N} \\ 2\boldsymbol{N}^{\boldsymbol{T}} & 2\iota\boldsymbol{K} - \boldsymbol{L} - \boldsymbol{L}^{\boldsymbol{T}} \end{pmatrix}. \tag{A.21}$$

According to Ref. [63], the continuous Lyapunov equation $X^T Z + ZX = Y$ in the absence of any coherent pumping term can be simplified as

$$\tilde{X}\tilde{Z} + \tilde{Z}\tilde{X}^{\dagger} = \tilde{Y}, \tag{A.22}$$

Where

$$X = \begin{pmatrix} \tilde{X} & 0 \\ 0 & \tilde{X}^* \end{pmatrix}, Y = \begin{pmatrix} 0 & \tilde{Y} \\ \tilde{Y} & 0 \end{pmatrix}. \tag{A.23}$$

For our system, using the previously defined $\boldsymbol{M}, \boldsymbol{N}$, and $\boldsymbol{L}$ matrices in conjunction with Eqs. (18) and (19) of Ref. [64], we can write $\tilde{X}$ and$\tilde{Y}$ as:

$$\tilde{X} = \frac{1}{2}\begin{pmatrix} \gamma/2 & -\iota t_1 & -\iota t_3 \\ -\iota t_1 & 0 & -\iota t_1 \\ -\iota t_3 & -\iota t_1 & \gamma/2 \end{pmatrix}. \tag{A.24}$$

and

$$\tilde{Y} = \begin{pmatrix} \gamma N_L/2 & 0 & 0 \\ 0 & 0 & 0 \\ 0 & 0 & \gamma N_R/2 \end{pmatrix}. \tag{A.25}$$

Solving Eq. (A.22) yields the matrix $\tilde{Z}$, whose elements are equivalent to the correlation functions $\tilde{Z}_{lj} = \langle c_j^{\dagger} c_l \rangle$. The local currents and occupation numbers can then be calculated from the correlation functions.

Bibliography

[1] Chaoliang Tan, Xiehong Cao, Xue-Jun Wu, Qiyuan He, Jian Yang, Xiao Zhang, Junze Chen, Wei Zhao, Shikui Han, Gwang-Hyeon Nam, et al. Recent advances in ultrathin two-dimensional nanomaterials. *Chem. Rev.*, 117(9):6225–6331, 2017.

[2] José A Barreto, William O'Malley, Manja Kubeil, Bim Graham, Holger Stephan, and Leone Spiccia. Nanomaterials: applications in cancer imaging and therapy. *Adv. Mater.*, 23(12):H18–H40, 2011.

[3] Hyungsuk Moon, Changmin Lee, Woosuk Lee, Jungwoo Kim, and Heeyeop Chae. Stability of quantum dots, quantum dot films, and quantum dot light-emitting diodes for display applications. *Adv. Mater.*, 31(34):1804294, 2019.

[4] Colin D Bruzewicz, John Chiaverini, Robert McConnell, and Jeremy M Sage. Trapped-ion quantum computing: Progress and challenges. *Appl. Phys. Rev.*, 6(2):021314, 2019.

[5] Mehran Kardar. *Statistical physics of particles.* Cambridge University Press, 2007.

[6] Sam Young Cho and Ross H McKenzie. Thermal and electrical currents in nanoscale electronic interferometers. *Phys. Rev. B*, 71(4):045317, 2005.

[7] J-P Eckmann and Emmanuel Zabey. Strange heat flux in (an) harmonic networks. *J. Stat. Phys.*, 114(1):515–523, 2004.

[8] Yakir Aharonov and David Bohm. Significance of electromagnetic potentials in the quantum theory. *Phys. Rev.*, 115(3):485, 1959.

[9] Santanu K Maiti. Quantum transport in mesoscopic ring structures: effects of impurities, long-range hopping and interactions. *Quantum Matter*, 3(5):413–434, 2014.

[10] MA Castellanos-Beltran, DQ Ngo, WE Shanks, AB Jayich, and JGE Harris. Measurement of the full distribution of persistent current in normal-metal rings. *Phys. Rev. Lett.*, 110(15):156801, 2013.

[11] AC Bleszynski-Jayich, WE Shanks, B Peaudecerf, E Ginossar, F Von Oppen, L Glazman, and JGE Harris. Persistent currents in normal metal rings. *Science*, 326(5950):272–275, 2009.

[12] David J Griffiths. Introduction to electrodynamics, 2005.

[13] S Reitzenstein, S Münch, P Franeck, A Löffler, S Höfling, L Worschech, A Forchel, I V Ponomarev, and T L Reinecke. Exciton spin state mediated photon-photon coupling in a strongly coupled quantum dot microcavity system. *Phys. Rev. B*, 82(12):121306(R), 2010.

[14] Daniel Hey and Enbang Li. Advances in synthetic gauge fields for light through dynamic modulation. *Roy. Soc. Open. Sci.*, 5(4):172447, 2018.

[15] John P Mathew, Javier Del Pino, and Ewold Verhagen. Synthetic gauge fields for phonon transport in a nano-optomechanical system. *Nat. Nanotechnol.*, 15(3):198–202, 2020.

[16] Thomas Stegmann, John A Franco-Villafañe, Yenni P Ortiz, Michael Deffner, Carmen Herrmann, Ulrich Kuhl, Fabrice Mortessagne, Francois Leyvraz, and Thomas H Seligman. Current vortices in aromatic carbon molecules. *Phys. Rev. B*, 102(7):075405, 2020.

[17] Thorsten Arnold, Chi-Shung Tang, Andrei Manolescu, and Vidar Gudmundsson. Magnetic-field-influenced nonequilibrium transport through a quantum

ring with correlated electrons in a photon cavity. *Phys. Rev. B*, 87(3):035314, 2013.

[18] José E Barquera-Lozada. Vorticity: Simplifying the analysis of the current density. *J. Comput. Chem.*, 40(30):2602–2610, 2019.

[19] Eudes Gomes and Fernando Moraes. Current vortices in hexagonal graphene quantum dots. *arXiv preprint arXiv:2103.09337*, 2021.

[20] Charles A Downing, David Zueco, and Luis Martín-Moreno. Chiral current circulation and PT symmetry in a trimer of oscillators. *ACS Photonics*, 7(12):3401–3414, 2020.

[21] Rahul Marathe, Abhishek Dhar, and AM Jayannavar. Energy current magnification in coupled oscillator loops. *Phys. Rev. E*, 82(3):031117, 2010.

[22] Tommaso Roscilde, Michael F Faulkner, Steven T Bramwell, and Peter CW Holdsworth. From quantum to thermal topological-sector fluctuations of strongly interacting bosons in a ring lattice. *New. J. Phys.*, 18(7):075003, 2016.

[23] EV Anda, G Chiappe, and E Louis. Circulating currents in a metallic ring with two quantum dots. *J. Appl. Phys.*, 111(3):033711, 2012.

[24] Marc-Olivier Renou, Elisa Bäumer, Sadra Boreiri, Nicolas Brunner, Nicolas Gisin, and Salman Beigi. Genuine quantum nonlocality in the triangle network. *Phys. Rev. Lett.*, 123(14):140401, 2019.

[25] Chen-Yen Lai, Massimiliano Di Ventra, Michael Scheibner, and Chih-Chun Chien. Tunable current circulation in triangular quantum-dot metastructures. *EPL*, 123(4):47002, 2018.

[26] Jian-Sheng Wang, Bijay Kumar Agarwalla, Huanan Li, and Juzar Thingna. Nonequilibrium Green's function method for quantum thermal transport. *Front. Phys.-Beijing*, 9(6):673–697, 2014.

[27] Zhi-Zhou Yu, Guo-Huan Xiong, and Li-Fa Zhang. A brief review of thermal transport in mesoscopic systems from nonequilibrium Green's function approach. *Front. Phys.-Beijing*, 16(4):1–18, 2021.

[28] Ken Funo and HT Quan. Path integral approach to quantum thermodynamics. *Phys. Rev. Lett.*, 121(4):040602, 2018.

[29] Michael Kilgour, Bijay Kumar Agarwalla, and Dvira Segal. Path-integral methodology and simulations of quantum thermal transport: Full counting statistics approach. *J. Chem. Phys.*, 150(8):084111, 2019.

[30] Stéphane Attal and Alain Joye. The Langevin equation for a quantum heat bath. *J. Funct. Anal.*, 247(2):253–288, 2007.

[31] Abhishek Dhar and Dibyendu Roy. Heat transport in harmonic lattices. *J. Stat. Phys.*, 125(4):801–820, 2006.

[32] Abhishek Dhar. Heat transport in low-dimensional systems. *Adv. Phys.*, 57(5):457–537, 2008.

[33] Jian-Sheng Wang. Quantum thermal transport from classical molecular dynamics. *Phys. Rev. Lett.*, 99(16):160601, 2007.

[34] Peter Zoller and Crispin W Gardiner. Quantum noise in quantum optics: the stochastic Schrödinger equation. *arXiv preprint quant-ph/9702030*, 1997.

[35] George W Ford, John T Lewis, and RF O'connell. Quantum Langevin equation. *Phys. Rev. A*, 37(11):4419, 1988.

[36] GW Ford, M Kac, and P Mazur. Statistical mechanics of assemblies of coupled oscillators. *J. Math. Phys.*, 6(4):504–515, 1965.

[37] NG Van Kampen and I Oppenheim. Langevin and master equation in quantum mechanics. *J. Stat. Phys.*, 87(5):1325–1334, 1997.

[38] Daniel Boyanovsky and David Jasnow. Heisenberg-Langevin versus quantum master equation. *Phys. Rev. A*, 96(6):062108, 2017.

[39] Archak Purkayastha, Abhishek Dhar, and Manas Kulkarni. Out-of-equilibrium open quantum systems: A comparison of approximate quantum master equation approaches with exact results. *Phys. Rev. A*, 93(6):062114, 2016.

[40] Stefano Lepri, Roberto Livi, and Antonio Politi. Thermal conduction in classical low-dimensional lattices. *Phys. Rep.*, 377(1):1–80, 2003.

[41] Ryogo Kubo. The fluctuation-dissipation theorem. *Rep. Prog. Phys.*, 29(1):255, 1966.

[42] Jordi García-Ojalvo and José Sancho. *Noise in spatially extended systems.* Springer Science & Business Media, 2012.

[43] Emilio Cortes, Bruce J West, and Katja Lindenberg. On the generalized Langevin equation: Classical and quantum mechanical$^{a)}$. *J. Chem. Phys.*, 82(6):2708–2717, 1985.

[44] J Łuczka. Non-markovian stochastic processes: Colored noise. *Chaos*, 15(2):026107, 2005.

[45] Desmond J Higham. An algorithmic introduction to numerical simulation of stochastic differential equations. *SIAM review*, 43(3):525–546, 2001.

[46] Eric Vanden-Eijnden and Giovanni Ciccotti. Second-order integrators for Langevin equations with holonomic constraints. *Chem. Phys. Lett.*, 429(1-3):310–316, 2006.

[47] Timothy Sauer. Computational solution of stochastic differential equations. *Wiley Interdiscip Rev: Comput Stat*, 5(5):362–371, 2013.

[48] Jun John Sakurai and Eugene D Commins. Modern quantum mechanics, revised edition, 1995.

[49] Heinz-Peter Breuer and Francesco Petruccione. *The theory of open quantum systems.* Oxford University Press, Oxford, UK, 2002.

[50] Daniel A Lidar. Lecture notes on the theory of open quantum systems. *arXiv preprint arXiv:1902.00967*, 2019.

[51] Serge Haroche and J-M Raimond. *Exploring the quantum: atoms, cavities, and photons*. Oxford University Press, 2006.

[52] Ahsan Nazir. Lecture notes on open quantum systems. *Accesible via https://www.yumpu.com/en/document/read/8219582/lecture-notes-on-open-quantum-systems-workspace*, 2012.

[53] Maximilian A Schlosshauer. *Decoherence: and the quantum-to-classical transition*. Springer Science & Business Media, 2007.

[54] Jan Jeske, David J Ing, Martin B Plenio, Susana F Huelga, and Jared H Cole. Bloch-Redfield equations for modeling light-harvesting complexes. *J. Chem. Phys.*, 142(6):064104, 2015.

[55] Shiwu Gao. Dissipative quantum dynamics with a Lindblad functional. *Phys. Rev. Lett.*, 79(17):3101, 1997.

[56] Göran Lindblad. Brownian motion of a quantum harmonic oscillator. *Rep. Math. Phys.*, 10(3):393–406, 1976.

[57] Paola Cappellaro. Chapter 8: Open quantum systems. In *Quantum Theory of Radiation Interactions—MIT Course No. 22.51*. MIT OpenCourseWare, License : Creative Commons BY-NC-SA., Cambridge MA, 2012.

[58] John Preskill. Lecture notes for ph219/cs219: Quantum information. *Accesible via http://www. theory. caltech. edu/people/preskill/ph229*, 2015.

[59] Hannu Wichterich, Markus J Henrich, Heinz-Peter Breuer, Jochen Gemmer, and Mathias Michel. Modeling heat transport through completely positive maps. *Phys. Rev. E*, 76(3):031115, 2007.

[60] Giulio Amato, Heinz-Peter Breuer, Sandro Wimberger, Alberto Rodríguez, and Andreas Buchleitner. Noninteracting many-particle quantum transport between finite reservoirs. *Phys. Rev. A*, 102(2):022207, 2020.

[61] Tomaž Prosen and Bojan Žunkovič. Exact solution of markovian master equations for quadratic fermi systems: thermal baths, open xy spin chains and non-equilibrium phase transition. *New. J. Phys.*, 12(2):025016, 2010.

[62] Ágnes Szabados, Péter Jeszenszki, and Péter R Surján. Efficient iterative diagonalization of the Bose-Hubbard model for ultracold bosons in a periodic optical trap. *Chem. Phys.*, 401:208–216, 2012.

[63] Iztok Pižorn. One-dimensional Bose-Hubbard model far from equilibrium. *Phys. Rev. A*, 88(4):043635, 2013.

[64] Tomaž Prosen and Thomas H Seligman. Quantization over boson operator spaces. *J. Phys. A: Math Theor.*, 43(39):392004, 2010.

[65] Bojan Žunkovič and Tomaž Prosen. Heat transport in quantum harmonic chains with Redfield baths. In *AIP Conf. Proc.*, volume 1468, pages 350–366. AIP, 2012.

[66] J Clerk Maxwell. Tait's "thermodynamics". *Nature*, 17(432):278, 1878.

[67] Dibyendu Roy and Abhishek Dhar. Role of pinning potentials in heat transport through disordered harmonic chains. *Phys. Rev. E*, 78(5):051112, 2008.

[68] Daxing Xiong, Danial Saadatmand, and Sergey V Dmitriev. Crossover from ballistic to normal heat transport in the ϕ^4 lattice: If nonconservation of momentum is the reason, what is the mechanism? *Phys. Rev. E*, 96(4):042109, 2017.

[69] A V Savin and O V Gendelman. Heat conduction in one-dimensional lattices with on-site potential. *Phys. Rev. E*, 67(4):041205, 2003.

[70] Stefano Lepri, Roberto Livi, and Antonio Politi. Heat transport in low dimensions: introduction and phenomenology. In *Thermal transport in low dimensions*, pages 1–37. Springer, 2016.

[71] Jie Chen, Gang Zhang, and Baowen Li. Molecular dynamics simulations of heat conduction in nanostructures: effect of heat bath. *J. Phys. Soc. Jpn.*, 79(7):074604, 2010.

[72] William T Coffey and Yuri P Kalmykov. *The Langevin equation: with applications to stochastic problems in physics, chemistry and electrical engineering.* World Scientific, 2004.

[73] Chih-Chun Chien, Kirill A Velizhanin, Yonatan Dubi, and Michael Zwolak. Tunable thermal switching via DNA-based nano-devices. *Nanotechnology*, 24(9):095704, 2013.

[74] Ian F Akyildiz and Josep Miquel Jornet. The internet of nano-things. *IEEE Wirel. Commun.*, 17(6), 2010.

[75] Chunyu Li and Tsu-Wei Chou. Vibrational behaviors of multiwalled-carbon-nanotube-based nanomechanical resonators. *Appl. Phys. Lett.*, 84(1):121–123, 2004.

[76] Shaoqing Du, Kenji Yoshida, Ya Zhang, Ikutaro Hamada, and Kazuhiko Hirakawa. Terahertz dynamics of electron–vibron coupling in single molecules with tunable electrostatic potential. *Nat. Photonics*, 12(10):608, 2018.

[77] A Casher and J L Lebowitz. Heat flow in regular and disordered harmonic chains. *J. Math. Phys.*, 12(8):1701–1711, 1971.

[78] Emmanuel Pereira, Leonardo M Santana, and Ricardo Ávila. Heat-flow properties of systems with alternate masses or alternate on-site potentials. *Phys. Rev. E*, 84(1):011116, 2011.

[79] Venkateshan Kannan, Abhishek Dhar, and JL Lebowitz. Nonequilibrium stationary state of a harmonic crystal with alternating masses. *Phys. Rev. E*, 85(4):041118, 2012.

[80] Chih-Chun Chien, Said Kouachi, Kirill A Velizhanin, Yonatan Dubi, and Michael Zwolak. Thermal transport in dimerized harmonic lattices: Exact solution, crossover behavior, and extended reservoirs. *Phys. Rev. E*, 95(1):012137, 2017.

[81] Kirill A Velizhanin, Subin Sahu, Chih-Chun Chien, Yonatan Dubi, and Michael Zwolak. Crossover behavior of the thermal conductance and Kramers' transition rate theory. *Sci. Rep.*, 5:17506, 2015.

[82] David J Griffiths. *Introduction to Electrodynamics*. Prentice Hall, New Jersey, USA, 3 edition, 1999.

[83] A Asadian, D Manzano, M Tiersch, and H J Briegel. Heat transport through lattices of quantum harmonic oscillators in arbitrary dimensions. *Phys. Rev. E*, 87(1):012109, 2013.

[84] F Nicacio, A Ferraro, A Imparato, M Paternostro, and F L Semião. Thermal transport in out-of-equilibrium quantum harmonic chains. *Phys. Rev. E*, 91(4):042116, 2015.

[85] Marco Cattaneo, Gian Luca Giorgi, Sabrina Maniscalco, and Roberta Zambrini. Local versus global master equation with common and separate baths: superiority of the global approach in partial secular approximation. *New. J. Phys.*, 21(11):113045, 2019.

[86] Jürgen T Stockburger and Thomas Motz. Thermodynamic deficiencies of some simple Lindblad operators: A diagnosis and a suggestion for a cure. *Fortschr. Phys.*, 65(6-8):1600067, 2017.

[87] Amikam Levy and Ronnie Kosloff. The local approach to quantum transport may violate the second law of thermodynamics. *Europhys. Lett.)*, 107(2):20004, 2014.

[88] Gabriele De Chiara, Gabriel Landi, Adam Hewgill, Brendan Reid, Alessandro Ferraro, Augusto J Roncaglia, and Mauro Antezza. Reconciliation of quantum

local master equations with thermodynamics. *New. J. Phys.*, 20(11):113024, 2018.

[89] Adam Hewgill, Gabriele De Chiara, and Alberto Imparato. Quantum thermodynamically consistent local master equations. *Phys. Rev. Res.*, 3(1):013165, 2021.

[90] B Ahmadi, S Salimi, and AS Khorashad. Refined definitions of heat and work in quantum thermodynamics. *arXiv preprint arXiv:1912.01983*, 2019.

[91] Sahar Alipour, Fabio Benatti, Faraj Bakhshinezhad, Maryam Afsary, Stefano Marcantoni, and Ali T Rezakhani. Correlations in quantum thermodynamics: Heat, work, and entropy production. *Sci. Rep.*, 6(1):1–14, 2016.

[92] Chen-Yen Lai and Chih-Chun Chien. Challenges and constraints of dynamically emerged source and sink in atomtronic circuits: From closed-system to open-system approaches. *Sci. Rep.*, 6:37256, 2016.

[93] Hemant Sankar Dutta, Amit Kumar Goyal, Varun Srivastava, and Suchandan Pal. Coupling light in photonic crystal waveguides: A review. *Photonics Nanostruct: Fundam Appl*, 20:41–58, 2016.

[94] Lukas M Sieberer, Michael Buchhold, and Sebastian Diehl. Keldysh field theory for driven open quantum systems. *Rep. Prog. Phys.*, 79(9):096001, 2016.

[95] M Petruzzella, S Birindelli, F M Pagliano, D Pellegrino, Z Zobenica, E H Li, L H andLinfield, and A Fiore. Quantum photonic integrated circuits based on tunable dots and tunable cavities. *APL Photonics*, 3:106103, 2018.

[96] F Liu, A J Brash, J O'Hara, L M P P Martins, C L Phillips, R J Coles, B Royall, E Clarke, C Bentham, N Prtljaga, I E Itskevich, L R Wilson, M S Skolnick, and A M Fox. High Purcell factor generation of indistinguishable on-chip single photons. *Nat. Nanotech.*, 13:835, 2018.

[97] Angel Rivas and Susana F Huelga. *Open quantum systems*. Springer, Berlin, Germany, 2012.

[98] MS Sarandy and DA Lidar. Abelian and non-abelian geometric phases in adiabatic open quantum systems. *Phys. Rev. A*, 73(6):062101, 2006.

[99] William H Press, Saul A Teukolsky, William T Vetterling, and Brian P Flannery. *Numerical recipes 3rd edition: The art of scientific computing.* Cambridge University Press, Cambridge, UK, 2007.

[100] O Kyriienko, DN Krizhanovskii, and IA Shelykh. Nonlinear quantum optics with trion polaritons in 2d monolayers: Conventional and unconventional photon blockade. *Phys. Rev. Lett.*, 125(19):197402, 2020.

[101] Jacek Kasprzak, Murielle Richard, S Kundermann, A Baas, P Jeambrun, Jonathan Mark James Keeling, FM Marchetti, MH Szymańska, R André, JL Staehli, et al. Bose-Einstein condensation of exciton polaritons. *Nature*, 443(7110):409–414, 2006.

[102] Arnaud Verger, Cristiano Ciuti, and Iacopo Carusotto. Polariton quantum blockade in a photonic dot. *Phys. Rev. B*, 73(19):193306, 2006.

[103] Chandra Roychoudhuri, Al F Kracklauer, and Kathy Creath. *The nature of light: what is a photon?* CRC Press, Boca Raton, Florida, 2008.

[104] Giuliano Benenti, Giulio Casati, Tomaž Prosen, Davide Rossini, and Marko Žnidarič. Charge and spin transport in strongly correlated one-dimensional quantum systems driven far from equilibrium. *Phys. Rev. B*, 80(3):035110, 2009.

[105] Daniel Ratchford, Farbod Shafiei, Suenne Kim, Stephen K Gray, and Xiaoqin Li. Manipulating coupling between a single semiconductor quantum dot and single gold nanoparticle. *Nano. Lett.*, 11(3):1049–1054, 2011.

[106] Changgu Lee, Xiaoding Wei, Jeffrey W Kysar, and James Hone. Measurement of the elastic properties and intrinsic strength of monolayer graphene. *Science*, 321(5887):385–388, 2008.

[107] Qian Li, Ivan Duchemin, Shiyun Xiong, Gemma C Solomon, and Davide Donadio. Mechanical tuning of thermal transport in a molecular junction. *J. Phys. Chem. C*, 119(43):24636–24642, 2015.

[108] Qian Li, Mikkel Strange, Ivan Duchemin, Davide Donadio, and Gemma C Solomon. A strategy to suppress phonon transport in molecular junctions using π-stacked systems. *J. Phys. Chem. C*, 121(13):7175–7182, 2017.

[109] BS Yilbas and AFM Arif. Material response to thermal loading due to short pulse laser heating. *Int. J. Heat Mass Trans.*, 44(20):3787–3798, 2001.

[110] Fei Ding, Hengxing Ji, Yonghai Chen, Andreas Herklotz, Kathrin Dorr, Yongfeng Mei, Armando Rastelli, and Oliver G Schmidt. Stretchable graphene: a close look at fundamental parameters through biaxial straining. *Nano. Lett.*, 10(9):3453–3458, 2010.

[111] PS Goohpattader, S Mettu, and MK Chaudhury. Experimental investigation of the drift and diffusion of small objects on a surface subjected to a bias and an external white noise: roles of coulombic friction and hysteresis. *Langmuir*, 25(17):9969–9979, 2009.

[112] S Taylor Smith and Roberto Onofrio. Thermalization in open classical systems with finite heat baths. *Eur. Phys. J. B*, 61(3):271–275, 2008.

[113] Liliana Arrachea, Niels Bode, and Felix Von Oppen. Vibrational cooling and thermoelectric response of nanoelectromechanical systems. *Phys. Rev. B*, 90(12):125450, 2014.

[114] Avishai Benyamini, Assaf Hamo, S Viola Kusminskiy, Felix von Oppen, and Shahal Ilani. Real-space tailoring of the electron–phonon coupling in ultraclean nanotube mechanical resonators. *Nat. Phys.*, 10(2):151–156, 2014.

[115] Fakhreddine Landolsi, Fathi H Ghorbel, and James B Dabney. Adhesion and friction coupling in atomic force microscope-based nanopushing. *J. Dyn. Syst.-T. ASME.*, 135(1):011002, 2013.

[116] BA Nelson and WP King. Measuring material softening with nanoscale spatial resolution using heated silicon probes. *Rev. Sci. Instrum.*, 78(2):023702, 2007.

[117] Zhun-Yong Ong and Eric Pop. Effect of substrate modes on thermal transport in supported graphene. *Phys. Rev. B*, 84(7):075471, 2011.

[118] Zhiping Xu and Markus J Buehler. Nanoengineering heat transfer performance at carbon nanotube interfaces. *ACS Nano*, 3(9):2767–2775, 2009.

[119] Chen Si, Zhimei Sun, and Feng Liu. Strain engineering of graphene: a review. *Nanoscale*, 8(6):3207–3217, 2016.

[120] Josef Honerkamp. *Statistical physics: an advanced approach with applications.* Springer Science & Business Media, 2012.

[121] Michael Ramm, Thaned Pruttivarasin, and Hartmut Häffner. Energy transport in trapped ion chains. *New. J. Phys.*, 16(6):063062, 2014.

[122] A Noiri, K Kawasaki, T Otsuka, T Nakajima, J Yoneda, S Amaha, MR Delbecq, K Takeda, G Allison, A Ludwig, et al. A triangular triple quantum dot with tunable tunnel couplings. *Semicond. Sci. Technol.*, 32(8):084004, 2017.

[123] Ting Shan Luk, Shisheng Xiong, Weng W Chow, Xiaoyu Miao, Ganapathi Subramania, Paul J Resnick, Arthur J Fischer, and Jeffrey C Brinker. Anomalous enhanced emission from PbS quantum dots on a photonic-crystal microcavity. *J. Opt. Soc. Am. B*, 28(6):1365–1373, 2011.

[124] Troels Markussen. Phonon interference effects in molecular junctions. *J. Chem. Phys.*, 139(24):244101, 2013.

[125] Charalambos Evangeli, Katalin Gillemot, Edmund Leary, M Teresa Gonzalez, Gabino Rubio-Bollinger, Colin J Lambert, and Nicolas Agrait. Engineering the thermopower of C_{60} molecular junctions. *Nano. Lett.*, 13(5):2141–2145, 2013.

[126] W Gou, T Chen, D Xie, T Xiao, T S Deng, B Gadway, W Yi, and B Yan. Tunable non-reciprocal quantum transport through a dissipative aharonov-bohm ring in ultracold atoms, 2020. arXiv: 2001.01859.

[127] T Yoshie, A Scherer, J Hendrickson, G Khitrova, H M Gibbs, G Rupper, C Ell, O B Shchekin, and D G Deppe. Vacuum Rabi splitting with a single quantum dot in a photonic crystal nanocavity. *Nature*, 432:200, 2004.

[128] J P Reithmaier, G Sek, A Loffler, C Hofmann, S Kuhn, S Reitzenstein, L V Keldysh, V D Kulakovskii, T L Reinecke, and A Forche. Strong coupling in a single quantum dot–semiconductor microcavity system. *Nature*, 432:197, 2004.

[129] Joel Q Grim, Allan S Bracker, Maxim Zalalutdinov, Samuel G Carter, Alexander C Kozen, Mijin Kim, Chul Soo Kim, Jerome T Mlack, Michael Yakes, Bumsu Lee, et al. Scalable in operando strain tuning in nanophotonic waveguides enabling three-quantum-dot superradiance. *Nat. Mater.*, 18(9):963–969, 2019.

[130] Alexandros El Sachat, Francesc Alzina, Clivia M Sotomayor Torres, and Emigdio Chavez-Angel. Heat transport control and thermal characterization of low-dimensional materials: A review. *Nanomaterials*, 11(1):175, 2021.

[131] Longji Cui, Ruijiao Miao, Chang Jiang, Edgar Meyhofer, and Pramod Reddy. Perspective: Thermal and thermoelectric transport in molecular junctions. *J. Chem. Phys.*, 146(9):092201, 2017.

[132] Nico Mosso, Hatef Sadeghi, Andrea Gemma, Sara Sangtarash, Ute Drechsler, Colin Lambert, and Bernd Gotsmann. Thermal transport through single-molecule junctions. *Nano. Lett.*, 19(11):7614–7622, 2019.

[133] T Meier, F Menges, P Nirmalraj, H Hölscher, H Riel, and B Gotsmann. Length-dependent thermal transport along molecular chains. *Phys. Rev. Lett.*, 113(6):060801, 2014.

[134] Matthieu Bellec, Ulrich Kuhl, Gilles Montambaux, and Fabrice Mortessagne. Tight-binding couplings in microwave artificial graphene. *Phys. Rev. B*, 88(11):115437, 2013.

[135] Christian Maes, Karel Netočnỳ, and Michel Verschuere. Heat conduction networks. *J. Stat. Phys.*, 111(5):1219–1244, 2003.

[136] Bansal Garg et al. *Thermal physics.* Tata McGraw-Hill Education, 1993.

[137] Maciej Lewenstein, Anna Sanpera, Veronica Ahufinger, Bogdan Damski, Aditi Sen, and Ujjwal Sen. Ultracold atomic gases in optical lattices: mimicking condensed matter physics and beyond. *Adv. Phys.*, 56(2):243–379, 2007.